JINGLE – IV. Dust, H I gas and metal scaling laws in the local Universe

Article (Accepted Version)

MNRAS 000, 1–36 (2020) Preprint 4 June 2020 Compiled using MNRAS LATEX style file v3.0

JINGLE – IV. Dust, HI gas and metal scaling laws in the local Universe

I. De Looze[1,2,⋆†], I. Lamperti[2], A. Saintonge[2], M. Relaño[3,4], M. W. L. Smith[5], C. J. R. Clark[6], C. D. Wilson[7], M. Decleir[6], A. P. Jones[8], R. C. Kennicutt[9,10], G. Accurso[2], E. Brinks[11], M. Bureau[12,13], P. Cigan[5], D L. Clements[14], P. De Vis[5], L. Fanciullo[15], Y. Gao[16,17], W. K. Gear[18], L. C. Ho[19,20], H. S. Hwang[21], M. J. Michałowski[22], J. C. Lee[21], C. Li[23], L. Lin[15], T. Liu[24], M. Lomaeva[2], H.-A. Pan[15,25], M. Sargent[26], T. Williams[25], T. Xiao[15,27], M. Zhu[28]

Accepted 2020 April 9. Received 2020 March 6; in original form 2020 January 10.

ABSTRACT

Scaling laws of dust, HI gas and metal mass with stellar mass, specific star formation rate and metallicity are crucial to our understanding of the buildup of galaxies through their enrichment with metals and dust. In this work, we analyse how the dust and metal content varies with specific gas mass ($M_{\rm HI}/M_\star$) across a diverse sample of 423 nearby galaxies. The observed trends are interpreted with a set of Dust and Element evolUtion modelS (DEUS) – including stellar dust production, grain growth, and dust destruction – within a Bayesian framework to enable a rigorous search of the multi-dimensional parameter space. We find that these scaling laws for galaxies with $-1.0 \lesssim \log M_{\rm HI}/M_\star \lesssim 0$ can be reproduced using closed-box models with high fractions (37-89%) of supernova dust surviving a reverse shock, relatively low grain growth efficiencies (ϵ=30-40), and long dust lifetimes (1-2 Gyr). The models have present-day dust masses with similar contributions from stellar sources (50-80%) and grain growth (20-50%). Over the entire lifetime of these galaxies, the contribution from stardust (>90 %) outweighs the fraction of dust grown in the interstellar medium (<10 %). Our results provide an alternative for the chemical evolution models that require extremely low supernova dust production efficiencies and short grain growth timescales to reproduce local scaling laws, and could help solving the conundrum on whether or not grains can grow efficiently in the interstellar medium.

Key words: galaxies: evolution – galaxies: star formation – ISM: dust, extinction – ISM: abundances

1 SETTING THE SCENE

Dust grains make up only a small fraction (∼1% on average) of the interstellar mass in galaxies. Nonetheless, these dust particles play a crucial role in balancing local gas heating and cooling processes. Chemical reactions on the surfaces of dust grains result in the formation of a large variety of molecules, especially in regions of the interstellar medium (ISM) where gas phase chemistry is inefficient. The processing of about 30 to 50% of all stellar light in the Universe by dust grains (e.g., Driver et al. 2007; Bianchi et al. 2018) makes observations of the infrared (IR) dust emission furthermore essential for all studies of star formation to recover the bright ultraviolet (UV) and optical light emitted by young stellar populations.

Although the ubiquitous presence of interstellar gas (Hartmann 1904) and dust (Trumpler 1930) has been recognised for nearly a century, the origin and main formation channels for interstellar dust grains remain an open question. It is commonly accepted that dust grains can form through the condensation of metals in the cool envelopes of asymptotic giant branch (AGB) stars (e.g., Ferrarotti & Gail 2006; Nanni et al. 2013) and in the expanding ejecta of core-collapse supernovae (e.g., Barlow et al. 2010; Gomez et al. 2012; Matsuura et al. 2015; De Looze et al. 2017a; Temim

⋆ E-mail: ilse.delooze@ugent.be, idelooze@star.ucl.ac.uk
† Institutional affiliations are shown at the end of the paper.

et al. 2017; De Looze et al. 2019; Cigan et al. 2019), but these two stellar dust production sources appear not able to account for the bulk of the dust mass observed in galaxies at high redshift (Michałowski et al. 2010; Valiante et al. 2011; Rowlands et al. 2014; Michałowski 2015; Mancini et al. 2015; Graziani et al. 2019) and in the nearby Universe (Matsuura et al. 2013; De Looze et al. 2016; Schneider et al. 2016; Ginolfi et al. 2018; Triani et al. 2020). The reformation of dust grains through the accretion of metals in dense ISM clouds is thought to provide the key to explaining the large amounts of interstellar dust observed in galaxies (e.g., Rowlands et al. 2014; Zhukovska 2014; Schneider et al. 2016; Zhukovska et al. 2016; De Vis et al. 2017b; Popping et al. 2017), but the exact physical processes that enable this type of "grain growth" in the interstellar medium remain poorly understood (Barlow 1978; Ferrara et al. 2016; Ceccarelli et al. 2018).

To better understand the main dust formation mechanisms in galaxies, and whether or not grain growth can dominate the dust production, we require substantial progress on two independent fronts. First of all, we need reliable estimates of the dust content in galaxies. In this work, we rely on a set of carefully determined dust masses (see Appendix A) inferred from fitting the mid-infrared to submillimetre dust spectral energy distribution (SED) with a Bayesian method that builds upon the grain mix and dust properties from the THEMIS dust model (Jones et al. 2017) and a multi-component interstellar radiation field heating these dust grains (Dale et al. 2001). Secondly, we require measurements of how the dust, metal and gas content in galaxies scales with respect to other global galaxy properties (i.e., stellar mass, specific star formation rate, metallicity) through scaling relations to infer how a galaxy's dust content evolves with time and to shed light on the main sources of dust production in the ISM. Understanding how the amount of dust, metals and gas evolves for a large ensemble of galaxies, at different stages of their evolution, will allow us to pin down the importance of various dust production and destruction mechanisms. Tracking how metals and dust are built up throughout a galaxy's lifetime necessitates simultaneously quantifying dust and gas reservoirs. The JINGLE (JCMT dust and gas In Nearby Galaxies Legacy Exploration) galaxy sample (Saintonge et al. 2018, hereafter JINGLE Paper I) was designed to acquire dust mass measurements from *Herschel* and SCUBA-2 data, in addition to ancillary HI observations, and molecular gas mass measurements currently available for 63 JINGLE galaxies.

In this paper, we present dust, gas and metal scaling relations for a sample of 423 nearby galaxies, including JINGLE, HRS, HAPLESS, HiGH and KINGFISH samples[1]. We split up this local galaxy sample into six subsamples according to their stage of evolution. We assume in this paper that the evolutionary stage of a galaxy is relatively well approximated by their $M_{\rm HI}/M_\star$ ratios and infer representative star formation histories according to the evolutionary stage of these galaxies. We compare the average dust, gas and metal mass fractions along these evolutionary sequences with a set of Dust and Element evolUtion modelS (DEUS) in a Bayesian framework in order to cover a large range of input parameters and to elucidate what processes drive these scaling laws. This is the first study (to our knowledge) where such a rigorous search of the full parameter space has been pursued.

Section 2 discusses the main characteristics of our five nearby galaxy samples (JINGLE, HRS, KINGFISH, HAPLESS, HIGH). In Section 3, we analyse the observed scaling laws for the dust, gas and metal content of these five galaxy samples. In Section 4, we subdivide our local galaxy sample into six bins according to their specific HI gas masses, and compare their average scaling laws with DEUS to infer how their dust and metal content has been built up across cosmic time. In Section 5, we summarise our conclusions. In the Appendices, we outline the method used to model the dust masses (Appendix A), detail the datasets and methods used to infer galaxy specific properties (Appendix B), describe how we infer customised star formation histories (SFH) for galaxies at different evolutionary stages (Appendix C), discuss the specifics of DEUS (Appendix D), while a list of acronyms and symbols is presented in Appendix F, and additional Tables and Figures are presented in Appendices E and G.

2 SAMPLE DESCRIPTION

2.1 An introduction to JINGLE

JINGLE is a large program on the James Clerk Maxwell Telescope (JCMT) aiming to assemble dust mass measurements for a sample of 193 local galaxies and molecular gas masses for part of this sample. The JINGLE sample populates the redshift range between z=0.01 and z=0.05, and was drawn from the MaNGA (Mapping Nearby Galaxies at Apache Point Observatory, Bundy et al. 2015) sample with optical integral-field spectroscopy data. In brief, JINGLE galaxies were selected to homogeneously sample the SFR–$M_\star$ plane between 10^9 and $10^{11}\,{\rm M}_\odot$. As part of the sample selection procedure, JINGLE galaxies were required to have detections in the *Herschel* SPIRE 250 and 350 μm bands. New JCMT SCUBA-2 850 μm (and 450 μm) observations probe the dust emission spectrum along the Rayleigh-Jeans tail (Smith et al. 2019, hereafter JINGLE Paper II), while RxA CO J=2-1 observations provide measurements of the molecular gas content (currently) for 63 JINGLE galaxies (Xiao et al. in prep., hereafter JINGLE Paper III). As a consequence of the sample selection, most JINGLE galaxies are classified as late-type spirals or irregular galaxies with a subset of only 7 early-type galaxies.

The sample selection and main science goals of the JINGLE survey are described in JINGLE Paper I, with specific details about the observational setup and data reduction of the RxA CO J=2-1 line spectroscopy and SCUBA-2 450 and 850 μm dust continuum observations presented in JINGLE Papers III and II, respectively. In Lamperti et al. (2019) (hereafter JINGLE Paper V), a hierarchical Bayesian fitting algorithm has been used to infer dust temperatures, dust emissivity indices, and dust masses for the ensemble of JINGLE (and HRS) galaxies. In this paper, we rely on the dust masses for JINGLE and the other nearby galaxies inferred from an alternative modelling method using a

[1] The combined galaxy sample consists of 568 galaxies. We consider the subsample of those galaxies: (1.) with available HI gas measurements, and (2.) classified as non-HI-deficient galaxies.

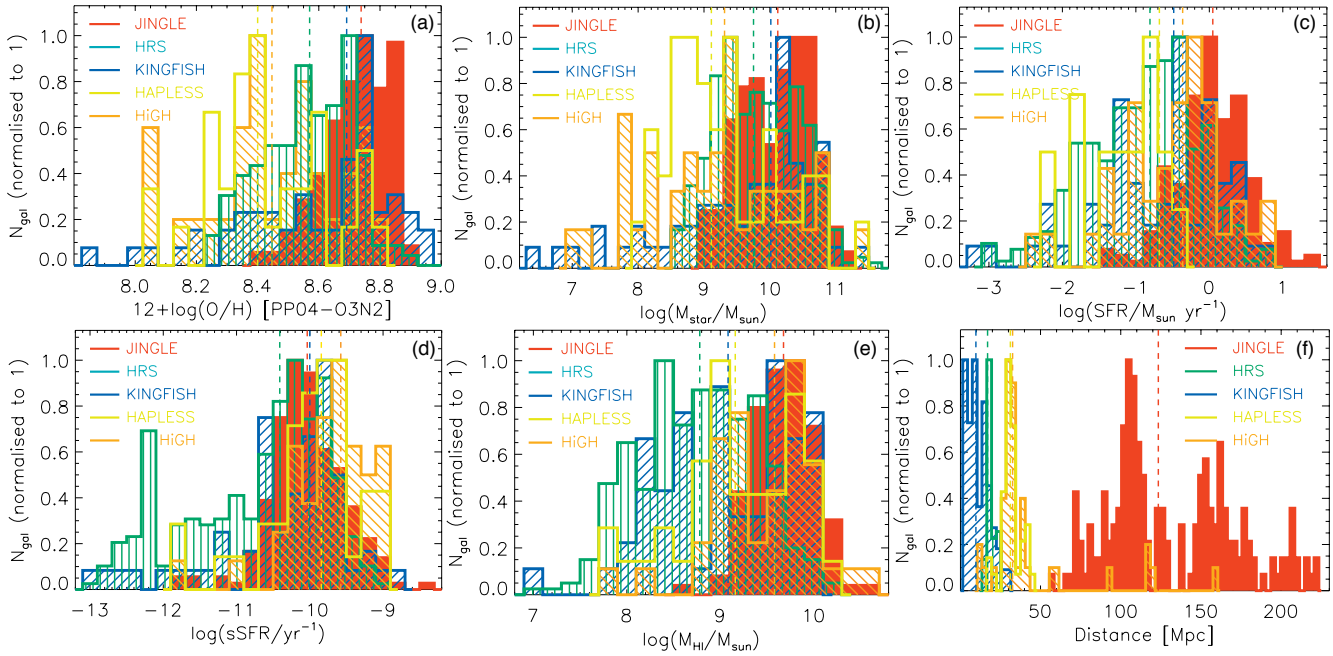

Figure 1. From left to right, and top to bottom: histograms of the metallicities (as traced by the oxygen abundance), stellar masses, star formation rates (SFRs), specific star formation rates (sSFRs), HI masses ($M_{\rm HI}$) and distances for the JINGLE (red filled histograms), HRS (green vertical lines), KINGFISH (blue diagonal lines), HAPLESS (yellow lines) and HiGH (orange diagonal lines) galaxies. Median sample values are indicated with vertical dashed lines using the same colour-coding.

non-hierarchical Bayesian implementation of the THEMIS dust model, that enables us to constrain the small grain size distribution, dust masses and starlight intensity distribution responsible for the dust heating (see Appendix A). We note that the dust masses inferred here and in JINGLE Papers V are in excellent agreement after considering the differences in the assumed dust mass absorption coefficients: JINGLE Paper V assumes κ_{500}=0.051 m^2 kg^{-1} (Clark et al. 2016), while here we adopt κ_{500}=0.185 m^2 kg^{-1} from the THEMIS dust model (Jones et al. 2013, 2017). Due to growing evidence (both from observations and laboratory experiments) indicating that interstellar dust is more emissive than considered in the previous generation of dust models (e.g., Planck Collaboration et al. 2016; Demyk et al. 2017a,b; Clark et al. 2019), we base our analysis upon the dust masses inferred with the THEMIS dust model to account for this increased dust emissivity and to avoid overestimating the dust masses for a set of observed flux densities (compared to the previous generation of dust models).

2.2 Nearby galaxy comparison samples

In addition to JINGLE, we have selected four nearby galaxy samples with well-studied dust characteristics and general galaxy properties. The combination of samples, whilst not statistical, allows the scaling relations in this paper to be explored over the widest possible extent of the parameter spaces in question.

The first sample consists of the galaxies from the *Herschel* Reference Survey (HRS, Boselli et al. 2010) which is a volume-limited, K-band selected sample of 322 nearby galaxies with distances between 15 and 25 Mpc. More than half of the HRS sample consists of cluster galaxies (residing in the Virgo and Ursa Major cluster), with the remaining galaxies located in massive groups surrounding these clusters. The second sample is composed of galaxies from the *Herschel* program KINGFISH (Key Insights on Nearby Galaxies: A Far-Infrared Survey with Herschel, Kennicutt et al. 2011) which consists of 61 nearby galaxies with distances $D \leq 30$ Mpc, covering a variety of different morphological classifications, star formation activity and galaxy environments. The third and fourth sample, HAPLESS and HiGH, were selected from the *Herschel* Astrophysical Terahertz Large Area Survey (H-ATLAS, Eales et al. 2010) based on their SPIRE 250 μm (HAPLESS, Clark et al. 2015) and HI (HiGH, De Vis et al. 2017a) detections, respectively. Since dusty galaxies often contain a considerable amount of gas, and vice versa, it is not surprising that the HAPLESS (42 galaxies) and HiGH (40 galaxies) samples have 22 sources in common. Average sample properties are summarised in Table 1, and are briefly discussed in Section 2.3. To compare properties of different galaxy samples, we have performed Mann–Whitney U–tests using the `RS_TEST` procedure in IDL (see Table E1 for the test results). This procedure tests the hypothesis that two samples have the same median of distribution at a significance level of 5%, with probabilities higher than this value indicative of both samples not being significantly different.

2.3 Sample characteristics

JINGLE and KINGFISH galaxies are more metal-rich as compared to other nearby galaxy samples (see Fig. 1a), whereas the oxygen abundance distributions for HRS, HAPLESS and HiGH samples are not considered to be significantly different. The JINGLE sample has a relatively flat

Table 1. Overview of the median values for a set of galaxy properties, with the error bars reflecting the dispersion observed for galaxies within a specific galaxy sample. For the HRS sample, we report the sample characteristics for the entire set of HRS galaxies, and the subsamples of HI-deficient and non-deficient (HI_{def} $\leq$0.5) HRS galaxies.

Quantity	JINGLE	HRS (all)	HRS (HI def<0.5)	HRS (HI def≥0.5)	KINGFISH	HAPLESS	HIGH
12+log(O/H)	8.74±0.10	8.58±0.15	8.57±0.15	8.64±0.13	8.69±0.22	8.44±0.17	8.50±0.20
log $M_\star$ [$M_\odot$]	10.13±0.55	9.67±0.63	9.53±0.59	9.95±0.64	9.95±0.98	9.06±0.64	9.39±0.86
log SFR [$M_\odot$ yr^{-1}]	0.052±0.48	-0.70±0.67	-0.47±0.56	-1.18±0.65	-0.48±0.85	-0.83±0.31	-0.24±0.54
log sSFR [yr^{-1}]	-10.03±0.49	-10.30±0.80	-10.08±0.51	-10.98±0.82	-10.0±0.63	-9.92±0.68	-9.72±0.50
log M_{HI} [$M_\odot$]	9.66±0.39	8.92±0.60	9.20±0.44	8.37±0.45	9.08±0.71	8.90±0.52	9.74±0.48
D [Mpc]	123.4±41.6	17.0±1.2	17.3±2.8	17.0±2.4	9.8±6.8	31.1±5.3	32.4±5.0
log $M_{dust}/M_\star$	-2.71±0.36	-2.90±0.43	-2.76±0.29	-3.19±0.55	-2.86±0.48	-2.82±0.46	-2.78±0.44
log $M_{HI}/M_\star$	-0.43±0.48	-0.76±0.75	-0.50±0.50	-1.49±0.66	-0.60±0.91	-0.35±0.69	0.02±0.61
log M_{dust}/M_{metals}	-0.67±0.23	-0.60±0.21	-0.62±0.21	-0.44±0.08	-0.63±0.38	-0.65±0.15	-0.78±0.30
log M_{dust}/M_{HI}	-2.25±0.31	-2.17±0.47	-2.28±0.35	-1.80±0.44	-2.30±0.69	-2.59±0.23	-2.61±0.45

stellar mass distribution (which was by selection, see Saintonge et al. 2018) with values ranging from 10^9 to 10^{11} $M_\odot$ (see Fig. 1b), significantly different from the other four nearby galaxy samples. The HRS, KINGFISH and HiGH samples extend towards low stellar masses with several galaxies in the 10^6-10^9 $M_\odot$ stellar mass range. HAPLESS does not contain galaxies with stellar masses below 10^8 $M_\odot$, nor does it contain many $M_\star > 10^{10}$ $M_\odot$ galaxies like JINGLE. Based on the mass-metallicity relation (e.g., Tremonti et al. 2004; Hughes et al. 2013; Sánchez et al. 2017), it is thus not surprising that JINGLE galaxies are characterised by the highest metal abundances among our local galaxy sample.

The median star formation rate (SFR) of JINGLE galaxies (1 $M_\odot$ yr^{-1}, see Fig. 1c) is similar to the average present-day star formation activity in our own Galaxy (Robitaille & Whitney 2010). SFRs are a factor of three lower in KINGFISH and HiGH galaxies, and lower by a factor of six in HRS and HAPLESS galaxies, than for JINGLE galaxies. The low SFRs and specific star formation rates (sSFRs) imply that the majority of HRS galaxies are undergoing a period of low star formation activity, and have built up the majority of their stellar mass content during earlier epochs. The subsample of more evolved HRS galaxies is also evident from the long tail in the sSFR diagram at the low sSFR end (see Fig. 1d). Although HiGH, KINGFISH and HAPLESS galaxies have a median SFR two, three and eight times lower than JINGLE, respectively, the similarity in their median sSFRs suggests that these samples contain several galaxies with elevated levels of recent star formation activity.

The HI mass content of JINGLE galaxies is similar to the median HI reservoirs present in the HI-selected HiGH sample, but the specific HI gas mass of HiGH galaxies (log $M_{HI}/M_\star$=0.02±0.61) is higher than for JINGLE (log $M_{HI}/M_\star$=-0.43±0.48). HiGH galaxies are therefore considered to be in a very early stage of galaxy evolution (De Vis et al. 2017a). Nonetheless, JINGLE HI masses are clearly higher than those of KINGFISH, HAPLESS and HRS galaxies, suggesting that JINGLE galaxies have retained a non-negligible part of their HI reservoir for future star formation, and are also at an earlier stage of galaxy evolution. It is worth noting that the spatial extent of the HI reservoir has not been taken into consideration in the comparison of these HI masses (due to the availability of single-dish measurements only), and that, in particular, low-mass metal-poor galaxies can have a large HI reservoir that extends well beyond the stellar body (e.g., Hunter et al. 2011). HRS galaxies have a median HI mass almost an order of magnitude below the median for JINGLE, which supports the interpretation of the HRS sample consisting of more evolved galaxies. A subset of the HRS galaxies have been characterised to be HI-deficient[2], and their reduced star formation activity has been attributed to the removal of part of their HI gas reservoir due to environmental processes that inhibit new stars from forming (e.g., Cortese et al. 2011).

The median distance of JINGLE galaxies (D=123.4 Mpc) is higher than the median distances (D=10-30 Mpc) for the other samples, which will likely bias the JINGLE sample selection to only include the dustiest galaxies at those distances.

Similar to the low fraction of early-type galaxies in the JINGLE sample (i.e., 3.6%), the HAPLESS and HiGH samples consist of late-type star-forming galaxies with a range of different morphologies (ranging from early-type spirals to bulgeless highly flocculent galaxies), with the exception of 2 early-type HAPLESS galaxies. The KINGFISH sample contains 10 early-type galaxies (E/S0/S0a), 22 early-type spirals (Sa/Sb/Sbc), 16 late-type spirals (Sc/Sd/Scd) and 13 irregular galaxies (I/Sm). The HRS sample contains a significant subpopulation of 23 elliptical and 39 spheroidal galaxies (Smith et al. 2012), with the remaining 261 galaxies classified as late-type galaxies.

3 DUST, GAS AND METAL SCALING LAWS

The main goal of this part of the paper is to analyse local dust, HI gas and metal scaling laws, to understand how the dust content and metallicity evolves over time, and what processes drive this evolution.

3.1 Dust scaling relations

With dust being formed through the condensation of metals synthesised in recent generations of stars, the dust content is closely linked to the stellar mass and star formation activity in galaxies. Since the stellar mass typically scales with the

[2] The HI-deficiency is calculated as the logarithmic difference between the expected and observed HI mass, i.e. HI def = log $M_{HI,ref}$ - log $M_{HI,obs}$, following the definition in Haynes & Giovanelli (1984).

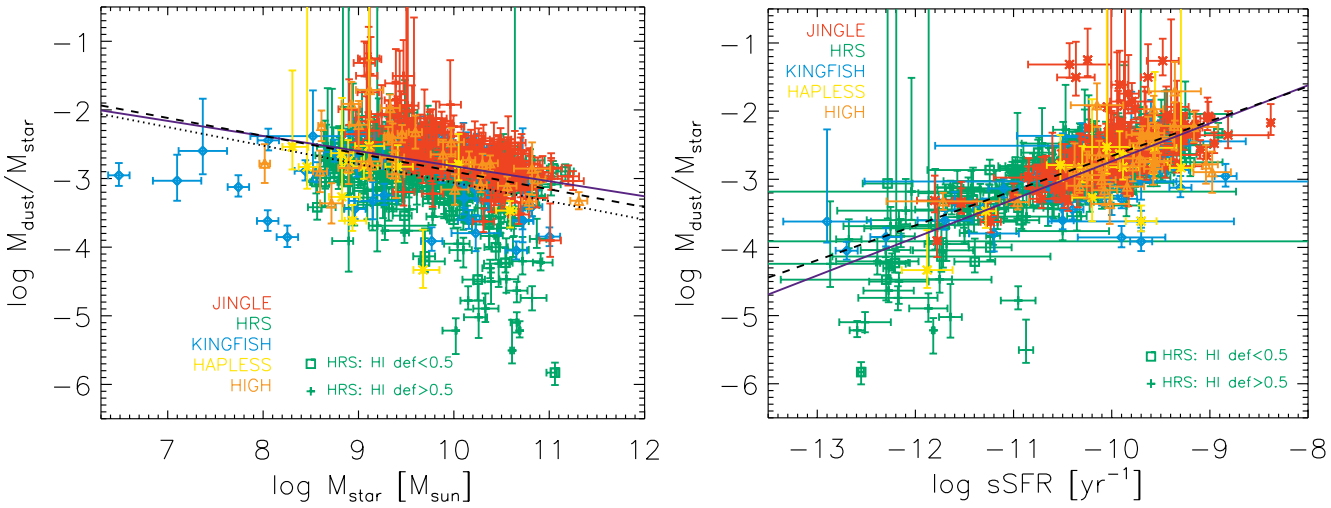

Figure 2. The scaling of the dust-to-stellar mass ratio (i.e., $M_{\rm dust}/M_\star$) with stellar mass ($M_\star$, left panel) and specific star formation rate (sSFR with sSFR=SFR/$M_\star$, right panel) is shown for JINGLE (red cross), HRS (green square/cross), KINGFISH (blue diamond), HAPLESS (yellow cross) and HiGH (orange triangle) galaxies. A distinction is made between HI-deficient and non-deficient HRS galaxies ($\rm H\,I_{def}$ $\leq$0.5, green square). Best-fit relations (as inferred for the entire nearby galaxy sample, with the exception of HI-deficient HRS galaxies) have been overlaid as a purple solid line, and are compared (where possible) to local galaxy scaling laws from De Vis et al. (2017a) (black dashed curve) and from Casasola et al. (2019) (black dotted curve). The scaling relation from De Vis et al. (2017a) was adjusted to account for the difference in the assumed dust opacities.

metal richness of the interstellar medium (through the stellar mass-metallicity relation, e.g., Tremonti et al. 2004), the dust-to-stellar mass ratio can be interpreted as the ratio of metals locked into dust grains versus the metals in the gas phase. It is known that specific dust masses ($M_{\rm dust}/M_\star$) decrease towards high stellar masses (see Fig. 2, left panel) due to dust destruction dominating over dust production processes in more massive systems. The latter trend can also be understood in view of the downsizing of galaxies (e.g., Cowie et al. 1996), where most of the massive galaxies already converted most of their gas into stars, and the bulk of dust mass was formed during these main star formation episodes. The wide spread in log $M_{\rm dust}/M_\star$ ratio from -2.5 to -5 that we find for galaxies with stellar masses $M_\star$=10^{10}-10^{11} $\rm M_\odot$ is a reflection of galaxies with similar stellar masses but at different stages of evolution.

JINGLE galaxies populate the high end of the $M_{\rm dust}/M_\star$ range at a given stellar mass. Their high log $M_{\rm dust}/M_\star$ ratios (-2.71$\pm$0.36) are not surprising considering that JINGLE galaxies were selected from their detections in the *Herschel* SPIRE bands (Saintonge et al. 2018). The JINGLE galaxies have $M_{\rm dust}/M_\star$ ratios similar to (or even slightly higher than) the majority of dust- and HI-selected HAPLESS/HiGH galaxies in the stellar mass range that those samples have in common. Several KINGFISH and HAPLESS/HiGH galaxies with stellar masses $M_\star$ $\leq$$10^9$ $\rm M_\odot$ are characterised by low $M_{\rm dust}/M_\star$ ratios, and deviate from the general trend for more massive galaxies. The HAPLESS/HiGH galaxies with low specific dust masses were identified by De Vis et al. (2017a) as a unique population of galaxies, at an extremely early phase of evolution where most of the dust still needs to be formed. H I-deficient HRS galaxies populate the bottom part of the diagram with systematically lower $M_{\rm dust}/M_\star$ ratios in comparison to other nearby galaxies. The lower $M_{\rm dust}/M_\star$ for H I-deficient galaxies suggests that these galaxies have had part of their dust content stripped along with their H I gas content (see also Cortese et al. 2014), or that star formation has ceased in these objects a long time ago, resulting in a lack of recent dust replenishment, with dust destruction processes further diminishing their dust content. Our best-fit relation is very similar compared to the best-fit relation from De Vis et al. (2017a) (inferred for HRS, HAPLESS and HiGH late-type galaxies). The relation inferred by Casasola et al. (2019) for a sample of 436 late-type local DustPedia galaxies is lower by up to 0.2 dex, which can likely be attributed to a selection effect. Our sample includes dust-selected galaxies at larger distances (see Fig. 1f), which are likely to be more dusty on average compared to a local galaxy sample.

The importance of recent star formation activity to determine a galaxy's dust content is evidently shown from the scaling of $M_{\rm dust}/M_\star$ with sSFR (see Fig. 2, right panel). Independent of their morphological classification, all galaxies follow a similar trend of decreasing $M_{\rm dust}/M_\star$ towards low sSFR over three orders of magnitude in both quantities. The tight correlation (ρ=0.63) between $M_{\rm dust}/M_\star$ and sSFR was first shown by da Cunha et al. (2010) for a sample of nearby galaxies. The fact that dust-selected samples such as JINGLE and HAPLESS follow the same trend as the stellar-mass selected HRS sample indicates that sSFR is a more fundamental parameter than $M_\star$ to determine the specific dust mass of a galaxy (either directly or through a secondary correlation).

The present-day dust mass of a galaxy is set by the balance between the sources producing dust (i.e., evolved stars, supernovae, grain growth) and the sinks destroying dust grains (i.e., astration, supernova shocks). The observed correlation between $M_{\rm dust}/M_\star$ and sSFR could be a reflection of an equilibrium process where the amount of dust grains formed/destroyed scales with the recent star formation activity in a galaxy. Alternatively, the relation of the $M_{\rm dust}/M_\star$ with sSFR can be interpreted as an indirect mea-

sure of the total gas mass in a galaxy which is known to scale with the star formation rate through the Kennicutt-Schmidt relation (Schmidt 1959; Kennicutt 1998). Given that the $M_{\rm HI}/M_\star$ ratio dominates the scatter in local scaling relations with $M_\star$ and sSFR (see also Section 3.2), and correlates strongly with the observed $M_{\rm dust}/M_\star$, $M_{\rm dust}/M_{\rm metals}$ and $M_{\rm dust}/M_{\rm HI}$ ratios in our local galaxy samples, we favour the latter interpretation (see below).

3.2 HI gas scaling relations

With dust grains making up about 1% of the ISM in mass, the gas reservoir dominates the ISM budget of a galaxy. In this paper, we will make the assumption that galaxies with massive HI reservoirs (compared to their $M_\star$) are considered to be at an early stage of evolution, while a low gas content is indicative of an evolved galaxy which had most of its gas reservoir turned into stars already. The $M_{\rm HI}/M_\star$ ratio in Fig. 3 (left panel) shows a similar anti-correlation (ρ=−0.64) with stellar mass as the $M_{\rm dust}/M_\star$ ratio in Fig. 2 (left panel) which is consistent with the least massive galaxies having the largest atomic gas reservoir proportional to their stellar mass.

Our best-fit relation for the specific HI gas mass as a function of stellar mass is shifted upwards by 0.3 to 0.4 dex compared to the trend from De Vis et al. (2017a) due to the high specific HI gas masses of JINGLE galaxies, and due to our omission of HI-deficient HRS galaxies to determine the best-fit relation. The scatter observed in the relations of $M_{\rm HI}/M_\star$ with $M_\star$ (σ=0.57) and sSFR (σ=0.40) dominates over the dispersion in the respective trends of $M_{\rm dust}/M_\star$ with $M_\star$ (σ=0.39) and sSFR (σ=0.29), which suggests that the scatter in the trends of $M_{\rm dust}/M_\star$ with $M_\star$ and $sSFR$ are likely dominated by variations in the galaxy's specific HI gas masses, and not necessarily directly influenced by the various dust production and destruction mechanisms at work in these galaxies. This scenario is also supported by the scatter observed in the scaling laws (see Fig. 4) for $M_{\rm dust}/M_{\rm HI}$ with $M_\star$ (σ=0.33) and sSFR (σ=0.37), which is lower than similar relations for $M_{\rm HI}/M_\star$ and suggests that the specific HI gas mass dominates the scatter in these scaling relations. The trends between $M_{\rm HI}/M_\star$, and $M_{\rm dust}/M_\star$ ($\rho = 0.67$), $M_{\rm dust}/M_{\rm metals}$ ($\rho = -0.61$) and $M_{\rm dust}/M_{\rm HI}$ ($\rho = -0.72$) furthermore show strong correlations (see Fig. 8 and Table 2) compared to the relations of the latter ratios with $M_\star$ or $sSFR$, reinforcing the above reasoning. To study what processes drive the observed trends and scatter in local scaling laws, we therefore verify how the dust and metal content of these galaxies varies as a function of $M_{\rm HI}/M_\star$ in Section 4.

3.3 Dust-to-HI ratios

The $M_{\rm dust}/M_{\rm HI}$ ratio (or dust-to-gas ratio, if the contribution from molecular gas can be marginalised[3]) of a galaxy measures how many metals have been locked up in dust grains compared to the metals in the gas phase. To verify the reliability of this proxy, we plot the $M_{\rm dust}/M_{\rm metals}$ ratio (see Section 3.4) as a function of the $M_{\rm dust}/M_{\rm HI}$ ratio in Figure 7 (right panel), which shows a strong correlation ($\rho = 0.88$) with little scatter ($\sigma = 0.11$) around the best-fit trend.

The $M_{\rm dust}/M_{\rm HI}$ ratios of our nearby galaxy samples range between $10^{-1.1}$ and $10^{-4.3}$ with a median $10^{-2.3\pm0.4}$ (see Figure 4) which is roughly consistent with the Milky Way dust-to-HI gas column density ratio assumed in the THEMIS dust model (1/135, Jones et al. 2017). The $M_{\rm dust}/M_{\rm HI}$ ratio decreases with decreasing stellar mass (ρ=0.51), and with increasing sSFR (ρ=−0.41), which is consistent with the consensus that less massive galaxies are currently in the process of vigorously forming stars, and that most of their metals have not been locked up in dust grains in comparison to the large reservoir of gas. In particular, HAPLESS ($\log M_{\rm dust}/M_{\rm HI}$=−2.59 ± 0.23) and HiGH ($\log M_{\rm dust}/M_{\rm HI}$=−2.61 ± 0.45) galaxies have median ratios at the low end of the entire nearby galaxy population, which might at first seem surprising given their "normal" $M_{\rm dust}/M_\star$ ratios. Similar trends were found by da Cunha et al. (2010) and consecutive works (Cortese et al. 2012; Clark et al. 2015; De Vis et al. 2017a), and attributed to galaxies with low stellar masses and high sSFRs, currently forming dust (high $M_{\rm dust}/M_\star$), and still retaining large HI gas reservoirs (low $M_{\rm dust}/M_{\rm HI}$) for future star formation. JINGLE ($\log M_{\rm dust}/M_{\rm HI}$=−2.25±0.31) and KINGFISH ($\log M_{\rm dust}/M_{\rm HI}$=−2.30 ± 0.69) galaxies have ratios that agree well with the general trend observed for the ensemble of nearby galaxies, while the overall HRS sample median ($\log M_{\rm dust}/M_{\rm HI}$=−2.17 ± 0.47) is increased due to the high ratios ($\log M_{\rm dust}/M_{\rm HI}$=−1.80 ± 0.44) observed for HI-deficient HRS galaxies. The latter high ratios agree with the findings of Cortese et al. (2016), and were attributed to the outside-in stripping of the interstellar medium in these HI-deficient HRS galaxies (where the extended HI component is affected more than the dust and molecular gas). The lowest ratios ($-4.3 \leq M_{\rm dust}/M_{\rm HI} \leq -3.9$) have been observed for four irregular KINGFISH galaxies (NGC 2915, HoII, DDO053, NGC 5408) characterised by low stellar masses, low metal abundances, high sSFRs, high specific HI gas masses and low specific dust masses, which makes them stand out from the average KINGFISH galaxy population and characterises these galaxies as being at an early stage of evolution.

Trends of dust-to-gas ratios with metallicity reported in the literature show that the $M_{\rm dust}/M_{\rm HI}$ ratio is strongly linked to the evolutionary stage of galaxies with gradually more metals being locked up in dust grains (e.g., Rémy-Ruyer et al. 2014). The relation between $M_{\rm dust}/M_{\rm HI}$ as a function of oxygen abundance is shown in Figure 5, and is best-fitted with a super-linear trend (slope: 2.26 ± 0.07). For reference, the linear relation (with a fixed slope of 1) and super-linear trend (with a slope of 2.02 ± 0.28) from Rémy-Ruyer et al. (2014) are overlaid as yellow solid and dashed

[3] We note that for 44 KINGFISH and 81 HRS galaxies with CO data the median H_2/HI ratio is equal to 0.62 and 0.31, respectively, assuming a Galactic $X_{\rm CO}$ factor. For a metallicity- and luminosity-dependent $X_{\rm CO}$ factor, the median H_2/HI ratio for KINGFISH and HRS galaxies changes to 1.90 and 0.30, respectively. For HRS galaxies, these values are in line with the average $M_{\rm H_2}/M_{\rm HI}$ ratio of 0.3 for xGASS galaxies with stellar masses above 10^{10} $M_\odot$ (Catinella et al. 2018).

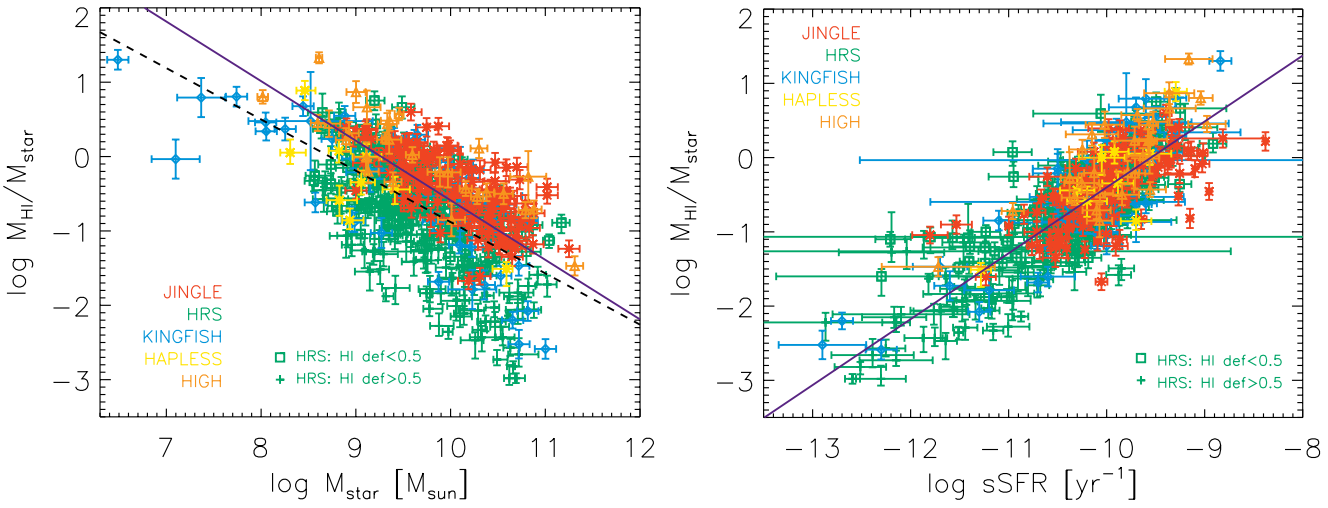

Figure 3. The scaling of the HI-to-stellar mass ratio (i.e., $M_{\rm HI}/M_\star$) with stellar mass ($M_\star$, left panel) and specific star formation rate (sSFR with sSFR=SFR/$M_\star$, right panel). See caption of Fig. 2 for more details on the symbols and plotted curves.

Table 2. The best-fit relations (of the form $y = a \times x + b$) have been inferred based on linear regression fits using the IDL procedure `MPFITEXY`, which is based on the non-linear least-squares fitting package MPFIT (Markwardt 2009). In addition to JINGLE, KINGFISH, HAPLESS and HiGH galaxies, only HRS galaxies with an HI-deficiency lower than 0.5 (i.e., classified as non-deficient galaxies) have been considered. The observed scatter (σ) around each of the best-fit relations has been inferred. The Spearman rank correlation coefficient, ρ, and corresponding p value have been inferred from the IDL procedure `r_correlate` to quantify the degree of (non-)linear correlation between the various quantities.

x	y	a	b	σ	ρ	p value
$\log M_\star$	$\log M_{\rm dust}/M_\star$	-0.22±0.01	-0.62±0.11	0.39	-0.39	$< 10^{-6}$
$\log M_\star$	$\log M_{\rm HI}/M_\star$	-0.80±0.01	7.42±0.12	0.57	-0.64	$< 10^{-6}$
$\log M_\star$	$\log M_{\rm dust}/M_{\rm HI}$	0.47±0.01	-6.90±0.11	0.33	0.51	$< 10^{-6}$
$\log M_\star$	$\log M_{\rm dust}/M_{\rm metals}$	0.19±0.01	-2.54±0.09	0.24	0.26	$< 10^{-6}$
log sSFR	$\log M_{\rm dust}/M_\star$	0.56±0.01	2.85±0.15	0.29	0.63	$< 10^{-6}$
log sSFR	$\log M_{\rm HI}/M_\star$	0.89±0.02	8.47±0.15	0.40	0.72	$< 10^{-6}$
log sSFR	$\log M_{\rm dust}/M_{\rm HI}$	-0.28±0.01	-5.08±0.10	0.37	-0.41	$< 10^{-6}$
log sSFR	$\log M_{\rm dust}/M_{\rm metals}$	-0.29±0.01	-3.54±0.11	0.24	-0.32	$< 10^{-6}$
Metallicity	$\log M_{\rm dust}/M_{\rm HI}$	2.27±0.06	-21.89±0.55	0.34	0.53	$< 10^{-6}$
Metallicity	$\log M_{\rm dust}/M_{\rm metals}$	0.40±0.14	-4.10±1.18	0.26	0.11	4×10^{-2}
$\log M_{\rm HI}/M_\star$	$\log M_\star$	-1.25±0.01	9.27±0.01	0.51	-0.65	$< 10^{-6}$
$\log M_{\rm HI}/M_\star$	$\log M_{\rm dust}/M_\star$	0.49±0.02	-2.55±0.01	0.28	0.67	$< 10^{-6}$
$\log M_{\rm HI}/M_\star$	$\log M_{\rm dust}/M_{\rm metals}$	-0.37±0.01	-0.84±0.01	0.20	-0.61	$< 10^{-6}$
$\log M_{\rm HI}/M_\star$	Metallicity	-0.25±0.01	8.54±0.01	0.15	-0.55	$< 10^{-6}$
$\log M_{\rm HI}/M_\star$	$\log M_{\rm dust}/M_{\rm HI}$	-0.63±0.01	-2.63±0.01	0.28	-0.72	$< 10^{-6}$
$\log M_{\rm dust}/M_{\rm HI}$	$\log M_{\rm dust}/M_{\rm metals}$	0.61±0.02	0.75±0.04	0.11	0.88	0.0

lines[4]. Our trend is consistent with the super-linear relation from Rémy-Ruyer et al. (2014), which might seem surprising at first as the linear relation from Rémy-Ruyer et al. (2014) was found adequate to explain the trends at metallicities $12+\log({\rm O/H}) \gtrsim 8$ and the super-linear trend was invoked to explain the behaviour at metallicities lower than this threshold. A χ^2 goodness-of-fit test confirms that the linear fit from Rémy-Ruyer et al. (2014) does not provide a good fit to the data (p-value of 1), even when excluding galaxies below a metallicity threshold of 12+log(O/H)=8.4. The p-value (0.25) inferred from our best-fit suggests that the data are neither well described by a non-linear relation, which likely results from the limited metallicity range covered by our sample, and the large degree of scatter in the relation (σ=0.34). We furthermore compare our best-fit relation to the super-linear trend (slope of 2.15±0.11) inferred by De Vis et al. (2019) for a sample of ∼500 DustPedia galaxies for the same metallicity "PP04" calibration[5], but they included an estimation of the molecular gas content. The slope of our relation agrees well with their super-linear trend, but is offset by 0.2-0.3 dex to higher dust-to-HI ratios, which can likely be attributed to the omission of the molecular gas content in our galaxy samples and/or to the different samples under study in both works. In another DustPedia paper, a

[4] Note, that we are only interested in a comparison of their slopes, as the normalisation of these curves can not be directly compared to our values due to the differences in the assumed metallicity calibration, scaling factor for the gas mass to include heavier elements and dust opacities.

[5] Note that the use of a different metallicity calibration would still yield a super-linear trend, but with a slightly different slope and/or normalisation (see Table 4 from De Vis et al. 2019).

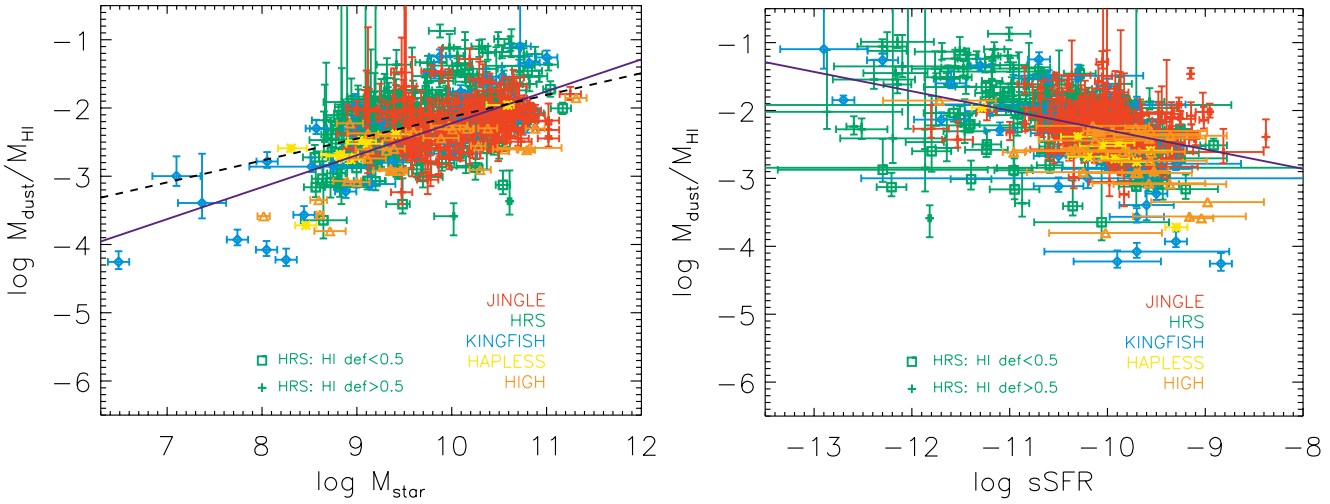

Figure 4. The scaling of the dust-to-HI mass ratio (i.e., $M_{\rm dust}/M_{\rm HI}$) with stellar mass ($M_\star$, left panel) and specific star formation rate (sSFR with $sSFR = SFR/M_\star$, right panel). See caption of Fig. 2 for more details on the symbols and plotted curves.

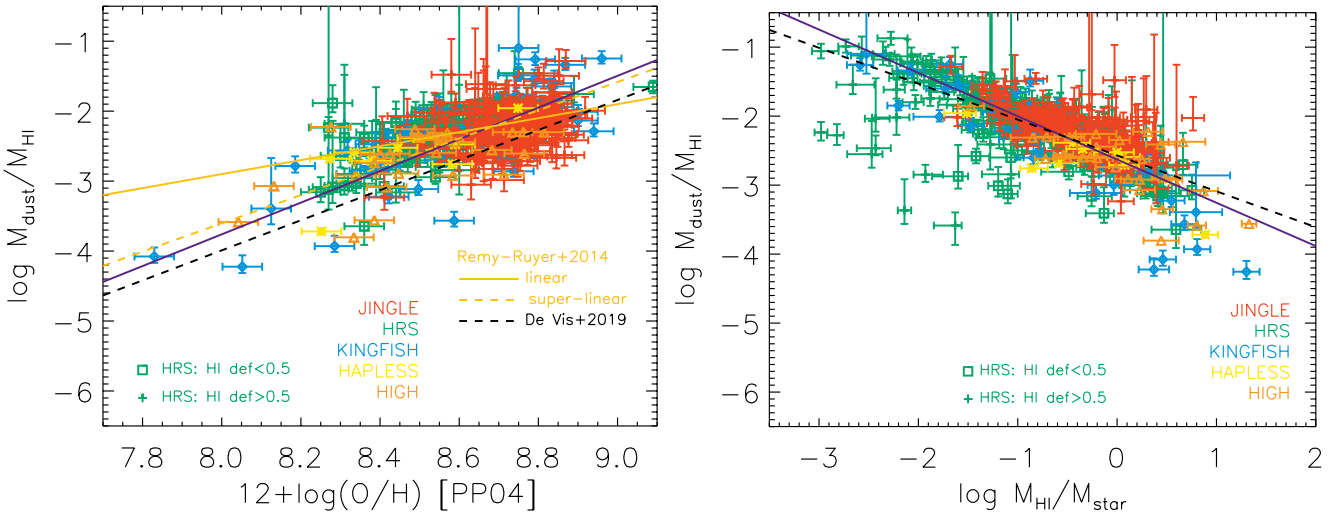

Figure 5. The scaling of the dust-to-HI mass ratio (i.e., $M_{\rm dust}/M_{\rm HI}$) with metallicity (as traced by the oxygen abundance 12+log(O/H)) and the specific HI gas mass (i.e., $M_{\rm HI}/M_\star$). See caption of Fig. 2 for more details on the symbols and plotted curves.

metallicity-dependent $X_{\rm CO}$ factor is invoked to reproduce a linear relation between the dust-to-gas ratio and metallicity Casasola et al. (2019), as frequently observed both on resolved and integrated galaxy scales in the local Universe (e.g., Lisenfeld & Ferrara 1998; Galametz et al. 2011; Magrini et al. 2011; Sandstrom et al. 2013). In future work, we will study the total gas scaling relations for JINGLE galaxies, and investigate the effect of different assumptions on the $X_{\rm CO}$ conversion factor. In the next paragraphs, we discuss the applicability of dust as a gas tracer based on the HI gas scaling relations of this work.

Dust mass measurements are often advocated as an alternative probe of the total ISM mass budget (e.g., Eales et al. 2012; Magdis et al. 2012; Scoville et al. 2014; Groves et al. 2015; Scoville et al. 2016; Janowiecki et al. 2018), due to the relative ease of obtaining infrared data and inferring dust masses, as opposed to a combination of HI data (for which the sensitivity quickly drops at high redshifts) and CO observations (hampered by the notorious CO-to-H_2 conversion factor, Bolatto et al. 2013).

Figure 5 shows that there is a considerable spread (0.34 dex) in the $M_{\rm dust}/M_{\rm HI}$ ratio as a function of oxygen abundance. The use of dust as an ISM mass tracer relies on the assumption of an approximately constant dust-to-gas ratio to convert dust masses into total gas masses. Variations of the dust-to-gas ratio with metallicity have been demonstrated before (e.g., Rémy-Ruyer et al. 2014), but the scatter around the best-fit in Figure 5 implies that the dust-to-HI ratio already varies by more than a factor of two at fixed metallicity. In most cases, the metal abundances of galaxies are not known a priori, and the uncertainty on the estimated ISM mass reservoir will be higher than this factor of two. Also the use of oxygen as a tracer of the total metal mass in galaxies might introduce an increased level of scatter. Some of the scatter in our relation might be caused by the missing molecular gas mass measurements; although Casasola et al.

(2019) find that the HI gas mass correlates more closely to the dust mass than the molecular gas. Part of the spread might furthermore be attributed to the inhomogeneous extent of dust and gas reservoirs tracing different parts of a galaxy. In particular, JINGLE galaxies may be affected by the unresolved extent of HI gas observations obtained from single-dish observations. In due course, all JINGLE galaxies will be covered by future interferometric radio facilities (e.g., SKA, Apertif), which will give us a handle on the spatial extent of their HI gas reservoir. JINGLE, HAPLESS and HiGH metallicities have furthermore been derived from the central 3″ covered by SDSS fibre optical spectroscopy data (Thomas et al. 2013), which could potentially increase the uncertainty on their oxygen abundances due to the lack of a set of spatially resolved metallicity measurements, as opposed to the resolved metallicity measurements for the other nearby galaxy samples. Due to the wide spread in metallicity gradients observed in local galaxy samples (e.g., Kennicutt et al. 2003; Moustakas et al. 2010; Sánchez-Blázquez et al. 2014; Belfiore et al. 2017; Poetrodjojo et al. 2018; An 2019), these central metallicity measurements will not necessarily be representative of a galaxy's average metal abundance. Metallicity measurements (in particular at low metallicity) furthermore come with large uncertainties due to the specific metallicity calibration that was applied, and its dependence on a fixed electron temperature in case of strong line calibrations. In addition, variations in the dust emissivity driven by an altered dust mineralogy or variations in carbon-to-silicate grain fractions (e.g., Clark et al. 2019) may be the cause of part of the scatter.

Janowiecki et al. (2018) argued that most of the scatter in the $M_{\rm dust}/M_{\rm HI}$ relation is driven by the unknown partition between atomic and molecular gas, and variations in the H_2-to-HI ratio with galaxy properties. Their study of the HRS galaxy sample suggests a dispersion of 0.22-0.25 dex in the relation between $M_{\rm dust}/M_{\rm HI}$ and metallicity, which is somewhat lower than the 0.34 dex scatter inferred for the sample of nearby galaxies in this paper.

3.4 Dust-to-metal ratios

We have calculated the dust-to-metal ratios (DTM) as the ratio of the dust mass and the total amount of metals (and thus accounting for metals in the gas phase and locked up in dust grains) similar to other literature works (e.g., De Vis et al. 2019):

$$DTM = M_{\rm dust}/M_{\rm metals}(gas + dust), \quad (1)$$

with $M_{\rm metals}$(gas+dust)=$f_{\rm Z} \times M_{\rm gas}$+$M_{\rm dust}$. This prescription allows for a direct comparison with the measurements of dust depletion in damped Lyman α absorbers out to large redshifts (e.g., De Cia et al. 2016). The metal mass fraction $f_{\rm Z}$ is calculated based on a galaxy's oxygen abundance, and the values of the metal mass fraction ($f_{Z_\odot}$=0.0134) and oxygen abundance (12+log(O/H)$_\odot$=8.69) inferred for the Sun from Asplund et al. (2009), which results in $f_{\rm Z}$=27.36×$10^{12+\log(O/H)-12}$. Due to the lack of molecular gas mass estimates, we have used the HI gas mass (corrected for the contribution from elements heavier than hydrogen, see Eq. D5) to calculate the metal mass fractions. We inferred that the dust-to-metal ratios are lower by -0.11 dex and -0.19 dex for 81 HRS and 44 KINGFISH galaxies, respectively, if we account for molecular gas masses assuming a Galactic $X_{\rm CO}$ conversion factor. A metallicity-dependent $X_{\rm CO}$ conversion factor would lower the dust-to-metal ratios by -0.46 dex for the KINGFISH sample (which contain the lowest metallicity galaxies in our local galaxy sample). It is worth noting that the metal mass furthermore relies on measurements of the oxygen abundance, which does not necessarily scale linearly to the total mass of metals in galaxies at different stages of evolution.

The DTM ratio provides a measure of the relative fraction of metals in the interstellar medium that have been locked up in dust grains, and therefore sensitively depends on the efficiency of various dust production and destruction mechanisms. It is assumed that the dust-to-metal ratio remains more or less constant if dust is predominantly produced via stellar sources[6]. If grain growth dominates the dust production, the DTM ratio is thought to increase as galaxies evolve and their interstellar medium is enriched with metals[7], with grain growth believed to be more efficient than stellar dust production sources once a critical metallicity threshold has been reached (Asano et al. 2013). Dust destruction through supernova shocks (where metals locked up in dust grains are returned to the interstellar medium) have the opposite effect and will lower the DTM ratio.

The majority of nearby galaxies fall within the same range of DTM ratios ($-0.90 \leq \log DTM \leq -0.40$), with little variation among the different galaxy populations (see Table 1 and Fig. 6). The Milky Way is situated on the high end of this range with log DTM=-0.45, if we have assume a total gas mass $M_{\rm gas}$=12.5×10^9 M$_\odot$ (Kalberla & Kerp 2009), solar metallicity and dust-to-HI ratio of 1/135 as inferred from the Milky Way THEMIS model (Jones et al. 2017). The median ratio for HiGH galaxies (log DTM=-0.78±0.30) is slightly lower than the other galaxy populations (but not significantly different, see Table E1) and confirms their early stage of evolution. The second lowest ratio (log DTM=-0.67±0.23) is observed for JINGLE galaxies, but similarly does not differ significantly from HAPLESS (log DTM=-0.65±0.15) and KINGFISH (log DTM=-0.63±0.38) galaxies. The median ratio for HRS galaxies (log DTM=-0.60±0.21) is significantly higher than for the other four samples due to the contribution from HI-deficient HRS galaxies, with the latter being characterised by significantly higher ratios (log DTM=-0.44±0.08). This DTM is more than 60% higher than the median DTM observed in our sample of nearby galaxies (log DTM=-0.66±0.24, excluding the HI-deficient HRS galaxies). This high DTM ratio appears consistent with the high $M_{\rm H_2}/M_{\rm dust}$ ratios observed in HI-deficient HRS galaxies (Cortese et al. 2016), and a picture of outside-in stripping of interstellar material where metals and HI are more easily stripped compared to the more centrally concentrated dust and molecular gas content. The median ratio for our nearby galaxy sample is higher than the average log DTM=-0.82±0.23 from De Vis

[6] This statement relies on the assumption that stellar dust yields, dust condensation efficiencies and reverse shock destruction rates do not have a strong metallicity dependence.
[7] This inference is somewhat model dependent, and is also influenced by grain destruction efficiencies.

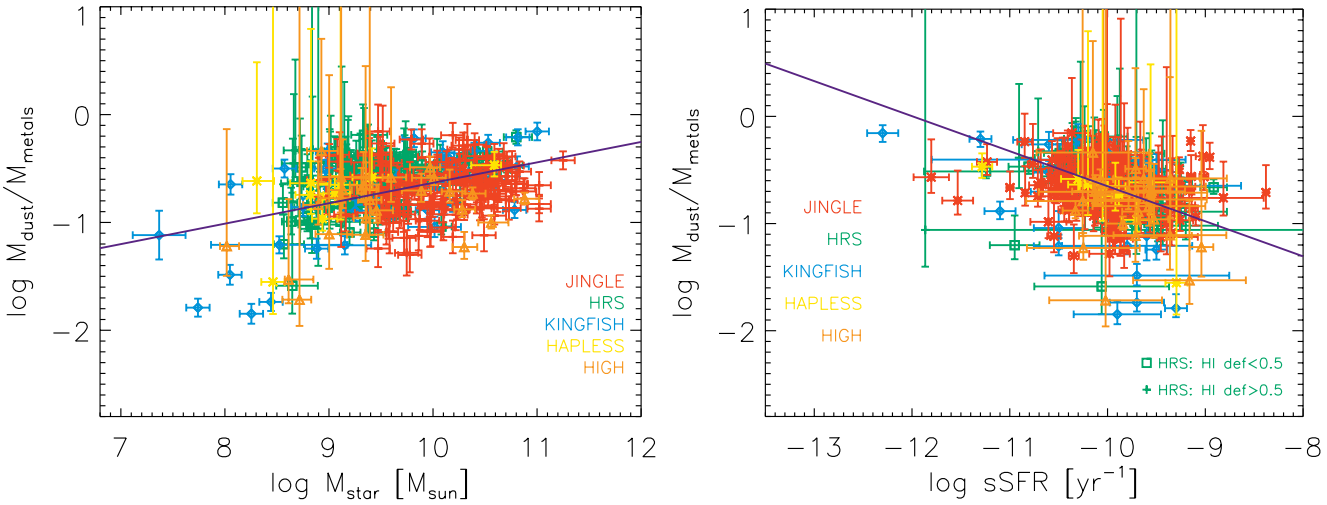

Figure 6. The scaling of the dust-to-metal mass ratio (i.e., $M_{\rm dust}/M_{\rm metals}$) with stellar mass ($M_\star$, left panel) and specific star formation rate (sSFR with $sSFR = SFR/M_\star$, right panel). See caption of Fig. 2 for more details on the symbols and plotted curves.

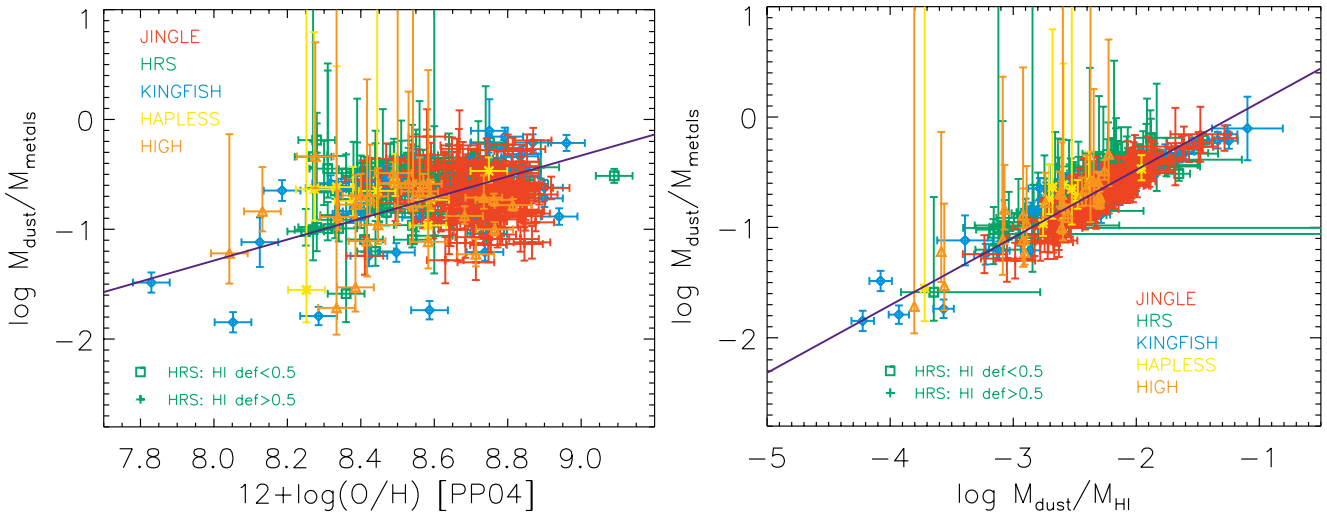

Figure 7. The scaling of the dust-to-metal mass ratio (i.e., $M_{\rm dust}/M_{\rm metals}$) with oxygen abundance (12+log(O/H), left panel) and dust-to-HI mass ratio (i.e., $M_{\rm dust}/M_{\rm HI}$, right panel). See caption of Fig. 2 for more details on the symbols and plotted curves.

et al. (2019), which we attribute to the fact that we did not consider molecular hydrogen measurements. Indeed, we discussed earlier that neglecting the molecular gas content will overestimate the DTM ratios by 0.11 dex up to 0.46 dex.

We observe weak (but significant) correlations between the DTM and $M_\star$ (ρ=0.26), sSFR (ρ=−0.32) and $M_{\rm HI}/M_\star$ (ρ=−0.61) (see Fig. 6 and 8), while the relation with metallicity does not reveal a clear trend (ρ=0.11, see Fig. 7, left panel). These weak correlations suggest that the DTM increases as a galaxy evolves, although there is quite some scatter in these relations. In particular, galaxies with $M_\star \geq 10^9 {\rm M}_\odot$ appear characterised by a nearly constant DTM, while the DTM drops significantly for several low mass galaxies ($M_\star < 10^9 {\rm M}_\odot$). This sudden change in DTM becomes particularly evident for less evolved galaxies with $\log M_{\rm HI}/M_\star > 0.3$ (see Fig. 8, bottom right panel), and has been attributed in the past to a critical metallicity threshold above which grain growth becomes efficient and contributes significantly to the dust production in galaxies (e.g., Asano et al. 2013). The absence of a clear trend with metallicity due to the large scatter in DTM ratios at low metallicities might suggest that this critical metallicity threshold can vary from one galaxy to another (Asano et al. 2013) or, alternatively, that such a critical metallicity threshold is not relevant[8]. In Section 4, we show that efficient grain growth is not required as a dominant dust production source to explain the current dust budgets of nearby galaxies with $-1.0 \lesssim \log M_{\rm HI}/M_\star \lesssim 0$. With supernova shock destruction releasing elements back into the gas phase, a wide range of DTM ratios (at fixed metallicity) can also result from variations in dust destruction efficiencies and/or recent supernova

[8] We should note that the metallicity range in our local galaxy sample is limited (with only one galaxy below 12+log(O/H)<8.0) and might not reach down to the metallicity regime where a threshold would occur.

rates. Also the structure of the interstellar medium, and the filling factor of different ISM phases can play an important role in determining how efficiently grains can grow in the interstellar medium, and how effectively supernova shocks can act as dust destroyers (Jones & Nuth 2011), and will add to the scatter.

To summarise our observational findings from these scaling relations, we infer that $M_{\rm HI}/M_\star$ varies considerably at a fixed stellar mass and fixed sSFR, more so than the $M_{\rm dust}/M_\star$ and $M_{\rm dust}/M_{\rm HI}$ ratios. This large spread can be interpreted as the specific HI gas mass being the main driver of the trends and scatter observed in other scaling laws (rather than variations in the relative contributions from several dust formation and destruction processes at fixed stellar mass or sSFR). This picture is reinforced by the significant correlations between $M_{\rm HI}/M_\star$, and $M_{\rm dust}/M_\star$, $M_{\rm dust}/M_{\rm metals}$(gas+dust) and $M_{\rm dust}/M_{\rm HI}$ (see Figure 8) and establishes that $M_{\rm HI}/M_\star$ is closely linked to the enrichment of the interstellar medium with dust and metals, and the evolution of a galaxy, in general. In Section 4, we will interpret the evolutionary trends for $M_{\rm dust}/M_\star$, $M_{\rm dust}/M_{\rm HI}$ and $M_{\rm dust}/M_{\rm metals}$(gas+dust) using a set of chemical evolution models to infer what dust production and destruction mechanisms have contributed to the build up a galaxy's present-day dust and metal budget.

4 INTERPRETING LOCAL SCALING LAWS WITH DUST AND ELEMENT EVOLUTION MODELS (DEUS)

4.1 Binning the sample in an evolutionary sequence

For the purpose of understanding how the dust, HI gas and metal content evolves in galaxies, we have divided our local galaxy sample[9] into six separate bins according to equally sized ranges covered by galaxies in log $M_{\rm HI}/M_\star$. This subdivision results in unequal galaxy sample sizes in each bin. We decided to take this approach as the spread in various quantities (and thus the uncertainty on our median bin values) does not depend on the number of galaxies in each bin, but rather on the intrinsic scatter for galaxies at different stages of evolution. Table 3 lists the sample size, average stellar mass (log $M_\star$), specific HI gas mass ($\log(M_{\rm HI}/M_\star)$), specific dust mass ($\log(M_{\rm dust}/M_\star)$), dust depletion ($\log(M_{\rm dust}/M_{\rm metals}$(gas+dust)) and metallicity for these six galaxy bins. The bins range from galaxies with high $M_{\rm HI}/M_\star$ ratios and thus at an early stage of evolution (Bin 1), down to galaxies with low $M_{\rm HI}/M_\star$ ratios, which have converted most of their gas into stars during the course of their lifetime (Bin 6).

[9] We omitted HI-deficient HRS galaxies, since they have experienced recent removal of large fractions of their gas content, which makes it tenuous to reproduce their current HI gas, dust and metal content without detailed constraints on the timescale and the extent of their gas removal.

4.2 DEUS modelling framework

To interpret what drives the evolution of the stellar mass, metal mass, HI gas, and dust content as galaxies evolve, we have used a Bayesian modelling framework to find the set of parameters capable of reproducing the observed scaling relations in the local Universe. To compare dust, HI gas and metal scaling relations in the local Universe to model predictions, and infer what physical processes drive the observed trends and differences between galaxy populations, we have used a chemical evolution model that tracks the buildup and evolution of dust, gas and metals throughout the lifetime of a galaxy. More specifically, we employ Dust and Element evolUtion modelS (DEUS), which account for dust production by asymptotic giant branch (AGB) stars, supernova remnants (SNRs), grain growth in the interstellar medium, and dust destruction through astration and processing by supernova shocks. Our model implementation is largely founded upon chemical evolution models presented in the literature (e.g., Dwek 1998; Morgan & Edmunds 2003; Calura et al. 2008; Rowlands et al. 2014). An earlier version of DEUS was introduced by De Looze et al. (2017b). We extended DEUS to include dust destruction by supernova shocks and dust growth in the interstellar medium. We furthermore coupled DEUS to a Bayesian Markov Chain Monte Carlo (MCMC) algorithm to study the effects of varying dust production and destruction efficiencies and to infer the set of parameters that best describes the observed scaling relations in the local Universe. In contrast to previous models (e.g., Pagel 1997; Dwek 1998), we have accounted for the lifetime of stars, and the replenishment of the interstellar medium with metals, dust and any remaining gas after stellar death, rather than resorting to the instantaneous recycling approximation for which the enrichment is assumed to occur at stellar birth. Appendix D gives a detailed overview of the DEUS code, our assumed metal and dust yields, and prescriptions for grain growth and dust destruction by supernova shocks. For this current paper, we explore three different models:

- Model I assumes a closed-box and predicts the amount of dust and metals produced following the customised SFHs (see next paragraph) inferred for the six galaxy bins.
- Model II assumes a closed-box and adopts a fixed SFH shape for all six galaxy bins. More specifically, we have adopted a scaled version of the delayed SFH from De Vis et al. (2017b).
- Model III deviates from the closed-box assumption, and includes gas infall and outflows (see Appendix D3), and furthermore relies on the customised SFHs inferred for each of the six galaxy bins.

The amount of metals and dust produced in galaxies sensitively depends on its (recent) star formation activity. Given that the six local galaxy samples correspond to different galaxy evolutionary stages, we expect them to have gone through different levels of recent star formation activity. To account for variations in their past and recent star formation activity, we have determined a customized SFH for each of the six galaxy bins by relying on their average stellar mass, specific star formation rate, and SFR(10 Myr)-to-SFR(100 Myr) ratio. The latter SFRs were inferred from hybrid SFR calibrators: Hα+WISE 22 μm for SFR(10 Myr) and far-ultraviolet (FUV)+total-infrared (TIR) emission for

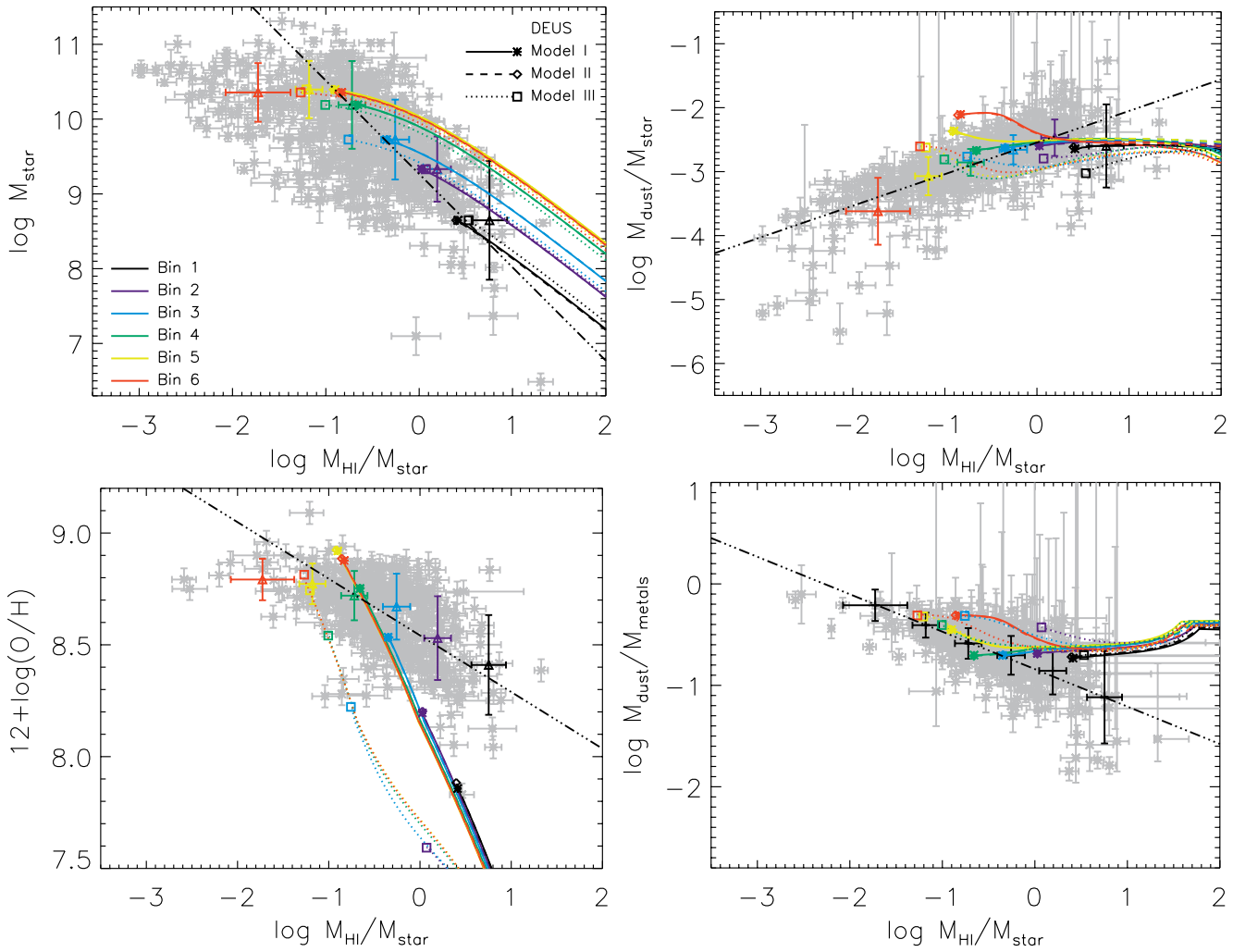

Figure 8. The scaling of the stellar mass ($M_\star$, top left), $M_{\rm dust}/M_\star$ (top right), oxygen abundance (bottom left) and $M_{\rm dust}/M_{\rm metals}$(gas+dust) (bottom right) with specific HI gas mass ($M_{\rm HI}/M_\star$) shown for our entire sample of nearby galaxies (grey symbols), with the best-fit trends overlaid as black dashed-triple dotted lines. The median values for each of the six galaxy bins are overlaid with coloured triangles and errors that correspond to the spread in each bin. The $M_{\rm HI}/M_\star$ ratio is highest for galaxies in Bin 1 (which are thought to correspond to the least evolved galaxies), while the more evolved galaxies with the lowest $M_{\rm HI}/M_\star$ ratios populate Bin 6. The evolutionary trends (over a period of 12 Gyr) that were inferred from the median parameters for Models I, II and III are overlaid as solid, dashed and dotted lines, respectively, and the final present-day model values are indicated with coloured asterisks, diamonds and squares, respectively. The colour coding of model trends and observed median properties range from black to red corresponding to Bins 1 through to 6 (see legend in the top left panel).

SFR(100 Myr). The customised SFHs are presented in Appendix C, where it is demonstrated that galaxies at an early stage of evolution have formed most stars during recent epochs, as opposed to more evolved galaxies which show a clear drop in their recent star formation activity.

Due to possible degeneracies between various dust production and destruction sources, we have coupled DEUS to a Bayesian MCMC method to effectively search a large parameter space and to constrain the relative importance of stellar dust production, grain growth and dust destruction by supernova shocks. Our Bayesian model has four free parameters: (1.) the initial gas mass, $M_{\rm gas,ini}$; (2.) the fraction of supernova dust that is able to survive the reverse shock, $f_{\rm survival}$; (3.) the grain growth parameter, ϵ (see Eq. D11); and (4.) the interstellar mass cleared by each single supernova event, $M_{\rm cl}$ (see Eq. D10), which is indicative of the dust destruction efficiency through supernova shocks. We leave the initial gas mass ($M_{\rm gas,ini}$) of the halo as a free parameter in DEUS to infer what gas mass is needed to reproduce the observed present-day specific HI gas masses ($M_{\rm HI}/M_\star$) and oxygen abundances. The initial gas mass is degenerate with the mass loading factors of infalling and outflowing gas; we therefore constrain the initial gas mass in our models at fixed in- and outflow rates (or no gaseous flows in the case of Models I and II). In a similar way, variations in the initial gas mass are hard to differentiate from merger events occurring throughout a galaxy's lifetime. To constrain the free parameters in DEUS, we have compared the present-day model output to five ob-

servational quantities: $\log M_\star$, $\log M_{\rm dust}/M_\star$, $\log M_{\rm HI}/M_\star$, $\log M_{\rm dust}/M_{\rm metals}$(gas+dust) and 12+log(O/H)[10].

As nothing much is known about the preferred values and their expected distribution, we have assumed flat priors to avoid biasing the model output results with $\log(M_{\rm gas,ini}/M_\odot)$ varying between 8.5 and 11, $f_{\rm survival}$ between 0.1 and 1.0, $\log(\epsilon)$ between 0.1 and 4.0, and $\log(M_{\rm cl}/M_\odot)$ between 0.1 and 5.0. This four-dimensional parameter space was sampled with an affine invariant ensemble sampler (Goodman & Weare 2010) as implemented in the `emcee` package for MCMC in `Python` (Foreman-Mackey et al. 2013). We have used a collection of 100 walkers to sample the entire parameter space, where the position of a walker is changed at each step to explore the parameter space and to look for a region with high likelihood. We assumed a likelihood function based on the commonly used χ^2 statistic: $\chi^2 = \Sigma_{i=1}^{N} \left(\frac{f_{\rm i}(obs) - f_{\rm i}(model)}{\sigma_{\rm i(obs)}} \right)^2$ with $f_{\rm i}$(obs) and $f_{\rm i}$(model) the observed and modelled values, respectively, and $\sigma_{\rm i(obs)}$ the observational uncertainty, for constraint i, which is equivalent to a Gaussian likelihood. The positions of the 100 walkers are recorded at each time step after a warm-up phase of $N_{\rm burn}$=500 steps, and the simulations are run for a total of $N_{\rm steps}$=1,500 steps. The final 1,000 time steps are used to construct the posterior probability density functions (PDFs). We furthermore verified that these steps are sufficient for each of the model parameters to converge, which requires the effective sample size $N_{\rm eff}$ ($=N_{\rm chain}/\tau_{\rm int}$ with $N_{\rm chain}$ the length of the chain and $\tau_{\rm int}$ the integrated autocorrelation time of the chain) to be higher than 10 for all parameters. As an additional check, we verified that the acceptance fraction of walkers ranges between 0.2 and 0.5.

4.3 Modelling results

The median parameter values inferred from the 1D posterior PDFs were tabulated in Table 4 for the three different models. Figures G1 through to G18 present the 1D and 2D posterior PDFs for the six galaxy bins and Models I, II, and III, respectively. The evolutionary tracks – as determined from those median parameter values and spanning a time period of 12 Gyr – have furthermore been overlaid on the individual panels of Figure 8.

The stellar mass and metal abundance gradually increases for all models as galaxies evolve. For Model III (with gaseous in/outflows), the metallicity increase is less steep compared to Models I and II due to metal-enriched outflows. Due to this slow metal enrichment, Model III is able to reproduce the low specific gas masses observed for more evolved galaxies in Bins 5 and 6. The dust-to-metal ratio (i.e., the amount of metals depleted onto dust grains) starts off at a plateau around 40% in all models, indicative of dust being produced mainly by stars, and only a minor contribution from grain growth, in the early stages of galaxy evolution. After a few 100 Myr, the metal abundance and dust mass has increased sufficiently for grain growth to kick in. However, the dust-to-metal ratio in our models first drops due to grain destruction (i.e., supernova shocks and astration) dominating over grain growth processes. For more evolved galaxies (Bins 5 and 6), the dust-to-metal ratio continues to increase due to grain growth becoming more dominant than these dust destruction mechanisms. Similar results have been inferred from galaxy simulations (e.g., Aoyama et al. 2017). The dust-to-stellar mass ratio shows a similar trend with a nearly flat ratio at the start due to dust forming as stars evolve, progressing to a gradual increase (if grain growth starts to become important) or decrease (if dust destruction processes dominate).

In most cases, the present-day model values (indicated with asterisks, diamonds and squares for Models I, II and III, respectively, in Fig. 8) are capable of reproducing the observed ratios in each bin within the error bars (reflecting the dispersion observed within each $M_{\rm HI}/M_\star$ bin) which makes us confident that the models are adequate to reproduce the dust, metal and HI gas scaling relations observed for the local Universe. There are however two notable exceptions. For evolved galaxy populations (Bins 5 and 6), Models I and II are not capable of reproducing their low observed specific HI gas masses ($\log M_{\rm HI}/M_\star \lesssim -1.0$). We believe this model discrepancy is driven by the closed-box assumption in Models I and II, as Model III is capable of reproducing the $M_{\rm HI}/M_\star$ ratios and metal abundances for these more evolved galaxies better. Due to their decrease in recent ($\lesssim$100 Myr) star formation activity, these galaxies are likely to have experienced some type of quenching during the last stages of their evolution. The assumption of a constant star formation rate on timescales >100 Myr, with a sudden drop in their recent star formation activity might therefore not be fully representative if quenching timescales are longer. However, the rapid star formation quenching inferred for several HRS galaxies (Ciesla et al. 2016) suggests that at least some galaxies experience a sudden drop in their SF activity on 100 Myr timescales. A discrepancy is also observed for galaxies at an early stage of evolution (Bins 1 and 2), for which both closed-box models and models with gaseous flows underestimate the observed metal abundances (see bottom panels in Figure 8). We speculate that these modelled low metal abundances might be compensated for by locking fewer metals into dust grains – either through less efficient grain growth processes or more efficient grain destruction – which will also bring the modelled dust-to-metal ratios closer to the observed values. Other than possible model discrepancies, we should note that the oxygen abundances are missing for several galaxies at the low end of the metallicity range, which will inevitably bias our average bin measurements upwards for these less evolved galaxies as the full dynamic range of metallicity values has not been covered.

4.4 Dust production and destruction efficiencies

In the rest of the paper, we focus our discussion on the dominant dust production and destruction mechanisms for the subsample of galaxies in Bins 3 and 4 with $-1.0 \lesssim \log M_{\rm HI}/M_\star \lesssim 0$, which constitute the majority (266/423 or 63%) of the local galaxy population. Stochastic effects will not hamper the median values inferred for the galaxies in Bins 3 and 4 as is the case for poorly sampled galaxy bins at the low and high $M_{\rm HI}/M_\star$ end. The stellar mass

[10] We have compared the median observed values to the model predictions at the end of our simulations at a galaxy age of 12 Gyr (assuming that these galaxies started forming stars 12 Gyr ago).

range (10^9-10^{11} $M_\odot$) covered by Bins 3 and 4 furthermore corresponds to galaxies in which an equilibrium is reached between gaseous infall, outflow and star formation (Bothwell et al. 2013). Such an equilibrium implies that the choice of specific gas infall/outflow rates and mass loading factors for these galaxies will have less of an impact on the output model parameters. The galaxies outside this stellar mass range instead show a large degree of scatter, and will be more sensitive to the effect of gas infall or outflows during recent times. We prefer to focus on these galaxies, for which the effect of gas infall or outflows during recent times has been less important, having sustained star formation over several Gyr (see Figure C1). The closed-box Models I and II result in adequate fits (as quantified by the $\chi^2_{\rm red}$ statistic, see Table 4) for these galaxies at an intermediate stage of evolution. We note that the conclusions for Models III (including gaseous in/outflows) generally remain unmodified, but these models typically give rise to larger model parameter uncertainties and less well constrained fits (see Table 4) due to the increased level of model complexity. Specifically, the oxygen abundance is severely underestimated due to the recent infall of pristine gas for galaxy Bins 1 through to 4, which results in higher $\chi^2_{\rm red}$ values for Model III than for Models I and II. The specific prescription adopted here to model gaseous flows might not be appropriate for the entire range of galaxies in our sample, and there result in worse model fits to the data. The assumed infall and outflow rates in Model III fit the data well for galaxies in Bins 5 and 6, resulting in better fits than for Models I and II.

4.4.1 Initial gas mass

The initial gas masses are well determined showing peaked 1D posterior PDFs with values that gradually increase with the evolutionary stage of galaxies (see Table 4) in line with the expectation that galaxies at an advanced stage of evolution are more massive, and thus require a larger initial mass to convert gas into stars than less evolved galaxies. It should be noted that part of this trend might be driven by merger events leading to increased gas masses at specific times throughout a galaxy lifetime rather than increased initial gas masses. Since these merger events have not been considered here, the models may have converged to large initial gas masses to reproduce present-day scaling laws for more evolved galaxies. The initial gas masses might be one of the most important parameters in DEUS as they directly influence the present-day model stellar masses and metal abundances, and play an important role in setting the posterior PDFs obtained for the other parameters. In future work, we intend to explore the importance of the initial gas mass parameter (and possible degeneracies with gaseous in- and outflows and merger events) in more detail.

4.4.2 Net supernova dust production rates

Models I and II suggest that a significant fraction (37 to 89%) of freshly condensed supernova dust is able to survive the reverse shock. Dust evolution models that include the effects of sputtering and/or shattering on supernova dust grains due to the passage of a reverse shock estimate dust survival rates ranging from 1 to 100% (e.g., Bianchi & Schneider 2007; Nozawa et al. 2007; Nath et al. 2008; Silvia et al. 2010; Sarangi & Cherchneff 2015; Biscaro & Cherchneff 2016; Bocchio et al. 2016; Micelotta et al. 2016; Kirchschlager et al. 2019). An easy comparison between these various models is hampered by the different assumptions made to describe the ambient densities, the density contrast between dust clumps and the surrounding medium, the grain size distribution and the composition of supernova dust species. In addition, our inferred dust survival rate will account for the fact that some supernova remnants will not experience a reverse shock (e.g., the Crab Nebula) due to the low density of the surrounding medium, and should thus be considered as an "effective" dust survival rate as it is convoluted with the probability that a reverse shock will be generated through the interaction with a dense circum- or interstellar medium, and that dust might be able to reform after the shock passage (e.g., Matsuura et al. 2019). Current observational studies tend to be biased towards interacting supernova remnants or pulsar wind nebulae which provide a heating mechanism through shock interaction or through the presence of a pulsar, respectively. It is therefore hard to estimate the fraction of SNRs that will experience a reverse shock, and at what average velocity the reverse shock will interact with the ejecta. Moreover, a non-negligible fraction of core-collapse supernovae occur "late" (i.e., 50-200 Myrs after birth) due to binary interactions (Zapartas et al. 2017). On such long timescales, the birth clouds of these massive stars will have dissolved, and it will become less likely that a reverse shock is generated.

Our high dust survival fractions are in excellent agreement with recent observational constraints. Elevated dust-to-gas ratios in the shocked ejecta clumps of the Galactic supernova remnant Cassiopeia A suggest that a significant fraction of supernova dust is capable of surviving a reverse shock (Priestley et al. 2019). Several studies (e.g., Temim & Dwek 2013; Gall et al. 2014; Wesson et al. 2015; Bevan & Barlow 2016; Priestley et al. 2020) have also argued for rather large supernova grain sizes ($\gtrsim$0.1 μm), which lends support to the idea that significant fractions of supernova dust are able to survive a reverse shock (with large grains being more resilient to sputtering, e.g., Silvia et al. 2010).

4.4.3 Grain growth timescales

The grain growth parameter has been parameterised through ϵ following Mattsson et al. (2012) (see Eq. D11 and Appendix D2 for an outline of its derivation). At a fixed gas mass, dust-to-gas ratio, metal fraction and star formation rate, the grain growth parameter ϵ is inversely proportional to the grain growth timescale, and can be considered to approximate the efficiency of grain growth processes. More specifically, large values of ϵ correspond to efficient grain growth and thus short grain growth timescales $\tau_{\rm grow}$, while small ϵ values are indicative of long $\tau_{\rm grow}$[11].

The 1D posterior PDFs for Models I and II, and Bins 3 and 4, have $\log\epsilon$ peaking around 2.0, with a wide tail of high-likelihood models extending to lower $\log\epsilon$ values and

[11] Values of ϵ of 10-100 typically correspond to $\tau_{\rm grow} > 100$ Myr, while $\epsilon \gtrsim 1000$ is needed to reach down to $\tau_{\rm grow}$ of 10 Myr and lower (depending on the assumed SFR, gas, dust and metal mass).

a sudden drop in likelihood beyond values of log $\epsilon \gtrsim$2.0. The 1D posterior PDFs for Model III peaks at higher values (see Figures G9 and G12) than for closed-box models, which is not surprising given that dust and metals will be expelled from the galaxy, and thus an additional source of dust production is required in Model III. A narrow range of models with ϵ values higher than this peak seems also capable of explaining our observed scaling relations, but only if such high grain growth efficiencies are exactly compensated for by high dust destruction efficiencies (e.g., the rightmost 2D contour plot on the bottom row of Figures G10, G11 and G12). With grain growth locking refractory elements into grains, and dust destruction releasing these same elements back into the gas phase, our observational constraints are not capable of distinguishing between both mechanisms. The model prescriptions to describe grain growth and dust destruction efficiencies furthermore depend directly (or indirectly in case of the supernova rate) on the current SFR, which causes this degeneracy between grain growth and dust destruction efficiencies, as long as both processes cancel each other out. To adapt those recipes, we require improved understanding of the grain growth and destruction processes in the interstellar medium. The 2D contour plots suggest that the models are also hampered by degeneracies between the supernova dust survival rate ($f_{\rm survival}$), the grain growth parameter (ϵ) and the dust destruction efficiency ($M_{\rm cl}$) in some parts of the 4D parameter space, which results in wide 1D posterior PDFs.

Our median values of log ϵ=$1.5^{+1.1}_{-0.9}$ – equivalent to present-day growth timescales $\tau_{\rm growth}$ of $\gtrsim$100 Myr, with a median of 400 Myr – are consistent with the range of values ($\epsilon \in$[10,457]) inferred by Mattsson & Andersen (2012) based on the resolved dust-to-metal gradients observed in a sample of 15 SINGS galaxies, and the accretion timescales ($\tau_{\rm grow}$=20-200 Myr, or ϵ=500) that were found adequate to reproduce the dust masses in a sample of high-redshift (z>1) submillimetre galaxies (Rowlands et al. 2014). In general, however, our grain growth efficiencies are significantly lower than many other studies. In Asano et al. (2013), Zhukovska (2014), Mancini et al. (2015) and Schneider et al. (2016), fast grain growth timescales of 0.2-2 Myr have been assumed which causes grain growth to dominate dust production as soon as a critical metallicity threshold has been reached. Feldmann (2015) required similarly short accretion timescales (5 Myr) to reproduce the dust and metal masses in low-metallicity dwarf galaxies. Also the dust, metal and gas scaling relations for a sample of nearby galaxies were found to be best reproduced by chemical evolution models with ϵ values of 2500-4000 (De Vis et al. 2017b)[12]. All of these studies suggest that grain growth dominates dust production for different galaxy populations across a wide range of different redshifts (see also Section 4.5).

Even though recent laboratory studies suggest that SiO_x and more complex silicate-type grains can form without an activation energy barrier under typical molecular cloud ($T_{\rm dust}$=10-12 K) conditions (Krasnokutski et al. 2014; Rouillé et al. 2015; Henning et al. 2018), it might be hard for the majority of dust grains in the low-redshift Universe to have formed through accretion of elements onto pre-existing grain seeds given the low accretion rates and the Coulomb barrier that needs to be overcome in diffuse gas clouds, and the efficient formation of ice mantles which prevents efficient grain growth in dense molecular clouds (Barlow 1978; Ferrara et al. 2016; Ceccarelli et al. 2018). Zhukovska et al. (2016) modelled the formation of silicate grains through the accretion of elements in diffuse gas clouds (with gas densities $n_{\rm H}$ between 5 and 50 cm^{-3}) on average timescales of 350 Myr, while Zhukovska et al. (2018) suggest that iron grains can grow efficiently in the cold neutral medium on timescales $\lesssim$10 Myr. Due to the absence of laboratory measurements of diffusion and desorption energies, the latter works assumed that elements sticking to grain surfaces, will have sufficient time to reach a strong active bonding site where these refractory elements can be chemisorbed. Given that the exposure to strong UV radiation in diffuse gas clouds will make these elements prone to photo-desorption processes, and various elements on the grain surface (with differing diffusion energies) might be competing for the same dangling bonds, we argue that a detailed set of laboratory studies, combined with detailed chemical modelling, is needed to verify what kind of grain species can form and what timescales are involved in their formation. We speculate that our longer grain growth timescales (and longer dust lifetimes, see Section 4.4.4) might reduce the tension with grain surface chemical models which have so far been incapable of proposing a viable chemical route for grain growth.

4.4.4 *Dust destruction efficiencies*

The dust destruction efficiency has been parameterised through the interstellar mass that is cleared per single supernova event ($M_{\rm cl}$). In reality, it is unlikely that a single value will apply to all supernova events as $M_{\rm cl}$ will depend on the ambient density, on the 3D structure of the ambient medium and on the supernova explosion energy. With several models assuming a single value for $M_{\rm cl}$, we pursue to infer what average values are adequate to reproduce the observed scaling laws in the local Universe. Similar to the grain growth parameter, the 1D posterior PDF for $M_{\rm cl}$ shows a sharp drop in likelihood beyond $M_{\rm cl} \gtrsim 10^{2.4}$ M$_\odot$. Higher values are only allowed in case the dust destruction efficiency is perfectly balanced by the same level of dust production through grain growth. The models are incapable of distinguishing between values of $M_{\rm cl}$ below this threshold due to degeneracies with the level of supernova dust production and the grain growth parameter.

The peaks in the 1D posterior PDFs occur at low $M_{\rm cl}$ values, resulting in median values of $M_{\rm cl}=10^{1.4-1.6}$ for galaxies in Bins 3 and 4, and correspond to long dust lifetimes of 1 to 2 Gyr. The upper limits in our models for the mass cleared per supernova event ($\lesssim$400 M$_\odot$) are consistent with current dust destruction timescales $\gtrsim$200 Myr. Our preferred model dust lifetimes of a few Gyr are consistent with the longer dust destruction timescales (2-3 Gyr) inferred for silicate grains by Slavin et al. (2015) by means of supernova remnant models with evolving shock waves. Long dust lifetimes (on the order of a few Gyr) for silicate grains were also suggested by Jones & Nuth (2011) after accounting for the 3D distribution of interstellar material, while carbonaceous

[12] The ϵ values (5000-8000) from De Vis et al. (2017b) have been corrected to account for their assumed cold gas fraction ($f_{\rm c}$=0.5) to allow for a direct comparison with our values.

grains are assumed to be processed on short timescales. Our conclusion applies to the ensemble of interstellar grains, and is in agreement with these longer silicate lifetimes. In future work, we hope to make the distinction in our models between the formation and destruction of various grain species such as carbonaceous and silicate dust grains. It is worth noting that our inferred dust destruction timescales are factors of a few longer than the average values reported by other works (e.g., 400-600 Myr, Jones et al. 1994, 1996; <90 Myr, Rowlands et al. 2014; 20-70 Myr for dust in the Magellanic clouds Temim et al. 2015; Lakićević et al. 2015; 350 Myr, Zhukovska et al. 2016, 2018; Hu et al. 2019).

4.5 Dominant dust production sources

Our thorough search of the four-dimensional parameter space, adapted to cover a wide range of different Dust and Element evolUtion modelS, has revealed that local galaxy scaling relations (with the exception of galaxies with low and high specific gas masses) can be reproduced adequately by models with long dust survival rates (on the order of 1-2 Gyr), low grain growth efficiencies (ϵ ~30-40) and a predominant contribution of stellar dust production sources to account for the present-day galaxy dust budgets. More specifically, we estimate that most of the dust (>90 %) is produced through stellar sources over a galaxy's lifetime, with a minor contribution from grain growth (<10 %, see Fig. 9). The contribution of grain growth increases with time for all models, with 50 to 80% of present-day dust masses resulting from stellar dust, while 20 to 50% of the dust is suggested to grow through the accretion in interstellar clouds. Models with in- and outflows (Model III) have an increased contribution from grain growth, resulting in more or less equal contributions from grain growth and stellar sources to the dust production over a galaxy lifetime. Given that a fraction of the dust is lost in galactic outflows (i.e., scaled with the dust-to-gas ratio of the galaxy at that point in time), we require more dust production through grain growth to reproduce the observed dust-to-stellar and dust-to-metal mass ratios with Models III. We furthermore note a trend of high relative fractions of stardust for less evolved galaxies (Bins 1 and 2), which is not surprising given the low metal abundances (and hence low grain growth efficiencies) for these galaxies.

We speculate that through performing a rigorous search of the four-dimensional parameter space, our results provide an alternative for the chemical evolution models with extremely low supernova dust production efficiencies and short grain growth timescales ($\lesssim$a few Myr), which have been invoked to explain the dust, metal and gas scaling laws of local galaxies (e.g. Zhukovska 2014; Feldmann 2015; De Vis et al. 2017b). Regardless of our model assumptions on the SFH and gaseous flows, the local dust, HI gas and metal scaling relations are reproduced well with models that assume long dust lifetimes (1-2 Gyr), favourable supernova dust injection rates ($f_{\rm survival}$ of 37-89%) and low grain growth efficiencies (ϵ of 30-40). These long grain growth timescales could reduce the tension between the high grain growth efficiencies (required to reproduce the large dust masses observed in low- to high-redshift galaxies) and grain surface chemical models, which currently fail to account for efficient grain growth processes in the interstellar medium (e.g., Barlow 1978; Ferrara et al. 2016; Ceccarelli et al. 2018; Jones & Ysard 2019).

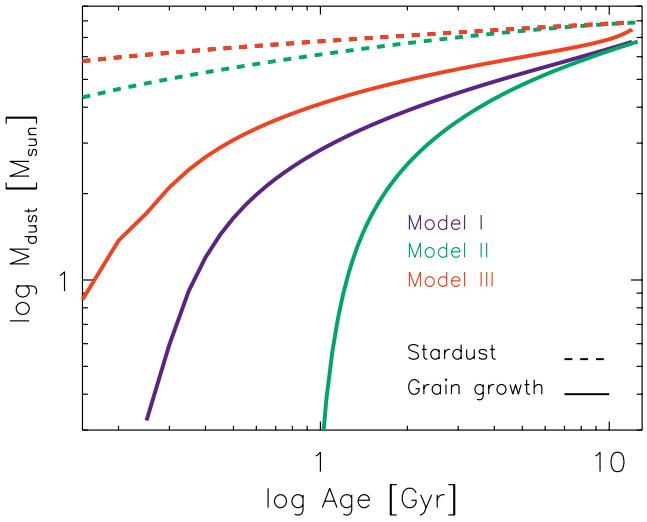

Figure 9. The amount of dust produced through stellar sources (AGB+SNe, dashed curves) and through interstellar grain growth (solid curves) as a function of galaxy age, as inferred from the median model parameter values for Bin 4. The stardust tracks for Model I and Model III overlap due to the same assumed SFH shape for both models.

4.6 Modelling caveats

We resorted to making some assumptions in DEUS to avoid introducing various model degeneracies. We briefly discuss the implications of these assumptions.

- **Star formation history:** we have assumed a customised SFH for each galaxy bin (i.e., Models I). To test the importance of this model assumption, we also ran models with a delayed star formation history (i.e., Models II). A quick comparison between the inferred model parameters shows that the dependence on the specific shape of the SFH is minimal based on the close resemblance between the Model I and II output parameters (see Table 4). We argue that the minor importance of the specific SFH shape results from the long dust lifetimes, which imply that the current dust reservoir has been built up during the last 1-2 Gyr, and that variations in the SFH shape on these timescales are less relevant as long as the final produced dust mass remains the same. We should also note that the simplicity of the SFH shapes, and other model assumptions may affect the dependence of the results on the SFH.
- **Closed-box vs gaseous flows:** even though the importance of gaseous flows is now well established in the field, the precise nature of these gas-regulated "bathtub" galaxies still requires further characterisation. In Model III, we have assumed that the infalling gas is pristine (i.e., the gas is not enriched with metals or dust), while the outflowing gas has the same gas-phase metallicity and dust-to-gas ratio as the galaxy at the time of the outflow. This assumption will vary depending on the outflow mechanism and the location of the onset of these gaseous outflows. The outflow rate is often assumed to scale with the SFR, but a time-dependent outflow

model with strong outflows at early times has been shown adequate to reproduce the observed gas and stellar metallicities in galaxies (Lian et al. 2018a). Similar time- or stellar mass-dependent outflows are also consistent with galaxy simulations (e.g., Muratov et al. 2015; Hayward & Hopkins 2017). We suggest that these strong outflows at early times (as implemented in our Model III), result in a slow build-up of a galaxy's metal content, which reduces the efficiency of grain growth processes at early times. Low outflow rates at the present epoch also reduce the need for short grain growth timescales to account for the observed dust masses in galaxies. But, as remarked upon before, different assumptions on the time-dependence of these outflows will affect dust production and destruction efficiencies. To limit these biases, we have assumed closed-boxes for Models I and II to model galaxies which have reached an equilibrium between gaseous infall, outflow and star formation.

- **One-zone models:** outflow rates are thought to vary with radial distance from the galaxy centre (e.g., Lian et al. 2018b; Belfiore et al. 2019; Vílchez et al. 2019), which would require resolved galaxy models to take this into consideration. Other than these spatial variations in mass loading factors, the 3D structure and filling factors of various ISM phases that together constitute an entire galaxy, will vary depending on the evolutionary stage and the specific type of galaxies under consideration. Dwarf galaxies in the nearby Universe provide an excellent example of how their low metal and dust content, high degree of porosity and radiation field hardness severely affects their ISM build-up with a highly-ionised, diffuse medium that dominates the ISM volume, and only minor contributions from compact phases (e.g. Lebouteiller et al. 2012; Cormier et al. 2015; Madden & Cormier 2019; Cormier et al. 2019). The detection of highly ionised nebular lines (e.g., Smit et al. 2014; Inoue et al. 2016; Carniani et al. 2017; Laporte et al. 2017; Hashimoto et al. 2018) suggests that high-redshift galaxies might have an ISM build-up similar to low-metallicity dwarfs in the nearby Universe, and supports the need for spatially resolved chemical evolution modelling to account for radially-dependent gas in/outflows and filling factors of different ISM phases (e.g. Peters et al. 2017). In the future, we plan to expand DEUS to include a realistic 3D ISM structure to model how the density and temperature distributions of the total ensemble of gas clouds in a galaxy varies with time.
- **Metal and dust yields:** we had to assume a set of AGB and supernova metal and dust yields, and apply specific prescriptions to describe the efficiency of grain growth and dust destruction processes. We endeavoured to select yields and recipes that correspond to the current state-of-the-art, but these prescriptions remain limited by our current knowledge on how grains are destroyed and whether or not grains can grow either in diffuse or dense clouds of the interstellar medium. If the true yields were to differ significantly from our model assumptions and/or show variations with metallicity (e.g., Valiante et al. 2009; Boyer et al. 2019; Dell'Agli et al. 2019), this could impact our inferred model parameters. In De Vis in prep., the choice of metal yields is shown to mostly impact the metallicities of galaxies with high specific gas masses.
- **Time dependence:** we have not accounted for variations in the dust destruction efficiency and grain growth parameter in time, which could be induced if strong variations in the grain size distribution occur throughout a galaxy's lifetime, as the efficiency of grain destruction and grain growth is strongly grain size-dependent (e.g. Hirashita 2015).
- **Initial mass function (IMF):** We have furthermore assumed a fixed Chabrier (2003) IMF. The shape of the IMF has been suggested to vary in different environments (e.g. Oldham & Auger 2018), and deviations from this standard IMF will affect the dust and metal yields, and supernova rates in DEUS.

In future work, we aim to explore the effects of varying the IMF and applying different sets of metal and dust stellar yields, to accommodate physically-motivated recipes to describe grain growth and dust destruction processes, and to allow for spatial variations in the efficiencies of these processes with local ISM conditions.

5 CONCLUSIONS

We analysed local dust, HI gas and metal scaling relations for a diverse sample of 423 nearby galaxies to infer that:

- the specific dust and HI gas masses are tightly linked to a galaxy's specific star formation rate (sSFR), which suggests that the interstellar mass (either traced through HI gas or dust) plays an important role in setting a galaxy's SFR (through the Kennicutt-Schmidt law).
- the HI gas scaling laws show the largest degree of dispersion, which suggests that variations in $M_{\rm dust}/M_\star$, $M_{\rm dust}/M_{\rm metals}$(gas+dust) and $M_{\rm dust}/M_{\rm HI}$ ratios are not necessarily influenced by dust production and destruction mechanisms but rather driven by the current HI gas reservoirs of galaxies.
- the strong correlations between $M_{\rm HI}/M_\star$, and $M_{\rm dust}/M_\star$, $M_{\rm dust}/M_{\rm metals}$(gas+dust) and $M_{\rm dust}/M_{\rm HI}$ reinforce the idea that the specific HI gas mass ($M_{\rm HI}/M_\star$) plays an important role in setting the dust and metal content of galaxies.
- the $M_{\rm dust}/M_{\rm metals}$(gas+dust) ratio in galaxies is nearly constant ($10^{-0.66\pm0.24}$) across our sample of galaxies for $M_\star \geq 10^9\,M_\odot$. Weak (but significant) trends with $M_\star$, sSFR and $M_{\rm HI}/M_\star$ support a scenario of increasing $M_{\rm dust}/M_{\rm metals}$(gas+dust) ratios as a galaxy evolves.
- the large spread (0.34 dex) in the $M_{\rm dust}/M_{\rm HI}$ ratio at a given metallicity should urge caution: total gas masses inferred from dust mass measurements will be uncertain by a factor of $\gtrsim 2$ due to variance – driven by intrinsic galaxy variations, the unknown extent of HI reservoirs and/or uncertain oxygen abundances – at a fixed metallicity.

To model the evolution of the dust and metal budgets in nearby galaxies, we have split up the local sample of galaxies in six "galaxy evolutionary" bins according to their specific HI gas masses. The observed $M_\star$, metallicity, $M_{\rm dust}/M_\star$, $M_{\rm HI}/M_\star$ and $M_{\rm dust}/M_{\rm metals}$(gas+dust) ratios at these six galaxy evolutionary stages were interpreted with a set of Dust and Element evolUtion modelS (DEUS) – including dust production by asymptotic giant branch stars, supernova remnants, grain growth in the interstellar medium, and dust destruction through astration and processing by supernova shocks. DEUS was coupled to an MCMC method

Table 3. The bin number (1st column), $\log(M_{\rm HI}/M_\star)$ range (2nd column), sample size (3rd column) and median properties (columns 4-9) inferred for each of the six galaxy bins. These galaxy bins were selected to include less evolved galaxies (Bin 1) while gradually moving to galaxies with the most advanced stages of evolution (Bin 6).

Bin	Range	$N_{\rm gal}$	$\log(M_\star/{\rm M}_\odot)$	$\log({\rm sSFR/yr}^{-1})$	$\log(M_{\rm HI}/M_\star)$	$\log(M_{\rm dust}/M_\star)$	$\log(M_{\rm dust}/M_{\rm metals})$	Metallicity
1	[0.5,-]	17	8.65±0.79	-9.36±0.28	0.75±0.19	-2.60±0.65	-1.12±0.46	8.41±0.22
2	[0,0.5[	81	9.33±0.44	-9.62±0.29	0.19±0.15	-2.47±0.29	-0.86±0.23	8.53±0.19
3	[-0.5,0[	134	9.73±0.53	-9.98±0.35	-0.26±0.15	-2.66±0.23	-0.70±0.19	8.67±0.15
4	[-1.0,-0.5[	132	10.19±0.59	-10.21±0.34	-0.72±0.14	-2.86±0.21	-0.59±0.15	8.72±0.11
5	[-1.5,-1.0[	46	10.40±0.38	-10.57±0.63	-1.18±0.14	-3.07±0.30	-0.41±0.12	8.77±0.10
6	[-,-1.5[	13	10.36±0.39	-11.30±0.91	-1.72±0.35	-3.62±0.52	-0.21±0.15	8.79±0.09

Table 4. The median values for the four DEUS parameters as inferred from three different models for each of the six galaxy bins. Models I and II correspond to closed-box models with optimised non-parametric SFHs and with a delayed SFH (with fixed shape), respectively (see Appendix C). Model III includes gaseous in- and outflows (see Appendix D3) and the specific set of non-parametric SFHs. The upper and lower limits on the model parameters have been inferred from the posterior PDFs as the 16th and 84th percentiles. In addition to these output model parameters, we calculated the reduced χ^2_{red} statistic by comparing the observed values with the model predictions for the median parameters. We also inferred the fraction of dust produced through stellar sources ($f_{\rm stardust}$) and through accretion processes in the ISM ($f_{\rm grain\ growth}$) throughout the galaxy lifetime, and at the current age of the galaxy (values between square brackets).

Bin	Bin 1	Bin 2	Bin 3	Bin 4	Bin 5	Bin 6
Model parameters	Model I. "Closed-box" model with specific non-parametric SFHs					
$\log(M_{\rm gas,ini}/{\rm M}_\odot)$	$9.33^{+0.11}_{-0.11}$	$9.77^{+0.08}_{-0.07}$	$9.99^{+0.05}_{-0.04}$	$10.36^{+0.03}_{-0.03}$	$10.51^{+0.02}_{-0.02}$	$10.48^{+0.03}_{-0.03}$
$f_{\rm survival}$ [%]	51^{+33}_{-21}	60^{+26}_{-27}	63^{+24}_{-25}	65^{+22}_{-27}	69^{+23}_{-35}	61^{+27}_{-34}
$\log\epsilon$	$2.0^{+1.2}_{-1.3}$	$1.8^{+1.2}_{-1.1}$	$1.6^{+1.0}_{-1.0}$	$1.5^{+0.8}_{-0.9}$	$2.2^{+1.0}_{-0.7}$	$3.0^{+0.7}_{-0.8}$
$\log(M_{\rm cl}/{\rm M}_\odot)$	$2.2^{+1.2}_{-1.4}$	$1.6^{+1.1}_{-1.0}$	$1.6^{+1.0}_{-1.0}$	$1.4^{+1.0}_{-0.9}$	$1.5^{+1.7}_{-1.0}$	$1.8^{+1.3}_{-1.0}$
$\chi^2_{\rm red}$	9.6	5.0	1.2	1.6	11.0	15.5
$f_{\rm stardust}$ [%]	99 [91]	98 [84]	96 [69]	93 [52]	55 [8]	30 [16]
$f_{\rm grain\ growth}$ [%]	1 [9]	2 [16]	4 [31]	7 [48]	45 [92]	70 [84]
Model parameters	Model II. "Closed-box" model with delayed SFHs					
$\log(M_{\rm gas,ini}/{\rm M}_\odot)$	$9.33^{+0.11}_{-0.10}$	$9.77^{+0.08}_{-0.07}$	$9.99^{+0.05}_{-0.05}$	$10.35^{+0.03}_{-0.03}$	$10.50^{+0.02}_{-0.02}$	$10.48^{+0.03}_{-0.03}$
$f_{\rm survival}$ [%]	50^{+32}_{-27}	59^{+27}_{-26}	63^{+24}_{-26}	68^{+21}_{-27}	66^{+24}_{-35}	60^{+28}_{-33}
$\log\epsilon$	$2.0^{+1.3}_{-1.3}$	$1.7^{+1.0}_{-1.1}$	$1.5^{+1.0}_{-0.9}$	$1.5^{+0.8}_{-0.9}$	$2.1^{+1.0}_{-0.7}$	$3.0^{+0.7}_{-0.7}$
$\log(M_{\rm cl}/{\rm M}_\odot)$	$2.0^{+1.3}_{-1.3}$	$1.7^{+1.0}_{-1.1}$	$1.5^{+1.0}_{-0.9}$	$1.4^{+0.9}_{-0.9}$	$1.5^{+1.6}_{-1.0}$	$1.8^{+1.4}_{-1.1}$
$\chi^2_{\rm red}$	9.4	4.9	1.2	1.6	10.9	15.3
$f_{\rm stardust}$ [%]	99 [96]	98 [91]	96 [81]	93 [66]	57 [13]	30 [11]
$f_{\rm grain\ growth}$ [%]	1 [4]	2 [9]	4 [19]	7 [34]	43 [87]	70 [89]
Model parameters	Model III. Model with gas in/outflows and specific non-parametric SFHs					
$\log(M_{\rm gas,ini}/{\rm M}_\odot)$	$9.43^{+0.13}_{-0.12}$	$9.79^{+0.10}_{-0.10}$	$9.84^{+0.04}_{-0.02}$	$10.27^{+0.01}_{-0.01}$	$10.45^{+0.01}_{-0.01}$	$10.41^{+0.01}_{-0.01}$
$f_{\rm survival}$ [%]	51^{+32}_{-31}	66^{+24}_{-37}	57^{+31}_{-38}	66^{+24}_{-38}	56^{+31}_{-36}	34^{+32}_{-36}
$\log\epsilon$	$2.8^{+1.8}_{-1.9}$	$4.0^{+1.3}_{-2.5}$	$3.7^{+0.7}_{-0.8}$	$2.7^{+1.0}_{-1.0}$	$2.9^{+0.8}_{-0.6}$	$3.2^{+0.6}_{-0.6}$
$\log(M_{\rm cl}/{\rm M}_\odot)$	$2.1^{+1.5}_{-1.4}$	$1.9^{+1.3}_{-1.2}$	$1.8^{+1.4}_{-1.2}$	$1.6^{+1.5}_{-1.0}$	$1.7^{+1.4}_{-1.1}$	$1.7^{+1.2}_{-1.1}$
$\chi^2_{\rm red}$	26.4	30.3	23.9	7.0	0.8	5.8
$f_{\rm stardust}$ [%]	99 [95]	71 [33]	54 [12]	73 [10]	57 [8]	49 [17]
$f_{\rm grain\ growth}$ [%]	1 [5]	29 [67]	46 [88]	27 [90]	43 [92]	51 [83]

to effectively search a large parameter space and to constrain the relative importance of stellar dust production, grain growth and dust destruction by supernova shocks. We obtained an extensive set of models by varying the initial gas mass ($M_{\rm gas,ini}$), the survival rate of supernova dust after passage of the reverse shock ($f_{\rm survival}$), the grain growth parameter (ϵ) and the interstellar mass cleared per supernova event ($M_{\rm cl}$, which determines the efficiency of dust destruction through supernova shocks). Based on a rigorous search of this four-dimensional parameter space, we conclude that:

- the average scaling laws for galaxies with $-1.0 \lesssim \log M_{\rm HI}/M_\star \lesssim 0$ (which are considered to have reached an equilibrium between gas infall, outflow and star formation) can be reproduced using closed-box models with a high fraction (37-89%) of supernova dust that is able to survive a reverse shock, low grain growth efficiencies (ϵ=30-40), and long dust lifetimes (1-2 Gyr).
- the contribution from stardust (>90 %) outweighs the fraction of dust grown through accretion in the ISM (<10 %) over the entire lifetime of these galaxies, while present-day dust budgets have similar contributions from stellar sources (50-80%) and ISM dust growth (20-50%).
- the specific shape of the SFH does not strongly influence the model outcome due to these long dust lifetimes.

We demonstrate in this paper that local galaxy scaling relations can be accounted for by efficient supernova dust production, low grain growth efficiencies, and long dust lifetimes. We speculate that these models provide an alternative to earlier work that required vigorous dust destruction and efficient grain growth on timescales $\lesssim$ a few Myr (e.g., Draine 2009; Zhukovska 2014; Feldmann 2015; De Vis et al.

2017b) to explain local galaxy scaling relations. These long dust lifetimes and reduced grain growth efficiencies could reduce the tension with grain-surface chemical models (e.g., Barlow 1978; Ferrara et al. 2016; Ceccarelli et al. 2018; Jones & Ysard 2019) that have not been able to come up with efficient grain growth mechanisms in interstellar clouds. Our model results might furthermore help solving the dust budget problem at high redshifts (e.g., Bertoldi et al. 2003; Priddey et al. 2003; Watson et al. 2015), in case similar dust production and destruction efficiencies would apply to those primordial galaxies.

We caution that model parameter degeneracies between supernova dust production, grain growth and dust destruction efficiencies can not fully be resolved based on the current set of global galaxy scaling laws presented in this work. In future work, we plan to expand DEUS with radially dependent gaseous flows, to explore alternative recipes to describe grain growth and dust destruction processes, and to include additional observational constraints (e.g., resolved galaxy properties, and depletion factors for various elements).

ACKNOWLEDGEMENTS

We would like to thank the anonymous referee for her/his suggestions which have improved the presentation of the fitting methods and results reported in this paper. IDL gratefully acknowledges the support of the Research Foundation – Flanders (FWO). LCH was supported by the National Science Foundation of China (11721303) and the National Key R&D Program of China (2016YFA0400702). MJM acknowledges the support of the National Science Centre, Poland through the SONATA BIS grant 2018/30/E/ST9/00208.
The James Clerk Maxwell Telescope is operated by the East Asian Observatory on behalf of The National Astronomical Observatory of Japan, Academia Sinica Institute of Astronomy and Astrophysics, the Korea Astronomy and Space Science Institute, the National Astronomical Observatories of China and the Chinese Academy of Sciences (Grant No. XDB09000000), with additional funding support from the Science and Technology Facilities Council of the United Kingdom and participating universities in the United Kingdom and Canada. Additional funds for the construction of SCUBA-2 were provided by the Canada Foundation for Innovation. This data is being observed under JCMT Project ID: M16AL005. The Starlink software (Currie et al. 2014) used as part of the JINGLE data reduction process is currently supported by the East Asian Observatory.
PACS was developed by a consortium of institutes led by MPE (Germany) and including UVIE (Austria); KU Leuven, CSL, IMEC (Belgium); CEA, LAM (France); MPIA (Germany); INAFIFSI/ OAA/OAP/OAT, LENS, SISSA (Italy); IAC (Spain). This development has been supported by the funding agencies BMVIT (Austria), ESA-PRODEX (Belgium), CEA/CNES (France), DLR (Germany), ASI/INAF (Italy), and CICYT/ MCYT (Spain).
SPIRE was developed by a consortium of institutes led by Cardiff University (UK) and including Univ. Lethbridge (Canada); NAOC (China); CEA, LAM (France); IFSI, Univ. Padua (Italy); IAC (Spain); Stockholm Observatory (Sweden); Imperial College London, RAL, UCL-MSSL, UKATC, Univ. Sussex (UK); and Caltech, JPL, NHSC, Univ. Colorado (USA). This development has been supported by national funding agencies: CSA (Canada); NAOC (China); CEA, CNES, CNRS (France); ASI (Italy); MCINN (Spain); SNSB (Sweden); STFC and UKSA (UK); and NASA (USA).

AFFILIATIONS

[1]Sterrenkundig Observatorium, Ghent University, Krijgslaan 281 - S9, 9000 Gent, Belgium
[2]Dept. of Physics & Astronomy, University College London, Gower Street, London WC1E 6BT, UK
[3]Dept. Física Teórica y del Cosmos, Universidad de Granada, Spain
[4]Instituto Universitario Carlos I de Física Teórica y Computacional, Universidad de Granada, 18071, Granada, Spain
[5]School of Physics and Astronomy, Cardiff University, Queens Buildings, The Parade, Cardiff CF24 3AA
[6]Space Telescope Science Institute, 3700 San Martin Drive, Baltimore, Maryland, 21211, USA
[7]Department of Physics & Astronomy, McMaster University, Hamilton, ON L8S 4M1 Canada
[8]Université Paris-Saclay, CNRS, Institut d'Astrophysique Spatiale, 91405, Orsay, France
[9]Steward Observatory, University of Arizona, 933 N Cherry Avenue, Tucson, AZ 85721-0065, USA
[10]George P. and Cynthia Woods Mitchell Institute for Fundamental Physics and Astronomy, Texas A&M University, College Station, TX 77843-4242, USA
[11]Centre for Astrophysics Research, University of Hertfordshire, College Lane, AL10 9AB, UK
[12]Sub-department of Astrophysics, University of Oxford, Denys Wilkinson Building, Keble Road, Oxford, OX1 3RH, UK
[13]Yonsei Frontier Lab and Department of Astronomy, Yonsei University, 50 Yonsei-ro, Seodaemun-gu, Seoul 03722, Republic of Korea
[14]Blackett Laboratory, Physics Department, Imperial College, London, SW7 2AZ, UK
[15]Institute of Astronomy & Astrophysics, Academia Sinica, Taipei, 10617, Taiwan
[16]Shanghai Astronomical Observatory, 80 Nandan Road, Xuhui District, Shanghai, China 200030
[17]Purple Mountain Observatory & Key Lab. of Radio Astronomy, Chinese Academy of Sciences, Nanjing 210034, China
[18]Centre for Astronomy, National University of Ireland, Galway, University Road, Galway, Ireland H91 TK33
[19]Kavli Institute for Astronomy and Astrophysics, Peking University, Beijing 100871, China
[20]Department of Astronomy, School of Physics, Peking University, Beijing 100871, China
[21]Korea Astronomy and Space Science Institute, 776 Daedeokdae-ro, Yuseong-gu, Daejeon 34055, Republic of Korea
[22]Astronomical Observatory Institute, Faculty of Physics, Adam Mickiewicz University, ul. Słoneczna 36, 60-286 Poznań, Poland
[23]Tsinghua Center for Astrophysics and Physics Department, Tsinghua University, Beijing 100084, China
[24]Shanghai Astronomical Observatory, Chinese Academy of

Sciences, 80 Nandan Road, Shanghai, 200030, PR China
[25]Max Planck Institute for Astronomy, Königstuhl 17, D-69117 Heidelberg, Germany
[26]Astronomy Centre, Department of Physics and Astronomy, University of Sussex, Brighton BN1 9QH, England
[27]Department of Physics, Zhejiang University, Hangzhou, Zhejiang 310027, China
[28]National Astronomical Observatory of China, 20A Datun Road, Chaoyang District, Beijing, China 100012

REFERENCES

Accurso G., et al., 2017, MNRAS, 470, 4750
Amorín R., Muñoz-Tuñón C., Aguerri J. A. L., Planesas P., 2016, A&A, 588, A23
An D., 2019, ApJ, 878, L31
Aoyama S., Hou K.-C., Shimizu I., Hirashita H., Todoroki K., Choi J.-H., Nagamine K., 2017, MNRAS, 466, 105
Asano R. S., Takeuchi T. T., Hirashita H., Inoue A. K., 2013, Earth, Planets, and Space, 65, 213
Asplund M., Grevesse N., Sauval A. J., Scott P., 2009, ARA&A, 47, 481
Aver E., Olive K. A., Porter R. L., Skillman E. D., 2013, J. Cosmology Astropart. Phys., 11, 017
Balser D. S., 2006, AJ, 132, 2326
Barlow M. J., 1978, MNRAS, 183, 417
Barlow M. J., et al., 2010, A&A, 518, L138
Belfiore F., et al., 2017, MNRAS, 469, 151
Belfiore F., Vincenzo F., Maiolino w. R., Matteucci F., 2019, MNRAS, p. 1173
Bertoldi F., Carilli C. L., Cox P., Fan X., Strauss M. A., Beelen A., Omont A., Zylka R., 2003, A&A, 406, L55
Bevan A., Barlow M. J., 2016, MNRAS, 456, 1269
Bianchi S., Schneider R., 2007, MNRAS, 378, 973
Bianchi S., et al., 2018, A&A, 620, A112
Bigiel F., Leroy A., Walter F., Brinks E., de Blok W. J. G., Madore B., Thornley M. D., 2008, AJ, 136, 2846
Biscaro C., Cherchneff I., 2016, A&A, 589, A132
Bocchio M., Marassi S., Schneider R., Bianchi S., Limongi M., Chieffi A., 2016, A&A, 587, A157
Bolatto A. D., Wolfire M., Leroy A. K., 2013, ARA&A, 51, 207
Boselli A., Boissier S., Cortese L., Gil de Paz A., Seibert M., Madore B. F., Buat V., Martin D. C., 2006, ApJ, 651, 811
Boselli A., et al., 2010, PASP, 122, 261
Boselli A., Cortese L., Boquien M., 2014a, A&A, 564, A65
Boselli A., Cortese L., Boquien M., Boissier S., Catinella B., Lagos C., Saintonge A., 2014b, A&A, 564, A66
Bothwell M. S., Maiolino R., Kennicutt R., Cresci G., Mannucci F., Marconi A., Cicone C., 2013, MNRAS, 433, 1425
Boyer M. L., et al., 2019, ApJ, 879, 109
Bundy K., et al., 2015, ApJ, 798, 7
Calura F., Pipino A., Matteucci F., 2008, A&A, 479, 669
Carniani S., et al., 2017, A&A, 605, A42
Casasola V., et al., 2019, arXiv e-prints, p. arXiv:1911.09187
Catinella B., et al., 2018, MNRAS, 476, 875
Ceccarelli C., Viti S., Balucani N., Taquet V., 2018, MNRAS, 476, 1371
Chabrier G., 2003, PASP, 115, 763
Cicone C., et al., 2014, A&A, 562, A21
Ciesla L., et al., 2012, A&A, 543, A161
Ciesla L., et al., 2016, A&A, 585, A43
Cigan P., et al., 2019, ApJ, 886, 51
Clark C. J. R., et al., 2015, MNRAS, 452, 397
Clark C. J. R., Schofield S. P., Gomez H. L., Davies J. I., 2016, MNRAS, 459, 1646
Clark C. J. R., et al., 2018, A&A, 609, A37
Clark C. J. R., et al., 2019, MNRAS, 489, 5256
Cormier D., et al., 2015, A&A, 578, A53
Cormier D., et al., 2019, A&A, 626, A23
Cortese L., Catinella B., Boissier S., Boselli A., Heinis S., 2011, MNRAS, 415, 1797
Cortese L., et al., 2012, A&A, 540, A52
Cortese L., et al., 2014, MNRAS, 440, 942
Cortese L., et al., 2016, MNRAS, 459, 3574
Cowie L. L., Songaila A., Hu E. M., Cohen J. G., 1996, AJ, 112, 839
Dale D. A., Helou G., Contursi A., Silbermann N. A., Kolhatkar S., 2001, ApJ, 549, 215
Dale D. A., et al., 2017, ApJ, 837, 90
De Cia A., Ledoux C., Mattsson L., Petitjean P., Srianand R., Gavignaud I., Jenkins E. B., 2016, A&A, 596, A97
De Looze I., et al., 2016, MNRAS, 459, 3900
De Looze I., Barlow M. J., Swinyard B. M., Rho J., Gomez H. L., Matsuura M., Wesson R., 2017a, MNRAS, 465, 3309
De Looze I., et al., 2017b, MNRAS, 465, 3741
De Looze I., et al., 2019, MNRAS, 488, 164
De Vis P., et al., 2017a, MNRAS, 464, 4680
De Vis P., et al., 2017b, MNRAS, 471, 1743
De Vis P., et al., 2019, A&A, 623, A5
Dekel A., et al., 2009, Nature, 457, 451
Dell'Agli F., Valiante R., Kamath D., Ventura P., García-Hernández D. A., 2019, MNRAS, 486, 4738
Demyk K., et al., 2017a, A&A, 600, A123
Demyk K., et al., 2017b, A&A, 606, A50
Draine B. T., 2009, in Henning T., Grün E., Steinacker J., eds, Astronomical Society of the Pacific Conference Series Vol. 414, Cosmic Dust - Near and Far. p. 453 (arXiv:0903.1658)
Driver S. P., Popescu C. C., Tuffs R. J., Liske J., Graham A. W., Allen P. D., de Propris R., 2007, MNRAS, 379, 1022
Dwek E., 1998, ApJ, 501, 643
Eales S., et al., 2010, PASP, 122, 499
Eales S., et al., 2012, ApJ, 761, 168
Eales S., de Vis P., Smith M. W. L., Appah K., Ciesla L., Duffield C., Schofield S., 2017, MNRAS, 465, 3125
Feldmann R., 2015, MNRAS, 449, 3274
Ferrara A., Viti S., Ceccarelli C., 2016, MNRAS, 463, L112
Ferrarotti A. S., Gail H.-P., 2006, A&A, 447, 553
Fluetsch A., et al., 2019, MNRAS, 483, 4586
Foreman-Mackey D., Hogg D. W., Lang D., Goodman J., 2013, PASP, 125, 306
Galametz M., Madden S. C., Galliano F., Hony S., Bendo G. J., Sauvage M., 2011, A&A, 532, A56
Gall C., et al., 2014, Nature, 511, 326
Garnett D. R., 2002, ApJ, 581, 1019
Ginolfi M., Graziani L., Schneider R., Marassi S., Valiante R., Dell'Agli F., Ventura P., Hunt L. K., 2018, MNRAS, 473, 4538
Gomez H. L., et al., 2012, ApJ, 760, 96
Goodman J., Weare J., 2010, Communications in Applied Mathematics and Computational Science, Vol.˜5, No.˜1, p.˜65-80, 2010, 5, 65
Graziani L., Schneider R., Ginolfi M., Hunt L. K., Maio U., Glatzle M., Ciardi B., 2019, arXiv e-prints, p. arXiv:1909.07388
Groves B. A., et al., 2015, ApJ, 799, 96
Hartmann J., 1904, ApJ, 19, 286
Hashimoto T., et al., 2018, Nature, 557, 392
Haynes M. P., Giovanelli R., 1984, AJ, 89, 758
Haynes M. P., et al., 2018, ApJ, 861, 49
Hayward C. C., Hopkins P. F., 2017, MNRAS, 465, 1682
Henning T., Jäger C., Rouillé G., Fulvio D., Krasnokutski S. A., 2018, in Cunningham M., Millar T., Aikawa Y., eds, IAU Symposium Vol. 332, IAU Symposium. pp 312–319, doi:10.1017/S174392131700686X

Hirashita H., 2015, MNRAS, 447, 2937
Hu C.-Y., Zhukovska S., Somerville R. S., Naab T., 2019, MNRAS, 487, 3252
Hughes T. M., Cortese L., Boselli A., Gavazzi G., Davies J. I., 2013, A&A, 550, A115
Hunt L. K., et al., 2019, A&A, 621, A51
Hunter D. A., Zahedy F., Bowsher E. C., Wilcots E. M., Kepley A. A., Gaal V., 2011, AJ, 142, 173
Inoue A. K., et al., 2016, Science, 352, 1559
Janowiecki S., Cortese L., Catinella B., Goodwin A. J., 2018, MNRAS, 476, 1390
Jones A. P., Nuth J. A., 2011, A&A, 530, A44
Jones A. P., Ysard N., 2019, A&A, 627, A38
Jones A. P., Tielens A. G. G. M., Hollenbach D. J., McKee C. F., 1994, ApJ, 433, 797
Jones A. P., Tielens A. G. G. M., Hollenbach D. J., 1996, ApJ, 469, 740
Jones A. P., Fanciullo L., Köhler M., Verstraete L., Guillet V., Bocchio M., Ysard N., 2013, A&A, 558, A62
Jones A. P., Köhler M., Ysard N., Bocchio M., Verstraete L., 2017, A&A, 602, A46
Kalberla P. M. W., Kerp J., 2009, ARA&A, 47, 27
Kennicutt Jr. R. C., 1998, ApJ, 498, 541
Kennicutt R. C., Evans N. J., 2012, ARA&A, 50, 531
Kennicutt Robert C. J., Bresolin F., Garnett D. R., 2003, ApJ, 591, 801
Kennicutt R. C., et al., 2011, PASP, 123, 1347
Kewley L. J., Ellison S. L., 2008, ApJ, 681, 1183
Kirchschlager F., Schmidt F. D., Barlow M. J., Fogerty E. L., Bevan A., Priestley F. D., 2019, MNRAS, 489, 4465
Kobulnicky H. A., Kewley L. J., 2004, ApJ, 617, 240
Köhler M., Jones A., Ysard N., 2014, A&A, 565, L9
Krasnokutski S. A., Rouillé G., Jäger C., Huisken F., Zhukovska S., Henning T., 2014, ApJ, 782, 15
Lakićević M., et al., 2015, ApJ, 799, 50
Lamperti I., et al., 2019, MNRAS, 489, 4389
Laporte N., et al., 2017, ApJ, 837, L21
Lebouteiller V., et al., 2012, A&A, 548, A91
Leroy A. K., Walter F., Brinks E., Bigiel F., de Blok W. J. G., Madore B., Thornley M. D., 2008, AJ, 136, 2782
Lian J., Thomas D., Maraston C., Goddard D., Comparat J., Gonzalez-Perez V., Ventura P., 2018a, MNRAS, 474, 1143
Lian J., et al., 2018b, MNRAS, 476, 3883
Lisenfeld U., Ferrara A., 1998, ApJ, 496, 145
Madden S. C., Cormier D., 2019, in McQuinn K. B. W., Stierwalt S., eds, IAU Symposium Vol. 344, Dwarf Galaxies: From the Deep Universe to the Present. pp 240–254 (arXiv:1810.09953), doi:10.1017/S1743921318007147
Magdis G. E., et al., 2012, ApJ, 760, 6
Magrini L., et al., 2011, A&A, 535, A13
Mancini M., Schneider R., Graziani L., Valiante R., Dayal P., Maio U., Ciardi B., Hunt L. K., 2015, MNRAS, 451, L70
Marassi S., Schneider R., Limongi M., Chieffi A., Graziani L., Bianchi S., 2019, MNRAS, 484, 2587
Markwardt C. B., 2009, in Bohlender D. A., Durand D., Dowler P., eds, Astronomical Society of the Pacific Conference Series Vol. 411, Astronomical Data Analysis Software and Systems XVIII. p. 251 (arXiv:0902.2850)
Matsuura M., Woods P. M., Owen P. J., 2013, MNRAS, 429, 2527
Matsuura M., et al., 2015, ApJ, 800, 50
Matsuura M., et al., 2019, MNRAS, 482, 1715
Mattsson L., Andersen A. C., 2012, MNRAS, 423, 38
Mattsson L., Andersen A. C., Munkhammar J. D., 2012, MNRAS, 423, 26
McKee C., 1989, in Allamandola L. J., Tielens A. G. G. M., eds, IAU Symposium Vol. 135, Interstellar Dust. p. 431
Mesa-Delgado A., Esteban C., García-Rojas J., Luridiana V., Bautista M., Rodríguez M., López-Martín L., Peimbert M., 2009, MNRAS, 395, 855
Micelotta E. R., Dwek E., Slavin J. D., 2016, A&A, 590, A65
Michałowski M. J., 2015, A&A, 577, A80
Michałowski M. J., Murphy E. J., Hjorth J., Watson D., Gall C., Dunlop J. S., 2010, A&A, 522, A15
Morgan H. L., Edmunds M. G., 2003, MNRAS, 343, 427
Moustakas J., Kennicutt Jr. R. C., Tremonti C. A., Dale D. A., Smith J.-D. T., Calzetti D., 2010, ApJS, 190, 233
Muratov A. L., Kereš D., Faucher-Giguère C.-A., Hopkins P. F., Quataert E., Murray N., 2015, MNRAS, 454, 2691
Naab T., Ostriker J. P., 2017, ARA&A, 55, 59
Nanni A., Bressan A., Marigo P., Girardi L., 2013, MNRAS, 434, 2390
Nath B. B., Laskar T., Shull J. M., 2008, ApJ, 682, 1055
Nersesian A., et al., 2019, A&A, 624, A80
Noeske K. G., et al., 2007, ApJ, 660, L43
Nozawa T., Kozasa T., Habe A., Dwek E., Umeda H., Tominaga N., Maeda K., Nomoto K., 2007, ApJ, 666, 955
Oldham L., Auger M., 2018, MNRAS, 474, 4169
Pagel B. E. J., 1997, Nucleosynthesis and Chemical Evolution of Galaxies
Pannella M., et al., 2009, ApJ, 698, L116
Pappalardo C., Lançon A., Vollmer B., Ocvirk P., Boissier S., Boselli A., 2010, A&A, 514, A33
Peters T., et al., 2017, MNRAS, 467, 4322
Pettini M., Pagel B. E. J., 2004, MNRAS, 348, L59
Planck Collaboration et al., 2016, A&A, 586, A132
Poetrodjojo H., et al., 2018, MNRAS, 479, 5235
Popping G., Somerville R. S., Trager S. C., 2014, MNRAS, 442, 2398
Popping G., Somerville R. S., Galametz M., 2017, MNRAS, 471, 3152
Prantzos N., Casse M., Vangioni-Flam E., 1993, ApJ, 403, 630
Priddey R. S., Isaak K. G., McMahon R. G., Robson E. I., Pearson C. P., 2003, MNRAS, 344, L74
Priestley F. D., Barlow M. J., De Looze I., 2019, MNRAS, 485, 440
Priestley F. D., Barlow M. J., De Looze I., Chawner H., 2020, MNRAS, 491, 6020
Rémy-Ruyer A., et al., 2014, A&A, 563, A31
Rémy-Ruyer A., et al., 2015, A&A, 582, A121
Robitaille T. P., Whitney B. A., 2010, ApJ, 710, L11
Rodighiero G., et al., 2010, A&A, 518, L25
Rouillé G., Jäger C., Krasnokutski S. A., Krebsz M., Henning T., 2015, arXiv e-prints,
Rowlands K., Gomez H. L., Dunne L., Aragón-Salamanca A., Dye S., Maddox S., da Cunha E., van der Werf P., 2014, MNRAS, 441, 1040
Saintonge A., et al., 2011, MNRAS, 415, 32
Saintonge A., et al., 2016, MNRAS, 462, 1749
Saintonge A., et al., 2018, MNRAS, 481, 3497
Sánchez Almeida J., Elmegreen B. G., Muñoz-Tuñón C., Elmegreen D. M., 2014, A&ARv, 22, 71
Sánchez-Blázquez P., et al., 2014, A&A, 570, A6
Sánchez S. F., et al., 2017, MNRAS, 469, 2121
Sandstrom K. M., et al., 2013, ApJ, 777, 5
Santini P., et al., 2017, ApJ, 847, 76
Sarangi A., Cherchneff I., 2015, A&A, 575, A95
Schaller G., Schaerer D., Meynet G., Maeder A., 1992, A&AS, 96, 269
Schmidt M., 1959, ApJ, 129, 243
Schneider R., Hunt L., Valiante R., 2016, MNRAS, 457, 1842
Schruba A., et al., 2012, AJ, 143, 138
Scoville N., et al., 2014, ApJ, 783, 84
Scoville N., et al., 2016, ApJ, 820, 83
Silk J., Mamon G. A., 2012, Research in Astronomy and Astrophysics, 12, 917
Silvia D. W., Smith B. D., Shull J. M., 2010, ApJ, 715, 1575

Slavin J. D., Dwek E., Jones A. P., 2015, ApJ, 803, 7
Smit R., et al., 2014, ApJ, 784, 58
Smith M. W. L., et al., 2012, ApJ, 748, 123
Smith M. W. L., et al., 2019, MNRAS, 486, 4166
Temim T., Dwek E., 2013, ApJ, 774, 8
Temim T., Dwek E., Tchernyshyov K., Boyer M. L., Meixner M., Gall C., Roman-Duval J., 2015, ApJ, 799, 158
Temim T., Dwek E., Arendt R. G., Borkowski K. J., Reynolds S. P., Slane P., Gelfand J. D., Raymond J. C., 2017, ApJ, 836, 129
Thomas D., et al., 2013, MNRAS, 431, 1383
Tremonti C. A., et al., 2004, ApJ, 613, 898
Triani D. P., Sinha M., Croton D. J., Pacifici C., Dwek E., 2020, MNRAS,
Trumpler R. J., 1930, PASP, 42, 214
Valiante R., Schneider R., Bianchi S., Andersen A. C., 2009, MNRAS, 397, 1661
Valiante R., Schneider R., Salvadori S., Bianchi S., 2011, MNRAS, 416, 1916
Vílchez J. M., Relaño M., Kennicutt R., De Looze I., Mollá M., Galametz M., 2019, MNRAS, 483, 4968
Walter F., et al., 2017, ApJ, 835, 265
Watson D., Christensen L., Knudsen K. K., Richard J., Gallazzi A., Michałowski M. J., 2015, Nature, 519, 327
Wesson R., Barlow M. J., Matsuura M., Ercolano B., 2015, MNRAS, 446, 2089
Woosley S. E., Weaver T. A., 1995, ApJS, 101, 181
Zapartas E., et al., 2017, A&A, 601, A29
Zhukovska S., 2014, A&A, 562, A76
Zhukovska S., Dobbs C., Jenkins E. B., Klessen R. S., 2016, ApJ, 831, 147
Zhukovska S., Henning T., Dobbs C., 2018, ApJ, 857, 94
da Cunha E., Eminian C., Charlot S., Blaizot J., 2010, MNRAS, 403, 1894
van den Hoek L. B., Groenewegen M. A. T., 1997, A&AS, 123, 305

APPENDIX A: DUST MASS DETERMINATION

Galaxy dust masses have been inferred from Bayesian dust spectral energy distribution (SED) models fit to the mid-infrared to sub-millimetre emission observed in five samples of nearby galaxies (JINGLE, HRS, KINGFISH, HAPLESS, HiGH). In brief, the Bayesian dust SED models use the THEMIS (The Heterogeneous dust Evolution Model for Interstellar Solids, Jones et al. 2013, 2017) dust model composition, in addition to two different prescriptions for the radiation field intensity: 1. single interstellar radiation field (ISRF) and 2. multi-component ISRF. In this work, we rely on the dust mass measurements inferred from the second model which relies on the multi-component radiation field prescription from Dale et al. (2001). More specifically, the starlight intensity is assumed to be distributed between $U_{\rm min}$ and $U_{\rm max}$ and the fractional dust mass heated by each ISRF intensity is assumed to be $dM/dU \propto U^{-\alpha_{\rm ISRF}}$. We fix $U_{\rm max}$=10^7 (e.g., Nersesian et al. 2019), and vary the minimum starlight intensity, $U_{\rm min}$, as well as the slope of the ISRF power-law distribution, $\alpha_{\rm ISRF}$, in our models. The THEMIS dust mix includes a set of small (sCM20) and large (lCM20) amorphous hydrocarbon grains (a-C(:H)) and large silicates with iron nano-particle inclusions (a-Sil$_{\rm Fe}$), for which the optical properties were derived from laboratory studies, and the size distribution and abundances of grain species were calibrated to reproduce the extinction and emission observed in the diffuse ISM of the Milky Way (Jones et al. 2013; Köhler et al. 2014). To model the diversity of dust SEDs observed in the local Universe, we allow for variations in the THEMIS dust mix by varying the slope $\alpha_{\rm sCM20}$ of the grain size distribution of small hydrocarbons, and the relative dust masses of small hydrocarbons, $M_{\rm sCM20}$, and large (hydrocarbon and amorphous silicate) dust grains, $M_{\rm lCM20+sil}$. An example dust SED model fit for the galaxy JINGLE 26 has been shown in Figure A1 (left panel). The lower and upper limit uncertainties on galaxy dust masses have been inferred from the 16th and 84th percentiles in the posterior PDFs (see Fig. A1, right panel) and have been tabulated in Table A1 for all galaxies.

Table A1: Overview of the dust masses inferred for the JINGLE, HRS, HAPLESS, HiGH and KINGFISH galaxies considered in the scaling relations presented in this work. The median dust masses have been inferred from the posterior PDFs while the 16th and 84th percentiles are used to approximate the lower and upper limits on these modelled dust masses. The full galaxy names for JINGLE and HRS galaxies can be retrieved from Saintonge et al. (2018) and Boselli et al. (2010).

Galaxy	$\log(M_{\rm dust}/M_{\odot})$	-dex	+dex
JINGLE:			
JINGLE 0	6.68	-0.06	+0.06
JINGLE 1	7.12	-0.08	+0.10
JINGLE 2	6.82	-0.23	+0.25
JINGLE 3	6.53	-0.05	+0.05
JINGLE 4	7.08	-0.06	+0.06
JINGLE 5	7.34	-0.06	+0.06
JINGLE 6	7.18	-0.08	+0.08
JINGLE 7	6.96	-0.07	+0.07
JINGLE 8	6.79	-0.09	+0.09
JINGLE 9	7.05	-0.08	+0.08
JINGLE 10	7.35	-0.06	+0.06
JINGLE 11	7.44	-0.09	+0.08
JINGLE 12	6.98	-0.09	+0.09
JINGLE 13	6.62	-0.10	+0.10
JINGLE 15	7.09	-0.06	+0.06
JINGLE 16	7.11	-0.07	+0.07
JINGLE 17	6.69	-0.09	+0.09
JINGLE 18	6.91	-0.12	+0.13
JINGLE 19	7.46	-0.08	+0.09
JINGLE 20	7.08	-0.09	+ 0.09
JINGLE 21	7.23	-0.13	+0.15
JINGLE 22	7.73	-0.06	+0.05
JINGLE 23	7.34	-0.05	+0.05
JINGLE 24	6.93	-0.14	+0.16
JINGLE 25	7.24	-0.05	+0.05
JINGLE 26	6.97	-0.05	+0.05
JINGLE 27	7.33	-0.08	+0.09
JINGLE 28	7.43	-0.07	+0.08
JINGLE 30	7.06	-0.11	+0.11
JINGLE 31	6.86	-0.08	+0.09
JINGLE 32	6.92	-0.08	+0.08
JINGLE 33	6.66	-0.05	+0.04
JINGLE 34	7.29	-0.07	+0.07
JINGLE 35	7.22	-0.05	+0.05
JINGLE 36	6.87	-0.07	+0.07
JINGLE 38	6.87	-0.06	+0.05
JINGLE 39	7.17	-0.08	+0.08
JINGLE 40	7.81	-0.05	+0.05
JINGLE 41	7.83	-0.04	+0.04
JINGLE 43	8.02	-0.04	+0.03
JINGLE 44	7.81	-0.06	+0.07
JINGLE 45	7.95	-0.05	+0.05
JINGLE 46	6.91	-0.13	+0.14

Continued on next column

Continued from previous column			
Galaxy name	$\log(M_{\rm dust}/M_{\odot})$	-dex	+dex
JINGLE 47	7.49	-0.05	+0.04
JINGLE 48	7.39	-0.04	+0.04
JINGLE 49	7.55	-0.05	+0.04
JINGLE 50	7.36	-0.13	+0.12
JINGLE 51	7.37	-0.04	+0.04
JINGLE 52	7.22	-0.09	+0.09
JINGLE 53	6.84	-0.09	+0.08
JINGLE 54	7.76	-0.05	+0.04
JINGLE 55	7.59	-0.04	+0.04
JINGLE 56	7.59	-0.05	+0.05
JINGLE 57	7.37	-0.09	+0.09
JINGLE 58	7.10	-0.11	+0.11
JINGLE 60	7.18	-0.10	+0.09
JINGLE 61	7.09	-0.07	+0.08
JINGLE 63	6.28	-0.13	+0.12
JINGLE 64	6.98	-0.09	+0.08
JINGLE 66	7.93	-0.09	+0.05
JINGLE 69	6.98	-0.06	+0.07
JINGLE 70	7.50	-0.05	+0.06
JINGLE 71	7.12	-0.06	+0.06
JINGLE 72	7.51	-0.04	+0.04
JINGLE 73	7.24	-0.09	+0.09
JINGLE 74	7.24	-0.06	+0.06
JINGLE 75	7.48	-0.07	+0.07
JINGLE 76	7.24	-0.04	+0.04
JINGLE 77	7.56	-0.04	+0.04
JINGLE 78	7.02	-0.10	+0.12
JINGLE 79	6.97	-0.09	+0.09
JINGLE 80	7.08	-0.09	+0.09
JINGLE 81	7.24	-0.05	+0.06
JINGLE 82	7.10	-0.09	+0.09
JINGLE 83	7.71	-0.06	+0.06
JINGLE 84	7.53	-0.06	+0.06
JINGLE 85	6.82	-0.07	+0.07
JINGLE 86	7.64	-0.05	+0.05
JINGLE 87	7.72	-0.07	+0.06
JINGLE 88	7.30	-0.09	+0.10
JINGLE 89	7.50	-0.05	+0.05
JINGLE 90	7.69	-0.07	+0.07
JINGLE 92	7.92	-0.06	+0.06
JINGLE 93	7.24	-0.08	+0.08
JINGLE 96	7.09	-0.13	+0.16
JINGLE 97	7.33	-0.09	+0.11
JINGLE 98	7.46	-0.09	+0.08
JINGLE 99	8.11	-0.05	+0.05
JINGLE 100	7.35	-0.05	+0.04
JINGLE 101	7.74	-0.04	+0.04
JINGLE 102	7.68	-0.06	+0.05
JINGLE 103	7.38	-0.05	+0.05
JINGLE 105	7.32	-0.07	+0.05
JINGLE 106	7.66	-0.05	+0.06
JINGLE 107	7.92	-0.10	+0.09
JINGLE 108	7.75	-0.05	+0.05
JINGLE 109	7.47	-0.08	+0.08
Continued on next column			

Continued from previous column			
Galaxy name	$\log(M_{\rm dust}/M_{\odot})$	-dex	+dex
JINGLE 110	7.46	-0.29	+0.27
JINGLE 111	7.48	-0.06	+0.06
JINGLE 112	7.72	-0.09	+0.09
JINGLE 113	7.40	-0.08	+0.09
JINGLE 114	7.68	-0.06	+0.05
JINGLE 115	7.29	-0.05	+0.05
JINGLE 117	7.58	-0.33	+0.30
JINGLE 118	8.18	-0.04	+0.04
JINGLE 120	8.04	-0.15	+0.15
JINGLE 121	7.92	-0.06	+0.07
JINGLE 122	8.00	-0.05	+0.05
JINGLE 123	7.57	-0.05	+0.05
JINGLE 125	7.78	-0.06	+0.06
JINGLE 127	7.85	-0.06	+0.06
JINGLE 128	7.87	-0.07	+0.06
JINGLE 129	7.50	-0.10	+0.10
JINGLE 131	7.52	-0.05	+0.05
JINGLE 132	8.02	-0.12	+0.07
JINGLE 133	7.55	-0.04	+0.04
JINGLE 134	7.71	-0.07	+0.07
JINGLE 135	7.44	-0.06	+0.06
JINGLE 136	7.75	-0.05	+0.04
JINGLE 137	6.90	-0.29	+0.51
JINGLE 138	7.22	-0.11	+0.10
JINGLE 139	7.66	-0.10	+0.09
JINGLE 140	7.53	-0.08	+0.07
JINGLE 141	7.56	-0.07	+0.06
JINGLE 143	7.47	-0.06	+0.06
JINGLE 144	7.56	-0.05	+0.04
JINGLE 145	6.56	-0.09	+0.10
JINGLE 146	7.49	-0.04	+0.04
JINGLE 147	7.64	-0.05	+0.04
JINGLE 148	7.42	-0.05	+0.05
JINGLE 149	7.31	-0.04	+0.04
JINGLE 151	8.16	-0.08	+0.06
JINGLE 152	7.72	-0.05	+0.05
JINGLE 154	8.21	-0.04	+0.03
JINGLE 155	7.82	-0.08	+0.07
JINGLE 156	7.77	-0.06	+0.05
JINGLE 160	7.03	-0.05	+0.05
JINGLE 161	7.78	-0.12	+0.12
JINGLE 162	7.83	-0.05	+0.06
JINGLE 163	7.59	-0.07	+0.07
JINGLE 164	7.33	-0.09	+0.09
JINGLE 165	7.60	-0.04	+0.04
JINGLE 166	7.67	-0.07	+0.07
JINGLE 167	8.16	-0.05	+0.05
JINGLE 168	8.07	-0.08	+0.08
JINGLE 169	7.43	-0.07	+0.07
JINGLE 170	7.74	-0.08	+0.08
JINGLE 171	7.86	-0.11	+0.08
JINGLE 172	7.54	-0.09	+0.09
JINGLE 173	7.35	-0.06	+0.06
JINGLE 174	7.97	-0.13	+0.13
Continued on next column			

Continued from previous column

Galaxy name	$\log(M_{\rm dust}/M_\odot)$	-dex	+dex
JINGLE 175	7.86	-0.08	+0.07
JINGLE 176	7.77	-0.06	+0.05
JINGLE 178	7.64	-0.07	+0.07
JINGLE 181	7.71	-0.06	+0.07
JINGLE 183	7.20	-0.05	+0.05
JINGLE 184	7.92	-0.06	+0.06
JINGLE 185	7.36	-0.09	+0.08
JINGLE 187	8.05	-0.08	+0.09
JINGLE 189	7.90	-0.05	+0.05
JINGLE 191	7.55	-0.06	+0.05
HRS:			
HRS 2	6.12	-0.04	+0.04
HRS 3	5.78	-0.10	+0.12
HRS 8	7.33	-0.05	+0.05
HRS 9	6.40	-0.05	+0.06
HRS 10	6.13	-0.10	+0.12
HRS 11	6.79	-0.04	+0.04
HRS 12	5.51	-0.06	+0.06
HRS 13	7.41	-0.03	+0.03
HRS 15	7.52	-0.05	+0.05
HRS 16	7.10	-0.03	+0.03
HRS 17	7.03	-0.04	+0.04
HRS 19	6.83	-0.05	+0.05
HRS 20	6.96	-0.03	+0.03
HRS 23	7.09	-0.03	+0.03
HRS 24	7.37	-0.04	+0.04
HRS 25	6.91	-0.04	+0.04
HRS 26	6.09	-0.08	+0.08
HRS 27	6.35	-0.04	+0.05
HRS 28	6.61	-0.04	+0.04
HRS 29	6.52	-0.05	+0.05
HRS 30	6.51	-0.06	+0.07
HRS 31	6.87	-0.05	+0.05
HRS 33	6.87	-0.04	+0.04
HRS 34	7.04	-0.05	+0.04
HRS 37	6.59	-0.04	+0.04
HRS 38	6.62	-0.05	+0.06
HRS 39	6.60	-0.07	+0.09
HRS 40	6.51	-0.04	+0.04
HRS 41	6.57	-0.06	+0.05
HRS 42	7.21	-0.05	+0.05
HRS 44	5.98	-0.06	+0.06
HRS 45	6.77	-0.05	+0.05
HRS 46	6.44	-0.04	+0.04
HRS 47	6.72	-0.09	+0.09
HRS 48	7.44	-0.04	+0.04
HRS 50	7.04	-0.03	+0.03
HRS 51	6.69	-0.05	+0.05
HRS 52	5.94	-0.07	+0.08
HRS 53	6.90	-0.04	+0.04
HRS 54	6.60	-0.05	+0.05
HRS 55	6.94	-0.04	+0.04
HRS 56	7.25	-0.03	+0.03

Continued on next column

Continued from previous column

Galaxy name	$\log(M_{\rm dust}/M_\odot)$	-dex	+dex
HRS 59	7.12	-0.05	+0.06
HRS 60	6.84	-0.06	+0.04
HRS 61	5.97	-0.08	+0.08
HRS 62	6.90	-0.10	+0.11
HRS 63	7.30	-0.04	+0.04
HRS 64	6.53	-0.08	+0.10
HRS 65	6.43	-0.07	+0.07
HRS 66	7.13	-0.04	+0.03
HRS 67	6.41	-0.10	+0.10
HRS 68	5.77	-0.05	+0.05
HRS 69	6.99	-0.06	+0.06
HRS 70	6.40	-0.06	+0.06
HRS 72	6.07	-0.07	+0.07
HRS 73	7.75	-0.03	+0.03
HRS 74	6.83	-0.05	+0.05
HRS 75	6.19	-0.15	+0.15
HRS 76	5.99	-0.10	+0.11
HRS 77	7.77	-0.04	+0.03
HRS 78	6.50	-0.07	+0.07
HRS 79	6.16	-0.10	+0.10
HRS 81	6.91	-0.04	+0.04
HRS 82	5.97	-0.05	+0.05
HRS 84	6.26	-0.04	+0.04
HRS 85	7.22	-0.04	+0.04
HRS 86	7.04	-0.07	+0.07
HRS 88	7.16	-0.07	+0.06
HRS 89	7.47	-0.06	+0.06
HRS 91	7.72	-0.03	+0.03
HRS 92	6.53	-0.05	+0.05
HRS 93	6.31	-0.06	+0.06
HRS 94	7.13	-0.06	+0.08
HRS 95	6.48	-0.03	+0.03
HRS 96	7.16	-0.03	+0.03
HRS 98	6.90	-0.04	+0.05
HRS 102	7.87	-0.03	+0.03
HRS 106	6.66	-0.06	+0.07
HRS 107	6.30	-0.06	+0.07
HRS 109	6.67	-0.06	+0.06
HRS 110	6.74	-0.06	+0.05
HRS 111	7.16	-0.03	+0.03
HRS 114	7.82	-0.03	+0.03
HRS 118	6.07	-0.17	+0.18
HRS 121	7.11	-0.04	+0.03
HRS 122	8.06	-0.03	+0.03
HRS 123	6.59	-0.05	+0.05
HRS 132	6.20	-0.07	+0.08
HRS 133	7.06	-0.10	+0.10
HRS 139	6.38	-0.06	+0.07
HRS 140	6.96	-0.06	+0.06
HRS 142	6.54	-0.04	+0.04
HRS 143	7.21	-0.04	+0.05
HRS 145	6.77	-0.06	+0.07
HRS 146	6.78	-0.05	+0.05
HRS 147	6.84	-0.04	+0.04

Continued on next column

Continued from previous column			
Galaxy name	$\log(M_{\rm dust}/M_\odot)$	-dex	+dex
HRS 148	6.97	-0.07	+0.06
HRS 154	7.06	-0.07	+0.08
HRS 157	6.68	-0.04	+0.03
HRS 158	6.89	-0.21	+0.21
HRS 169	6.59	-0.06	+0.07
HRS 177	6.41	-0.04	+0.04
HRS 182	6.69	-0.04	+0.04
HRS 187	7.12	-0.05	+0.06
HRS 188	6.91	-0.05	+0.05
HRS 189	6.36	-0.05	+0.05
HRS 194	7.99	-0.03	+0.03
HRS 196	6.91	-0.06	+0.06
HRS 198	6.75	-0.07	+0.08
HRS 201	7.69	-0.03	+0.03
HRS 203	6.81	-0.04	+0.04
HRS 204	7.84	-0.03	+0.03
HRS 205	7.53	-0.04	+0.04
HRS 212	6.33	-0.07	+0.07
HRS 213	8.27	-0.03	+0.03
HRS 215	6.99	-0.03	+0.03
HRS 216	7.38	-0.03	+0.03
HRS 227	6.87	-0.07	+0.07
HRS 237	6.62	-0.06	+0.05
HRS 238	5.59	-0.17	+0.24
HRS 239	6.85	-0.03	+0.03
HRS 242	6.83	-0.05	+0.05
HRS 244	7.12	-0.03	+0.03
HRS 246	7.27	-0.03	+0.04
HRS 247	7.57	-0.03	+0.03
HRS 251	7.87	-0.03	+0.02
HRS 252	6.58	-0.10	+0.11
HRS 255	6.88	-0.11	+0.11
HRS 257	7.27	-0.05	+0.05
HRS 259	6.78	-0.08	+0.10
HRS 262	6.89	-0.04	+0.05
HRS 263	8.19	-0.05	+0.04
HRS 264	6.35	-0.10	+0.10
HRS 266	7.45	-0.08	+0.12
HRS 267	6.77	-0.08	+0.07
HRS 268	6.83	-0.03	+0.03
HRS 271	6.75	-0.06	+0.07
HRS 273	7.05	-0.04	+0.04
HRS 274	6.79	-0.04	+0.05
HRS 275	7.01	-0.04	+0.04
HRS 276	6.56	-0.06	+0.06
HRS 279	6.93	-0.07	+0.08
HRS 280	6.38	-0.04	+0.04
HRS 281	5.82	-0.07	+0.07
HRS 283	7.04	-0.04	+0.04
HRS 284	6.80	-0.03	+0.03
HRS 286	6.70	-0.19	+0.19
HRS 287	6.78	-0.04	+0.05
HRS 289	7.34	-0.03	+0.03
HRS 290	6.04	-0.05	+0.05
		Continued on next column	

Continued from previous column			
Galaxy name	$\log(M_{\rm dust}/M_\odot)$	-dex	+dex
HRS 292	6.68	-0.04	+0.04
HRS 293	6.68	-0.04	+0.05
HRS 295	7.66	-0.03	+0.03
HRS 296	5.49	-0.08	+0.09
HRS 297	7.38	-0.03	+0.04
HRS 298	6.52	-0.04	+0.04
HRS 299	7.10	-0.05	+0.06
HRS 301	7.36	-0.06	+0.08
HRS 302	6.97	-0.11	+0.13
HRS 307	7.71	-0.04	+0.04
HRS 308	5.15	-0.08	+0.09
HRS 309	6.24	-0.07	+0.07
HRS 314	6.73	-0.07	+0.07
HRS 315	6.18	-0.23	+0.31
HRS 317	6.16	-0.13	+0.14
HRS 318	6.75	-0.05	+0.05
HRS 319	7.10	-0.06	+0.06
HRS 320	7.48	-0.08	+0.09
HRS 321	6.39	-0.04	+0.04
HRS 322	7.28	-0.10	+0.12
HRS 323	7.06	-0.04	+0.03
HAPLESS+HiGH:			
UGC 06877	5.32	-0.06	+0.06
PGC 037392	5.77	- 0.26	+ 0.27
UGC 09215	6.94	-0.07	+0.07
UM 452	5.56	- 0.20	+ 0.21
NGC 4030	7.87	-0.03	+0.03
NGC 5496	7.11	-0.07	+0.07
UGC 07000	6.36	-0.08	+0.08
UGC 09299	6.38	-0.14	+0.15
NGC 5740	7.18	-0.04	+0.04
UGC 07394	7.01	-0.25	+0.24
PGC 051719	6.19	-0.08	+0.09
NGC 5584	7.50	-0.05	+0.04
UGC 09348	6.58	-0.07	+0.07
UGC 06780	6.78	-0.34	+0.28
NGC 5719	7.46	-0.03	+0.03
NGC 5746	7.99	-0.03	+0.03
NGC 5690	7.60	-0.03	+0.03
NGC 5750	7.12	-0.05	+0.06
NGC 5705	7.36	-0.09	+0.09
UGC 09482	5.36	-0.19	+0.54
NGC 5691	6.85	-0.04	+0.04
NGC 5713	7.45	-0.03	+0.03
UGC 09470	6.05	-0.12	+0.14
UGC 06903	7.24	-0.06	+0.06
CGC G019-084	6.23	-0.06	+0.06
UM 491	5.63	- 0.30	+ 0.46
UGC 07531	5.70	-0.22	+0.32
UGC 07396	6.59	- 0.30	+ 0.33
UGC 04684	6.66	-0.19	+0.18
NGC 5725	6.32	-0.10	+0.12
UGC 06578	5.23	-0.26	+0.25
		Continued on next column	

Continued from previous column

Galaxy name	$\log(M_{\rm dust}/M_\odot)$	-dex	+dex
UGC 04673	7.41	-0.37	+0.32
UGC 04996	6.95	-0.11	+0.13
UGC 06970	6.45	-0.36	+0.30
NGC 4202	7.50	-0.07	+0.06
2MASX J14265308	7.27	-0.17	+0.19
IC 1011	7.43	-0.06	+0.06
IC 1010	7.96	-0.12	+0.11
KINGFISH:			
NGC 0337	7.00	-0.04	+0.04
NGC 0584	7.10	-0.28	+0.30
NGC 0628	7.24	-0.04	+0.05
NGC 0855	5.52	-0.05	+0.05
NGC 0925	7.18	-0.06	+0.05
NGC 1097	7.71	-0.04	+0.04
NGC 1291	7.12	-0.04	+0.04
IC 0342	7.45	-0.05	+0.05
NGC 1482	7.14	-0.04	+0.04
NGC 1512	7.20	-0.06	+0.06
NGC 2146	7.42	-0.04	+0.04
HoII	4.40	-0.04	+0.04
DDO 053	3.53	-0.06	+0.06
NGC 2798	6.82	-0.05	+0.04
NGC 2841	7.65	-0.04	+0.04
NGC 2915	4.62	-0.05	+0.05
HoI	4.77	-0.17	+0.21
NGC 2976	6.15	-0.05	+0.05
NGC 3049	6.54	-0.05	+0.06
NGC 3077	5.83	-0.04	+0.04
M81dwB	4.07	-0.10	+0.08
NGC 3184	7.38	-0.04	+0.04
NGC 3190	7.03	-0.04	+0.04
NGC 3198	7.44	-0.05	+0.05
IC 2574	5.55	-0.05	+0.05
NGC 3265	6.03	-0.05	+0.05
NGC 3351	7.07	-0.04	+0.04
NGC 3521	7.76	-0.04	+0.04
NGC 3621	7.15	-0.04	+0.04
NGC 3627	7.39	-0.04	+0.04
NGC 3773	5.66	-0.04	+0.04
NGC 3938	7.50	-0.04	+0.04
NGC 4236	6.21	-0.05	+0.05
NGC 4254	7.66	-0.04	+0.04
NGC 4321	7.73	-0.04	+0.04
NGC 4536	7.27	-0.05	+0.04
NGC 4559	6.81	-0.05	+0.05
NGC 4569	6.94	-0.03	+0.04
NGC 4579	7.40	-0.03	+0.03
NGC 4594	7.16	-0.04	+0.04
NGC 4625	6.14	-0.04	+0.04
NGC 4631	7.38	-0.05	+0.04
NGC 4826	6.43	-0.03	+0.03
NGC 5055	7.65	-0.03	+0.04
NGC 5398	5.61	-0.06	+0.05

Continued on next column

Continued from previous column

Galaxy name	$\log(M_{\rm dust}/M_\odot)$	-dex	+dex
NGC 5408	4.43	-0.05	+0.05
NGC 5457	7.69	-0.05	+0.05
NGC 5474	6.14	-0.05	+0.05
NGC 5713	7.22	-0.04	+0.04
NGC 5866	6.61	-0.03	+0.04
NGC 6946	7.64	-0.04	+0.04
NGC 7331	7.90	-0.04	+0.04
NGC 7793	6.65	-0.05	+0.05

Concluded

APPENDIX B: GALAXY SPECIFIC PROPERTIES

To compare the dust properties and dust scaling trends of JINGLE galaxies to other local galaxy samples, we assembled data for several well-studied nearby galaxy samples (HRS, KINGFISH, HiGH and HAPLESS). We repeat the dust SED modelling procedure for each of these galaxy samples to allow for an unbiased comparison with JINGLE. The same set of IR/submm filters has been used (where possible) to infer the contribution from stellar emission (WISE 3.4 and 4.6 μm), and to fit the dust emission (WISE 12 and 22 μm, IRAS 60 μm, PACS 100 and 160 μm, and SPIRE 250, 350 and 500 μm flux). For each of these galaxy samples, galaxy properties (i.e., metallicities, star formation rates and stellar masses etc.) have been derived in a consistent way (where possible). A short description and details about the data assembly have been presented below.

B1 JINGLE

We have adopted the median $M_\star$ and SFR parameters (and uncertainties) inferred from a panchromatic SED fitting procedure using `MagPhys` (da Cunha et al. 2010). Gas-phase metallicities have been calculated using the O3N2 calibration of Pettini & Pagel (2004) based on optical strong emission lines observed in the SDSS spectra of JINGLE galaxies (Saintonge et al. 2018). Due to the lack of uncertainty measurements for some galaxy samples, we have assumed a fixed 0.05 dex uncertainty on the oxygen abundances. The HI masses and uncertainties were extracted from the ALFALFA catalog (Haynes et al. 2018). For JINGLE galaxies not covered or detected by ALFALFA, we have completed our own JINGLE HI observing campaign with Arecibo (PI: M.W.L. Smith) and have taken the HI masses and uncertainties inferred from these recent observations. Combining both datasets, we have HI masses available for 161 JINGLE galaxies. With distances ranging from 56 to 223 Mpc, it is not always easy to assign a Hubble type to each of the JINGLE galaxies. The distinction for JINGLE galaxies is therefore made only between early-type and late-type galaxies. Due the selection criteria, the JINGLE sample is dominated by late-type galaxies (186 galaxies) with a minority of 7 early-type galaxies (JINGLE 61, 63, 76, 85, 95, 104, 125).

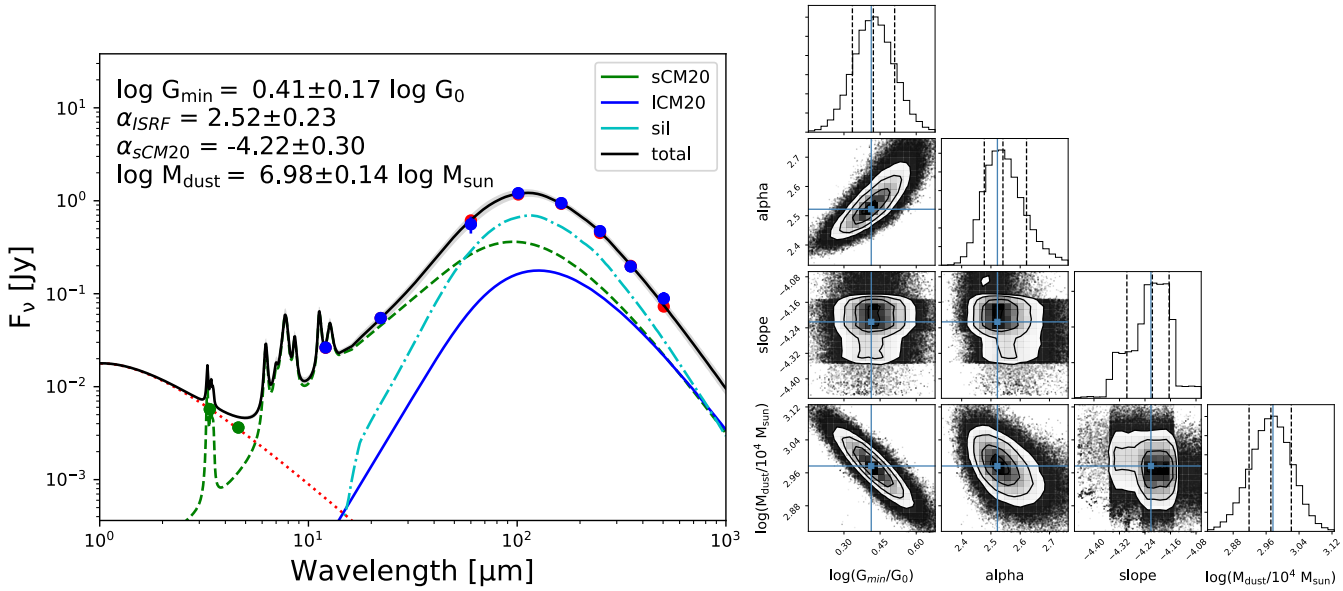

Figure A1. Left panel: a representative model fit for JINGLE 26 with our Bayesian THEMIS dust SED model. The best-fit SED models for small (sCM20) and large (lCM20) carbonaceous grains and large silicate (sil) grains are indicated with green dashed, blue solid and cyan dash-dotted lines, respectively. The stellar emission at NIR wavelengths is modelled using a blackbody function with temperature $T = 5,000K$ (red dotted curve). The total best-fit stellar+dust SED emission is shown in black. The shaded grey region indicate the lower and upper limit uncertainties on the SED models. Right panel: 1D and 2D posterior PDFs which indicate the likelihood of a given output parameter value. The blue line indicates the position of the maximum likelihood (or best-fit model) solution which does not always correspond to the peak of the posterior PDF, while the black dashed lines correspond to the 16th, 50th and 84th percentiles.

B2 Herschel Reference Survey

The *Herschel* Reference Survey (HRS, Boselli et al. 2010) is a volume-limited sample of 322[13] nearby galaxies with distances ranging from 15 Mpc to 25 Mpc, selected based on near-infrared magnitude limits of K<12 mag for late-type galaxies (Sa-Sd-Im-BCD) and K<8.7 mag for early-type galaxies (E, S0 and S0a). Due to the K-band selection criteria, the HRS is a stellar mass-selected sample dominated by more evolved sources which have already converted most of their gas into stars. It is thus not surprising that the HRS sample contains a large fraction of early-type galaxies (62), in addition to 261 late-type galaxies. Even though early-type galaxies are considered to be red and dead, nearly one quarter of the HRS ellipticals and up to 62% of HRS lenticular galaxies (S0s) have been observed to contain a non-negligible amount of dust (Smith et al. 2012).

For the HRS flux measurements and errors, we relied on the aperture-matched photometry measurements from CAAPR (Comprehensive & Adaptable Aperture Photometry Routine, Clark et al. 2018). The PACS and SPIRE observations were presented in Cortese et al. (2014) and Ciesla et al. (2012). Metal abundances (using the O3N2 calibration) have been taken from Hughes et al. (2013). We use the stellar masses and star formation rates and corresponding uncertainties inferred from `MagPhys`[14] (as presented in De Vis et al. 2017a). The HI and H_2 masses and uncertainties were taken from Boselli et al. (2014a), with HI mass measurements available for 315 HRS galaxies (of which 52 are upper limits).

B3 KINGFISH

The KINGFISH sample is composed of 61 nearby (D≤30 Mpc) galaxies with a wide range of morphological classifications (Kennicutt et al. 2011). The sample is not complete as such, but with KINGFISH galaxies covering more than four orders of magnitude in stellar mass and star formation activity, the KINGFISH galaxies stretch across most of the parameter space occupied by local galaxies. Photometric measurements and errors were taken from Dale et al. (2017), who presented an updated set of multi-wavelength photometry for all KINGFISH and SINGS galaxies. The HI and H_2 masses and uncertainties were taken from Rémy-Ruyer et al. (2014) (including three galaxies with HI upper limits and three galaxies without HI masses). Stellar masses and SFRs (and uncertainties) have been adopted from the `MagPhys` fitting results presented in Hunt et al. (2019). Oxygen abundances (based on the O3N2 calibration) have been extracted from De Vis et al. (2019), with metallicities available for 46 out of 61 KINGFISH galaxies. For the missing 15 galaxies, oxygen abundances (relying on the Kobulnicky & Kewley 2004 metallicity calibration) have been taken from Kennicutt et al. (2011), and were converted to the 03N2 calibration from Pettini & Pagel (2004)

[13] We removed HRS 228 from the sample as it was identified as a background object, rather than a nearby galaxy (Ciesla et al. 2012).

[14] `MagPhys` results are missing for four HRS galaxies (HRS 138, 150, 183, 241) due to possible contamination from an AGN, hot X-ray halo and/or synchrotron component (Eales et al. 2017).

following the conversion formula from Kewley & Ellison (2008). For two metal-poor KINGFISH galaxies (DDO 053 and DDO 165), the metal abundances reported in Kennicutt et al. (2011) were used due to the absence of a reliable conversion at these low metallicities (Kewley & Ellison 2008). To avoid any contamination from an AGN, we have removed three KINGFISH galaxies (NGC 1316, NGC 4725, NGC 4736; Rémy-Ruyer et al. 2015) from our sample.

B4 HAPLESS and HiGH samples

The HAPLESS and HiGH galaxy samples have been selected from the *Herschel* Astrophysical Terahertz Large Area Survey (H-ATLAS, Eales et al. 2010). The HAPLESS sample was selected based on bright 250 μm emission, resulting in a local sample of 42 dusty galaxies at distances between 15 and 46 Mpc. The selection criteria and galaxy properties have been outlined in Clark et al. (2015); they show that HAPLESS galaxies are predominantly blue, star-forming galaxies in an early stage of evolution. HiGH galaxies were selected based on their HI detections. The 40 HI-rich galaxies span distances from 11.3 to 158.9 Mpc, and typically have low stellar masses ($\leq 10^9$ M$_\odot$) and relatively low dust masses for their stellar mass content, indicating that these galaxies are also at an early stage of evolution. Due to similarities in the selection criteria, it is not surprising that the dust-selected HAPLESS and HI-selected HiGH galaxy samples have 22 galaxies in common.

Photometry measurements and errors for HAPLESS and HiGH samples have been derived using the CAAPR software from Clark et al. (2018), and the `MagPhys` fitting results (for stellar masses and SFRs) and HI masses (and uncertainties) were taken from Clark et al. (2015) and De Vis et al. (2017a), respectively. HI mass measurements were available for all HiGH galaxies, and 38/42 HAPLESS galaxies. Metal abundances were taken from De Vis et al. (2017b).

APPENDIX C: ESTIMATING STAR FORMATION HISTORIES

A reasonable estimation of a galaxy's SFH is vital to constrain stellar dust production and supernova rates. To avoid biasing the inferred SFHs by assuming a particular SFH shape, we resort to non-parametric star formation histories, where we determine the average SFR in three "look-back time" bins: 0-10 Myr, 10-100 Myr and 100 Myr-12 Gyr, and where we have assumed that galaxies started forming stars roughly 12 Gyr ago. To determine the average SFR during those three distinct periods, we assembled Hα, WISE 22 μm, FUV, and TIR luminosities, and inferred two different measurements of the recent star formation activity: SFR(Hα+WISE 22 μm) and SFR(FUV+TIR)[15] (see Table C1 for the estimated SFRs). With Hα and WISE 22 μm emission being mostly sensitive to young stellar populations with ages $\lesssim$10 Myr, while FUV and TIR probe star formation on recent timescales of $\sim$100 Myr (e.g., Kennicutt & Evans 2012), the ratio of these SFR estimates, SFR(Hα+WISE 22 μm)/SFR(FUV+TIR), provides an indication of how much star formation occurred during the last 10 Myr as opposed to a longer 100 Myr look-back time period. For each sample of galaxies at a similar evolutionary stage, as indicated by the ratio of their HI gas mass versus stellar mass, $M_{\rm HI}/M_\star$, we have calculated the average ratio of these SFRs. These ratios, in comparison to the average stellar mass and SFR (which corresponds to a constant SFR over the last 100 Myr as inferred by `MagPhys`), allow us to constrain the average SFR during the last 10 and 100 Myr. The average (constant) SFR during the 100 Myr-12 Gyr period is then constrained based on the current "average" stellar mass for each galaxy bin.

Figure C1 shows the SFHs that have been inferred in this way for the six $M_{\rm HI}/M_\star$ bins. For comparison, the delayed SFH model used by De Vis et al. (2017b) is indicated with a red, solid line and was used in Models II to test the sensitivity of our model results to the assumed SFH. Galaxies at an early stage of evolution (Bin 1) did experience some star formation in the past, but have converted gas into stars at an increased rate during the last 100 Myr, with a further increment in their star formation activity during the last 10 Myr. Similar SFHs were inferred for the two subsequent bins (Bins 2 and 3), but show less pronounced differences in their average SFRs during the three subsequent epochs. More evolved galaxies (Bins 4-5) show a dip in their star formation activity over 100 Myr timescales, followed by an increased star formation activity during the last 10 Myr. The most evolved galaxies (Bin 6) show an overall decrease in their star formation activity during the last 100 Myr, which can be expected if most gas has been consumed in earlier star formation episodes (or has been partly removed from the galaxy).

We realise that these SFHs will not be representative for all galaxies presented in this paper. However, the star formation activity during the last 10 and 100 Myr, and how this relates to any earlier star formation activity in the galaxy, will be important to assess how much dust has formed over a galaxy lifetime. The non-parametric SFHs for the six galaxy bins have been overlaid on the star formation main sequence (see Figure C2). All model SFH tracks display a horizontal trend in the $M_\star$-SFR plane, due to the fixed SFR at look-back times older than 100 Myr, and reside on the SF main sequence during most of a galaxy's lifetime. Only for look-back times >11 Gyr, the model SFH tracks are positioned above the SF main sequence inferred for the local Universe, which is consistent with the expected shift of the main sequence at earlier times (Santini et al. 2017).

APPENDIX D: DUST AND ELEMENT EVOLUTION MODELS: DEUS

We here describe the evolution of stars, metals and dust, as it is implemented in DEUS. We have adopted the same notation as commonly used throughout the literature (e.g., Rowlands et al. 2014; De Vis et al. 2017b).

[15] We have used the prescriptions from Kennicutt & Evans (2012), and have assumed that the WISE 22 μm filter is equivalent to the MIPS 24 μm or IRAS 25 μm filter.

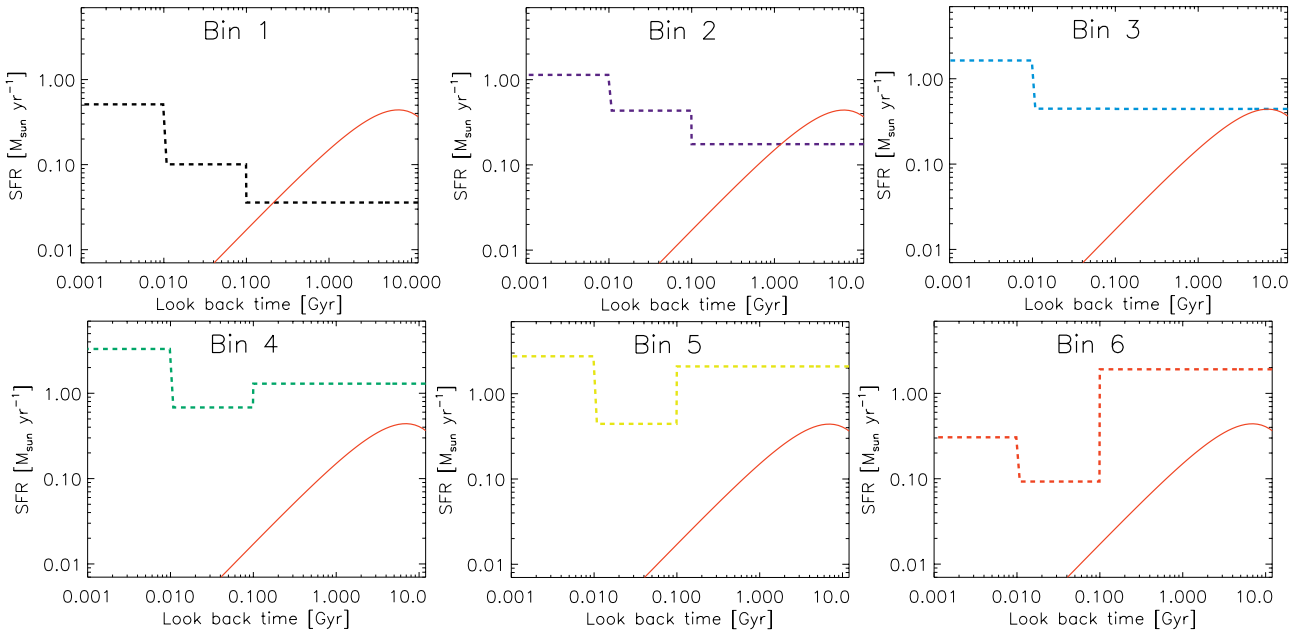

Figure C1. The customised star formation histories that have been inferred for each of the galaxy subsamples following the method presented in Appendix C, and were used in our Model I. Galaxies evolve from Bin 1 (corresponding to an early stage of evolution as inferred from the high $M_{\rm HI}/M_\star$ ratios) through to Bin 6 (characteristic of evolved galaxies with low $M_{\rm HI}/M_\star$ ratios). The customised SFHs are compared to the delayed star formation history (red curve) applied by De Vis et al. (2017b), which has been used to predict galaxy's dust, HI and metal content in our Model II.

Table C1. We present the log $M_{\rm HI}/M_\star$ range and sample size in each galaxy bin, along with the subsample size with available Hα, FUV, WISE 22 and TIR measurements which were used to estimate the past (>100 Myr), recent (10-100 Myr) and present (0-10 Myr) SFRs inferred for each of the six galaxy bins.

Bin	log $M_{\rm HI}/M_\star$ range	$N_{\rm galaxies}$	$N_{\rm SFR}$	$SFR_{>100{\rm Myr}}$ [M$_\odot$ yr^{-1}]	$SFR_{10\text{-}100{\rm Myr}}$ [M$_\odot$ yr^{-1}]	$SFR_{<10{\rm Myr}}$ [M$_\odot$ yr^{-1}]
1	[0.5,-]	17	3	0.04	0.10	0.51
2	[0,0.5[	81	31	0.18	0.43	1.14
3	[-0.5,0[	134	47	0.44	0.45	1.64
4	[-1.0,-0.5[	132	62	1.30	0.68	3.30
5	[-1.5,-1.0[	46	20	2.09	0.44	2.75
6	[-,-1.5[	13	2	1.91	0.09	0.31

D1 Model implementation

D1.1 Stellar populations

The stellar mass of a galaxy, $M_\star$, evolves with time according to:

$$\frac{dM_\star}{dt} = \psi(t) - e(t) \quad \text{(D1)}$$

where $\psi(t)$ is the SFR and $e(t)$ is the ejected mass lost from stars throughout their lives. We assume the mass loss occurs at the end of stellar evolution:

$$e(t) = \int_{m_{\tau_{\rm m}}}^{m_{\rm max}} [m - m_{\rm R}(m)]\psi(t-\tau_{\rm m})\phi(m)dm, \quad \text{(D2)}$$

where the integral runs over stars with masses ($m_{\tau_{\rm m}}$) with a lifetime $\tau_{\rm m}$, which formed at a time $t - \tau_{\rm m}$. The ejected masses are calculated as the difference between the initial stellar mass, m, and the remnant mass, $m_{\rm R}(m)$ for a star with a given initial mass m. The stellar lifetimes are adopted from Schaller et al. (1992), while the remnant masses are taken from Prantzos et al. (1993). We assume a Chabrier (2003) initial mass function $\phi(m)$, maximum stellar mass $m_{\rm max}$ of 100 M$_\odot$, with the masses of stars ranging from 0.1 to 100 M$_\odot$ in stellar mass bins of 0.1 M$_\odot$.

D1.2 Gaseous reservoirs

The total (interstellar) gas content of a galaxy, $M_{\rm gas}$, evolves as:

$$\frac{dM_{\rm gas}}{dt} = -\psi(t) + e(t) + I(t) - O(t), \quad \text{(D3)}$$

where the first term accounts for the gas lost through "astration", as the gas is being consumed to form new stars at a rate equal to the SFR, ψ(t). The second term accounts for the mass gain through mass loss during late stellar evolutionary phases, while the third and fourth term represent the infall and outflow of gas. For Models I and II, we have assumed closed-box models with no infalling or outflowing gas (i.e., $I(t) = 0$ and $O(t) = 0$). In Model III, we abandoned this closed-box assumption (see Section D3) and have explored how the DEUS parameters are affected by the in- and outflow of gas. Our current picture of galaxy evolution suggests that relatively pristine gas is being funneled through cold

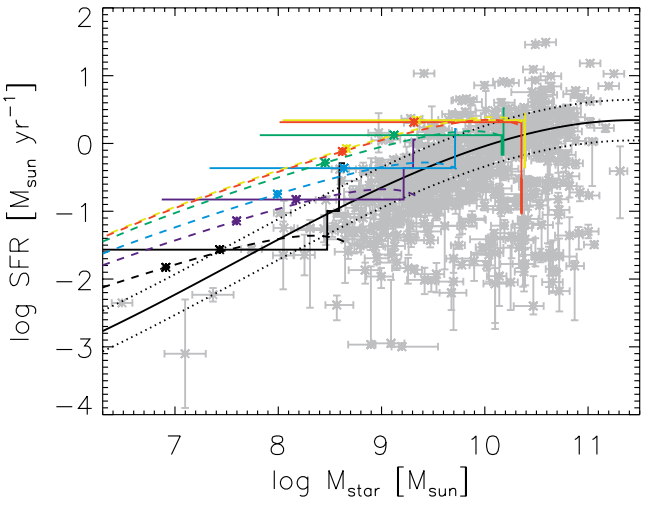

Figure C2. The star formation main sequence for JINGLE, HRS, KINGFISH, HAPLESS and HiGH galaxies (grey symbols), with the average trend found by Saintonge et al. (2016) overlaid as a solid black line. An offset of 0.3 dex on either side of this trend (similar to the spread observed by Noeske et al. 2007; Pannella et al. 2009; Rodighiero et al. 2010) has been indicated by dashed black lines, and encloses galaxies located on the SF main sequence. The evolutionary path for the customised and delayed SFHs have been overlaid with solid and dashed curves, respectively, for galaxy Bins 1 through to 6 in black, purple, blue, green, yellow and red. The location of the asterisk corresponds to a look-back time of 2 Gyr.

gas streams and is slowly accreted from the halo onto the galaxy disk during its lifetime (e.g., Dekel et al. 2009). Neglecting this process, which works to dilute metal fractions in the interstellar medium, will accelerate the buildup of a galaxy's metal content over time. Due to poor constraints on the initial gas mass and metallicity of the halo from which a galaxy forms, it is quite tedious to constrain the rates of infalling and outflowing gas, and their mass loading factors (as they will be influenced by the initial gas and metal abundances) based on the observations at hand. To work around this problem, we leave the initial gas mass of the halo as a free parameter in DEUS and infer what gas mass is needed to reproduce the observed present-day specific HI gas masses ($M_{\rm gas}/M_\star$) and oxygen abundances. In this manner, the initial gas mass will be adapted to account for any gas mass accreted/lost throughout a galaxy's lifetime. Naturally, this approach will only work for galaxies that have not experienced any recent gas in- or outflows, as those would affect their dust and gas masses on timescales significantly shorter than the time needed to replenish a galaxy's dust and gas content. In this paper, we therefore refrain from modelling the sub-population of HI-deficient HRS galaxies which have experienced massive gas outflows that have shut down star formation on galaxy-wide scales in these systems over the last $\lesssim$1.5 Gyr (e.g., Boselli et al. 2006; Pappalardo et al. 2010; Ciesla et al. 2016).

Rather than total gas masses, we only have HI gas mass measurements available for most galaxies in our local galaxy sample. The determination of molecular gas masses for JINGLE galaxies has been deferred to JINGLE Paper III for a subsample of JINGLE galaxies, and to future work, in anticipation of the completion of our JCMT CO(2-1) survey. Molecular gas mass estimates exist for a few nearby galaxy samples (e.g., HRS, KINGFISH), but these measurements are either hampered by the extrapolation of localized CO observations to galaxy-wide scales, or by the uncertainties involved in the conversion from CO-to-H_2 masses, which varies non-linearly with the metallicity and ISM phase filling factors in galaxies (e.g., Schruba et al. 2012; Amorín et al. 2016; Accurso et al. 2017, Madden et al. in prep.).

To compare the total gas masses in our model to the observed HI content, which are related through:

$$M_{\rm gas} \;=\; \xi\;(M_{\rm HI} + M_{\rm H_2}), \tag{D4}$$

we need to estimate the correction factor (ξ) to take into account the gas fraction of elements heavier than hydrogen. Rather than a canonical correction factor of 1.36, often used in the literature, we follow Clark et al. (2016) to define the correction factor ξ as:

$$\xi \;=\; \frac{1}{1-\left(f_{\rm He_p} \;+\; f_{\rm Z}\left[\frac{\Delta f_{\rm He}}{\Delta f_{\rm Z}}\right]\right) - f_{\rm Z}} \tag{D5}$$

which depends on the primordial helium mass fraction ($f_{\rm He_p}$=0.2485±0.0002, Aver et al. 2013), the metal mass fraction $f_{\rm Z}$ of the galaxy at that point in time, and the evolution of the helium mass fraction with metallicity, $\left[\frac{\Delta f_{\rm He}}{\Delta f_{\rm Z}}\right]$, which is assumed to be equal to $\left[\frac{\Delta f_{\rm He}}{\Delta f_{\rm Z}}\right]$=1.41±0.62 (Balser 2006). The metal mass fraction is defined as $f_{\rm Z} = f_{\rm Z_\odot} Z_{\rm O}$ with the Solar metal mass fraction assumed to be $f_{\rm Z_\odot}$=0.0134 (Asplund et al. 2009). The oxygen-based metallicity $Z_{\rm O}$ is defined as:

$$Z_{\rm O} = \delta_{\rm O} \left[\frac{O}{H}\right] / \left[\frac{O}{H}\right]_\odot \tag{D6}$$

with the Solar oxygen abundance [12+log $\frac{O}{H}$]=8.69±0.05 (Asplund et al. 2009), and a correction factor $\delta_{\rm O}$ (=1.32±0.09, Mesa-Delgado et al. 2009) to account for the depletion of oxygen (mostly in HII regions).

In addition to this ξ correction factor, we need to correct our model gas masses for a contribution from molecular gas, to allow a direct comparison with the observed HI masses. Hereto, we rely on the scaling relation of the H_2-to-HI mass ratio as a function of the stellar mass inferred by Popping et al. (2014) for disc-dominated galaxies using metallicity-based H_2 formation recipes in their semi-analytic models of galaxy evolution. Their modelled scaling laws agree well with various literature sets of observed data from Leroy et al. (2008), Saintonge et al. (2011) and Boselli et al. (2014b), and are applicable up to redshifts of z$\sim$2.

D1.3 Metal budgets

The mass of metals in the ISM ($M_{\rm metals}$(gas)) evolves with time according to:

$$\frac{dM_{\rm metals}(gas)}{dt} \;=\; -Z_{\rm M}(t)\psi(t) + e_{\rm Z}(t) + Z_{\rm I}I(t) - Z_{\rm O}O(t) \tag{D7}$$

where $Z_{\rm M}(t)$ represents the mass fraction of heavy elements in the gas phase (i.e., $Z_{\rm M} = M_{\rm metals}({\rm gas})/M_{\rm gas}$). $e_{\rm Z}$ accounts

for the ejected metals through stellar mass loss during late stellar evolutionary stages, and can be calculated as:

$$e_{\rm Z}(t) = \int_{m_{\tau_{\rm m}}}^{m_{\rm max}} \left(\left[m - m_{\rm R(}{}_{m)} \right] Z(t-\tau_{\rm m}) + m p_{\rm Z} \right) \times \psi(t-\tau_{\rm m}) \phi(m) dm \quad \text{(D8)}$$

where the first term between parentheses accounts for the metals ejected through stellar mass loss (based on the metallicity of the gas from which the star formed t - $\tau_{\rm m}$ ago), and the second term ($mp_{\rm Z}(m)$) represents the heavy elements produced by a star with initial mass m and metallicity Z (where $p_{\rm Z}(m)$ represents the stellar yields). The metal yields for low- and intermediate mass stars (LIMS, with progenitor masses $M_{\rm prog} \leq 8\,{\rm M}_{\odot}$) and for massive stars ($8\,{\rm M}_{\odot} < M_{\rm prog} \leq 40{\rm M}_{\odot}$) were taken from van den Hoek & Groenewegen (1997) and Woosley & Weaver (1995), respectively. The third and fourth term of Eq. D7, which are related to gas inflows and outflows, are not considered in our closed-box Models I and II.

Rather than tracking metal fractions, our observations constrain the oxygen abundances in galaxies. To convert these oxygen abundances into metal mass fractions, we rely on the conversion from Solar oxygen abundance ($12+\log({\rm O/H})_{\odot}=8.69$) to the Solar metal fraction ($f_{Z_{\odot}}=0.134$), which results in the following relation[16]: $f_{\rm Z} = 27.36 \times 10^{(12+\log(O/H))-12}$. Note that this relation has been inferred based on the conversion from total metal fraction to oxygen abundance at solar metallicity, but that the exact conversion at other metallicities likely deviates from this relation due to oxygen abundance variations. At the onset of our simulation, we have assumed a metallicity $Z_{\rm ini}=M_Z/M_{\rm gas}=0.0001$[17], and an oxygen mass $M_{\rm O}=0.44\times M_Z$.

D1.4 Dust reservoirs

The dust mass evolves with time according to:

$$\frac{dM_{\rm dust}}{dt} = \int_{m_{\tau_{\rm m}}}^{m_{\rm max}} ([m - m_{\rm R}(m)] Z(t-\tau_{\rm m}) \delta_{\rm LIMS} + m p_{\rm Z} \delta_{\rm dust}) \times \psi(t-\tau_{\rm m}) \phi(m) dm - (M_{\rm dust}/M_{\rm gas}) \psi(t) - M_{\rm dust} \delta_{\rm destr}(t) + M_{\rm dust} \delta_{\rm grow}(t) + (M_{\rm dust}/M_{\rm gas})_{\rm I} I(t) - (M_{\rm dust}/M_{\rm gas})_{\rm O} O(t) \quad \text{(D9)}$$

where the first term accounts for dust production by LIMS (during late stellar evolutionary stages) and massive stars (after their explosion as core-collapse supernovae). The second and third term account for dust destruction through astration (i.e., dust that is incorporated into new stars) and dust destruction (mostly) through supernova shocks in the interstellar medium. The fourth term accounts for dust grown through accretion of elements onto pre-existing grain seeds in interstellar clouds. The last two terms have been neglected for closed-box Models I and II, while dust outflows (no dust inflows) have been accounted for in Model III (see App. D3).

We rely on the model dust yields, $\delta_{\rm dust}$, from Ferrarotti & Gail (2006) for LIMS and from Marassi et al. (2019) (for their non-rotating CE models[18]) for supernovae to model stellar dust production[19]. The supernova dust yields from Marassi et al. (2019) are at the high end of values reported in the literature, and have not yet been corrected for the destruction of freshly condensed supernova dust by a reverse shock. There is a large uncertainty inherent to the efficiency of reverse shock dust destruction, due to its dependence on the grain size and composition, the clumpiness of the dust distribution in the supernova ejecta, and the reverse shock velocity (which is set by the ambient circum- and interstellar densities). Values have been quoted ranging from a few percent to 100% dust destruction efficiencies (e.g., Bianchi & Schneider 2007; Silvia et al. 2010; Bocchio et al. 2016; Kirchschlager et al. 2019). Rather than fixing the survival fraction of supernova dust for destruction by the reverse shock, we implement the reverse shock dust destruction efficiency as a free parameter ($f_{\rm survival}$) of our model. We furthermore assume that stars more massive than $40\,{\rm M}_{\odot}$ will end up as black holes, and do not contribute to the dust enrichment of the ISM.

To model the dust destruction efficiency, $\delta_{\rm destr}$, we infer an estimate for the average dust destruction timescale τ_{destr}, which describes the destruction of dust with time through $M_{\rm dust}(t) = M_{\rm dust}(0)\exp(-t/\tau_{\rm destr})$ and which is assumed to be the inverse of the dust destruction efficiency, i.e., $\delta_{\rm destr}=\tau_{destr}^{-1}$. We define the dust destruction timescale as:

$$\tau_{\rm destr} = \frac{M_{\rm gas}}{\delta_{\rm SN} R_{\rm SN} M_{\rm cl}} \quad \text{(D10)}$$

where $R_{\rm SN}$ is the supernova rate per gas mass, $M_{\rm gas}$, and per 20 Myr (i.e., the time interval in our chemical evolution model), which can be inferred from the star formation history and the number of massive stars with progenitor masses between 8 and $40\,{\rm M}_{\odot}$ that have reached the end of their lives during the last 20 Myr period. The average gas mass cleared by each supernova, $M_{\rm cl}$, (which is a free parameter in our models) depends on the supernova energy, and the structure, clumpiness and density of the ambient interstellar medium (Slavin et al. 2015; Hu et al. 2019). The gas mass cleared of dust, $M_{\rm cl}$, is thought to vary from $1000\,{\rm M}_{\odot}$ under average warm neutral medium conditions ($n_{\rm H}$ $\sim$0.1 cm^3) to $700\,{\rm M}_{\odot}$ for the cold neutral medium ($n_{\rm H}$ $\sim$10 cm^3) up to $\lesssim 350\,{\rm M}_{\odot}$ in molecular clouds with $n_{\rm H}$ >100 cm^3 (Hu et al. 2019). The correction factor $\delta_{\rm SN}$ accounts for "delayed" or "clustered" supernova explosions occurring above the galactic plane and within superbubbles, where they will neglect

[16] This conversion factor translates into an oxygen mass fraction, compared to the total mass of metals, of 44%, if we first convert the oxygen abundance into oxygen mass fractions through $X_{\rm O} = 12\frac{O}{H}$. The latter value corresponds to the lower limit of predictions between 45-60% from Garnett (2002).

[17] We verified that assuming an absence of any metals at the start of our simulation renders similar results.

[18] The "CE" models from Marassi et al. (2019) correspond to a set of models for which the properties of the explosions have been calibrated to reproduce empirically inferred values of the ^{56}Ni mass, as opposed to their "FE" models for which a fixed explosion energy is assumed.

[19] We have interpolated between the yields for evolved stars and supernovae to infer dust yields for progenitor masses between 7 and $13\,{\rm M}_{\odot}$.

to destroy a significant mass of pre-existing dust. We fix $\delta_{\rm SN}$ to 0.4, estimated from simulations with a random positional occurrence of supernova (Hu et al. 2019), and consistent with earlier estimates (0.36, McKee 1989).

The efficiency of grain growth processes $\delta_{\rm grow}(=\tau_{\rm grow}^{-1})$ is estimated from the average grain growth timescale:

$$\tau_{\rm grow} = \frac{M_{\rm gas}}{\epsilon Z_{\rm M} \psi} \left(1 - \frac{\eta_{\rm dust}}{Z_{\rm M}}\right)^{-1} \quad \text{(D11)}$$

following Mattsson et al. (2012); Mattsson & Andersen (2012) (see Section D2 for a quick summary of their derivation of the grain growth parameter), where $Z_{\rm M}$ $(=M_{\rm metals}({\rm gas})/M_{\rm gas})$ represents the metallicity (in the gas phase), ψ corresponds to the star formation rate and $\eta_{\rm dust}$ is the dust-to-gas ratio. The ϵ parameter determines the grain growth parameter, and is set as a free parameter in our model.

D2 Grain growth parameter

In this paragraph, we reiterate the derivation of the grain growth prescription presented by Mattsson et al. (2012) to illustrate the assumptions that have gone into the derivation of Eq. D11 and to give a physical interpretation of the grain growth parameter ϵ.

The rate (per unit volume) at which the number of atoms, $N_{\rm A}$, increases in dust grains through accretion of metals on to these dust grains can be expressed as:

$$\frac{{\rm d}N_{\rm A}}{{\rm d}t} = f_{\rm s}\, \pi a^2\, n_{\rm Z}\, n_{\rm gr}\, \langle v_{\rm gas} \rangle \quad \text{(D12)}$$

where $f_{\rm s}$ is the sticking coefficient (which gives the probability that an atom will stick to a grain), a is the typical grain radius, and $n_{\rm Z}$ and $n_{\rm gr}$ are the average number densities for atomic metals and dust grains, respectively, while $\langle v_{\rm gas} \rangle$ is the mean thermal speed of the gas particles. Rather than number densities, this expression can be rewritten in terms of dust surface densities ($\Sigma_{\rm dust}$) of molecular gas clouds, i.e.:

$$\frac{{\rm d}\Sigma_{\rm dust}}{{\rm d}t} = \frac{f_{\rm s}\, \pi a^2\, \widetilde{\Sigma}_{\rm Z}\, \Sigma_{dust}\, \langle v_{\rm gas} \rangle}{\langle m_{\rm gr} \rangle\, d_{\rm c}} \quad \text{(D13)}$$

where $\widetilde{\Sigma}_{\rm Z}$ is the surface density of free (atomic) metals, $\langle m_{\rm gr} \rangle$ is the mean mass of interstellar dust grains, and $d_{\rm c}$ is the size of the molecular cloud. The inferred grain growth timescale can then be written as:

$$\tau_{\rm gr} = \tau_0 \left(1 - \frac{\eta_{\rm dust}}{Z_{\rm M}}\right)^{-1} \quad \text{(D14)}$$

with

$$\tau_0 = \frac{\langle m_{\rm gr} \rangle\, d_{\rm c}}{f_{\rm s}\, \pi a^2\, \widetilde{\Sigma}_{\rm Z}\, \langle v_{\rm gas} \rangle} \approx \frac{\langle m_{\rm gr} \rangle\, d_{\rm c}}{f_{\rm s}\, \pi a^2\, Z_{\rm M}\, \Sigma_{\rm mol}\, \langle v_{\rm gas} \rangle} \quad \text{(D15)}$$

where $\Sigma_{\rm mol}$ is the molecular gas surface density and $Z_{\rm M}$ the metallicity. It is assumed that $\Sigma_{\rm mol} \approx \Sigma_{\rm H_2}$, and that the star formation rate surface density scales with $\Sigma_{\rm H_2}$ (where α is a constant):

$$\Sigma_{\rm SFR} = \alpha\, \Sigma_{\rm H_2} \quad \text{(D16)}$$

through the Kennicutt-Schmidt relation (Schmidt 1959; Kennicutt 1998) for molecular (rather than total) gas mass surface densities (e.g., Bigiel et al. 2008). The mean thermal speed $\langle v_{\rm gas} \rangle$ is furthermore assumed to be roughly constant, and the typical grain radius a is assumed not to vary much, which allows to reduce Eq. D15 to:

$$\tau_0^{-1} = \frac{\epsilon\, Z_{\rm M}\, \Sigma_{\rm SFR}}{\Sigma_{\rm gas}} \quad \text{(D17)}$$

which only depends on the metallicity $Z_{\rm M}$, the gas ($\Sigma_{\rm gas}$) and star formation rate ($\Sigma_{\rm SFR}$) surface densities, with a constant (dimensionless) factor ϵ that is left as a free parameter. This factor ϵ will set the grain growth efficiency and will be sensitive to the average grain size, the mean thermal speed of gas particles, and other assumptions that have gone into this derivation. As we do not consider the resolved nature of galaxies in this work, we convert the surface densities from Eq. D17 to total gas mass and SFR measurements in Eq. D11.

The derivation of this grain growth prescription from Mattsson et al. (2012) is based on the assumption that the accretion rate of gas-phase elements onto grain surfaces scales with the molecular cloud surface density, and does not account for any barriers which could reduce the grain growth efficiency (e.g., ice mantle formation, or Coulomb barriers). Due to the molecular gas mass not always being readily available from observations or simulations, the star formation rate (assumed to scale with the molecular gas content) is used to parameterise the efficiency of grain growth processes.

D3 Including gas infall and outflows

It is commonly believed that the infall from primordial gas along dense filaments from the cosmic web plays an important role in fueling and sustaining star formation in galaxies (e.g. Dekel et al. 2009; Silk & Mamon 2012). This gas accretion of metal-poor gas is also required to explain the fundamental relation between the stellar mass, metallicity and star formation rate of galaxies (e.g., Sánchez Almeida et al. 2014). For this work, we assume that gas infall scales directly with the star formation rate, and that the gas is pristine and dust-free (i.e., the infalling gas does not contribute to the overall metal and dust budget in galaxies).

Multi-phase galactic outflows, on the other hand, have been shown to play an important role in the quenching of star formation activity, but the main driving force of these outflows (supernovae, stellar wind, accreting black holes, cosmic rays) has yet to be identified (see Naab & Ostriker 2017 for a recent review). Other than simulations, the copious number of detections of massive galactic outflows (e.g., Cicone et al. 2014; Walter et al. 2017; Fluetsch et al. 2019) during recent years has reinforced the importance of these outflows in regulating galaxy evolution. Galactic outflows are thought to be most powerful in galaxies at high redshift which undergo strong bursts of star formation; while low redshift galaxies with $M_\star \gtrsim 10^{10}\,{\rm M}_\odot$ tend to have a suppressed galactic outflows due to the lower gas fraction and turbulent velocity dispersion in these galaxies, which makes it tenuous to drive outflows with high mass loading factors (Hayward & Hopkins 2017). The mass loading factor η $(=\dot{M}_{\rm out}/\dot{M}_\star)$ is defined as the ratio of the mass outflow rate to the star formation rate. To quantify how the mass loading factor varies across a galaxy's lifetime, we rely on the prescription from Hayward & Hopkins (2017) (see their Eq. 44) which relates

η to the stellar mass $M_\star$ and gas fraction $f_{\rm gas}$ of galaxies through:

$$\eta \; = \; 14 \left(\frac{f_{\rm gas} M_\star}{10^{10} M_\odot} \right)^{-0.23} \exp \left(\frac{-0.75}{f_{\rm gas}} \right) \tag{D18}$$

and accounts for the decreased mass loading factors in the local Universe. The prescriptions from Hayward & Hopkins (2017) furthermore agree well with the mass-loading factors inferred from the FIRE simulations (Muratov et al. 2015).

APPENDIX E: TABLES

Table E1: Overview of the results obtained from performing Mann-Whitney U-tests to verify whether two samples have the same median of distribution. The output nearly-normal test statistic Z (top value) and probability level p (bottom value) of this test are presented for each pair of galaxy samples. Probabilities p>0.05 (shown in blue) indicate that the hypothesis that both samples have the same median of distribution could not be rejected, and that both samples are therefore not significantly different.

Properties		JINGLE vs. HRS	JINGLE vs. KINGFISH	JINGLE vs. HAPLESS	JINGLE vs. HiGH	HRS vs. KINGFISH	HRS vs. HAPLESS	HRS vs. HiGH	KINGFISH vs. HAPLESS	KINGFISH vs. HiGH	HAPLESS vs. HiGH
$\log M_\star$	Z =	-6.1	-2.7	-4.1	-3.2	0.3	-3.0	-1.0	-1.9	-0.4	1.8
	p =	$< 10^{-6}$	3.4×10^{-3}	1.8×10^{-5}	7.3×10^{-4}	4.0×10^{-1}	1.5×10^{-3}	1.7×10^{-1}	2.7×10^{-2}	3.5×10^{-1}	3.7×10^{-2}
$\log \mathrm{SFR}$	Z =	-12.7	-5.3	-5.4	-2.8	1.8	-1.5	4.2	-1.9	1.8	4.0
	p =	$< 10^{-6}$	$< 10^{-6}$	$< 10^{-6}$	2.5×10^{-3}	3.7×10^{-2}	6.3×10^{-2}	1.2×10^{-5}	3.1×10^{-2}	3.8×10^{-2}	3.8×10^{-5}
$\log \mathrm{sSFR}$	Z =	-5.9	-0.7	-0.1	2.2	2.7	1.6	4.5	0.2	2.1	1.3
	p =	$< 10^{-6}$	2.4×10^{-1}	4.6×10^{-1}	1.6×10^{-2}	3.0×10^{-3}	5.8×10^{-2}	$< 10^{-6}$	4.2×10^{-1}	1.9×10^{-2}	1.0×10^{-1}
$\log M_{\mathrm{HI}}$	Z =	-8.8	-3.2	-3.6	1.3	2.2	-1.6	6.3	-2.4	3.8	4.4
	p =	$< 10^{-6}$	6.1×10^{-4}	1.7×10^{-4}	9.7×10^{-2}	1.3×10^{-2}	5.1×10^{-2}	0.0	9.3×10^{-3}	7.9×10^{-5}	5.8×10^{-6}
12+log(O/H)	Z =	-13.6	-2.4	-4.5	-5.7	6.9	0.5	2.0	-3.0	-3.0	1.0
	p =	$< 10^{-6}$	9.3×10^{-3}	3.3×10^{-6}	0.0	0.0	3.0×10^{-1}	2.2×10^{-2}	1.5×10^{-3}	1.3×10^{-3}	1.6×10^{-1}
$\log M_{\mathrm{dust}}/M_\star$	Z =	-7.5	-3.6	-2.1	-0.6	0.9	0.2	2.9	-0.3	2.0	1.5
	p =	$< 10^{-6}$	1.5×10^{-4}	1.9×10^{-2}	2.6×10^{-1}	1.9×10^{-1}	4.1×10^{-1}	2.1×10^{-3}	4.0×10^{-1}	2.2×10^{-2}	6.8×10^{-2}
$\log M_{\mathrm{HI}}/M_\star$	Z =	-3.1	0.9	0.2	4.5	2.7	0.6	5.8	-0.5	3.0	2.4
	p =	10^{-3}	1.8×10^{-1}	4.4×10^{-1}	2.7×10^{-6}	3.7×10^{-3}	2.7×10^{-1}	0.0	3.2×10^{-1}	1.5×10^{-3}	9.4×10^{-3}
$\log M_{\mathrm{dust}}/M_{\mathrm{metals}}$	Z =	5.4	-1.1	-0.3	-2.6	-5.9	-2.4	-4.9	0.2	-1.5	-1.3
	p =	0.0	1.4×10^{-1}	3.8×10^{-1}	4.9×10^{-3}	0.0	7.6×10^{-3}	$< 10^{-6}$	4.2×10^{-1}	6.4×10^{-2}	9.9×10^{-2}
$\log M_{\mathrm{dust}}/M_{\mathrm{HI}}$	Z =	-0.4	-2.4	-1.9	-5.7	-2.2	-1.3	-5.6	-0.2	-2.9	-1.3
	p =	3.5×10^{-1}	9.3×10^{-3}	2.7×10^{-2}	0.0	1.4×10^{-2}	9.2×10^{-2}	0.0	4.4×10^{-1}	2.1×10^{-3}	9.4×10^{-2}

APPENDIX F: LIST OF ACRONYMS AND SYMBOLS

APPENDIX G: FIGURES

This paper has been typeset from a TEX/LATEX file prepared by the author.

Table F1. We collected the acronyms used throughout this paper in this summary table for quick reference.

Symbol	Explanation
AGB	asymptotic giant branch
DEUS	Dust and Element evolUtion modelS
FUV	far-ultraviolet
HAPLESS	*Herschel*-ATLAS Phase-1 Limited-Extent Spatial Survey
HI def	HI deficiency
HIGH	HI-selected Galaxies in *Herschel*-ATLAS
HRS	*Herschel* Reference Survey
IMF	initial mass function
IR	infrared
ISM	interstellar medium
JINGLE	JCMT dust and gas In Nearby Galaxies Legacy Exploration
KINGFISH	Key Insights on Nearby Galaxies: A Far-Infrared Survey with *Herschel*
LIMS	low-and intermediate mass stars
MCMC	Markov Chain Monte Carlo
PDF	probability density function
PP04	metallicity calibration from Pettini & Pagel (2004)
SED	spectral energy distribution
SFH	star formation history
SFR	star formation rate
sSFR	specific star formation rate
THEMIS	The Heterogeneous dust Evolution Model for Interstellar Solids
TIR	total infrared
UV	ultraviolet

Table F2. We collected the symbols used throughout this paper in this summary table for quick reference.

Symbol	Explanation
12+log(O/H)	oxygen abundance (as proxy of metallicity)
D	distance
DTM	dust-to-metal ratio
$\delta_{\rm destr}$	dust destruction efficiency
$\delta_{\rm grow}$	grain growth efficiency
$\delta_{\rm LIMS}$	dust yields for low- and intermediate mass stars (LIMS)
$\delta_{\rm dust}$	dust yields for supernovae
$\delta_{\rm SN}$	correction factor to account for "clustered" or "delayed" supernova explosions (which will not clear interstellar material)
$e(t)$	mass loss (at time t) during late stellar evolutionary stages
ϵ	grain growth parameter – DEUS parameter
$f_{\rm c}$	cold gas fraction
$f_{\rm gas}$	gas fraction (i.e., $M_{\rm gas}/(M_{\rm gas}+M_\star)$)
$f_{\rm survival}$	fraction [in %] of freshly condensed supernova dust capable of surviving the reverse shock – DEUS parameter
$f_{\rm Z}$	metal mass fraction
η	mass loading factor (= ratio of the mass outflow rate to the star formation rate)
$\eta_{\rm dust}$	dust-to-gas ratio
$I(t)$	infalling gas at time t
$lcm20$	large hydrocarbon grains (in the THEMIS dust model)
$m_{\rm R}$	remnant mass for a star with initial mass m
$\rm M_\odot$	solar mass
$M_{\rm gas,ini}$	initial gas mass (in $\rm M_\odot$) – DEUS parameter
$M_{\rm cl}$	interstellar cleared mass (in $\rm M_\odot$) per single supernova event – DEUS parameter
$M_{\rm gas}$	total (interstellar) gas mass, i.e. $\xi(M_{\rm HI}+M_{\rm H_2})$
$M_{\rm HI}$	atomic gas mass
$M_{\rm H_2}$	molecular gas mass
$M_{\rm metals}$(gas)	metal mass in the gas phase
$M_{\rm metals}$(gas+dust)	metal mass in the gas phase + locked in dust grains
$M_{\rm prog}$	progenitor mass (where progenitor refers to the star prior to the supernova event)
$M_\star$	stellar mass
$M_{\rm HI}/M_\star$	specific HI gas mass
$M_{\rm dust}/M_\star$	specific dust mass
$n_{\rm H}$	hydrogen density
$N_{\rm burn}$	MCMC steps in the warm-up phase
$N_{\rm chain}$	the length of the MCMC chain
$N_{\rm eff}$	effective sample size, defined as $N_{\rm chain}/\tau_{\rm int}$
ξ	correction factor to account for gas fraction heavier than hydrogen
$O(t)$	outflowing gas at time t
$p_{\rm Z}(m)$	stellar yields for a star with initial mass m and metallicity Z
p	probability (significance) level (both for Spearman rank correlation and Mann-Whitney U-tests)
ρ	Spearman rank correlation coefficient
$sCM20$	small hydrocarbon grains (in the THEMIS dust model)
σ	standard deviation
$\Sigma_{\rm dust}$	dust mass surface density
$\Sigma_{\rm gas}$	gas mass surface density
$\Sigma_{\rm SFR}$	SFR surface density
sil	silicates (in the THEMIS dust model)
$R_{\rm SN}$	supernova rate per gas mass, $M_{\rm gas}$
$T_{\rm dust}$	dust temperature
$\tau_{\rm destr}$	dust destruction timescale ($=\delta_{\rm destr}^{-1}$)
$\tau_{\rm int}$	integrated auto-correlation time of the MCMC chain
$\tau_{\rm grow}$	grain growth timescale ($=\delta_{\rm grow}^{-1}$)
$\tau_{\rm m}$	lifetime of a star with initial mass m
$\phi_{\rm m}$	initial mass function (IMF)
χ^2	chi-squared statistic
$\chi^2_{\rm red}$	reduced chi-squared statistic
$\psi(t)$	star formation rate (SFR) at time t
$X_{\rm CO}$	CO-to-H_2 conversion factor
$Z_{\rm I}$	metallicity of infalling gas
$Z_{\rm M}$	metallicity ($=M_{\rm metals}$(gas)$/M_{\rm gas}$)
$Z_{\rm O}$	metallicity of outflowing gas

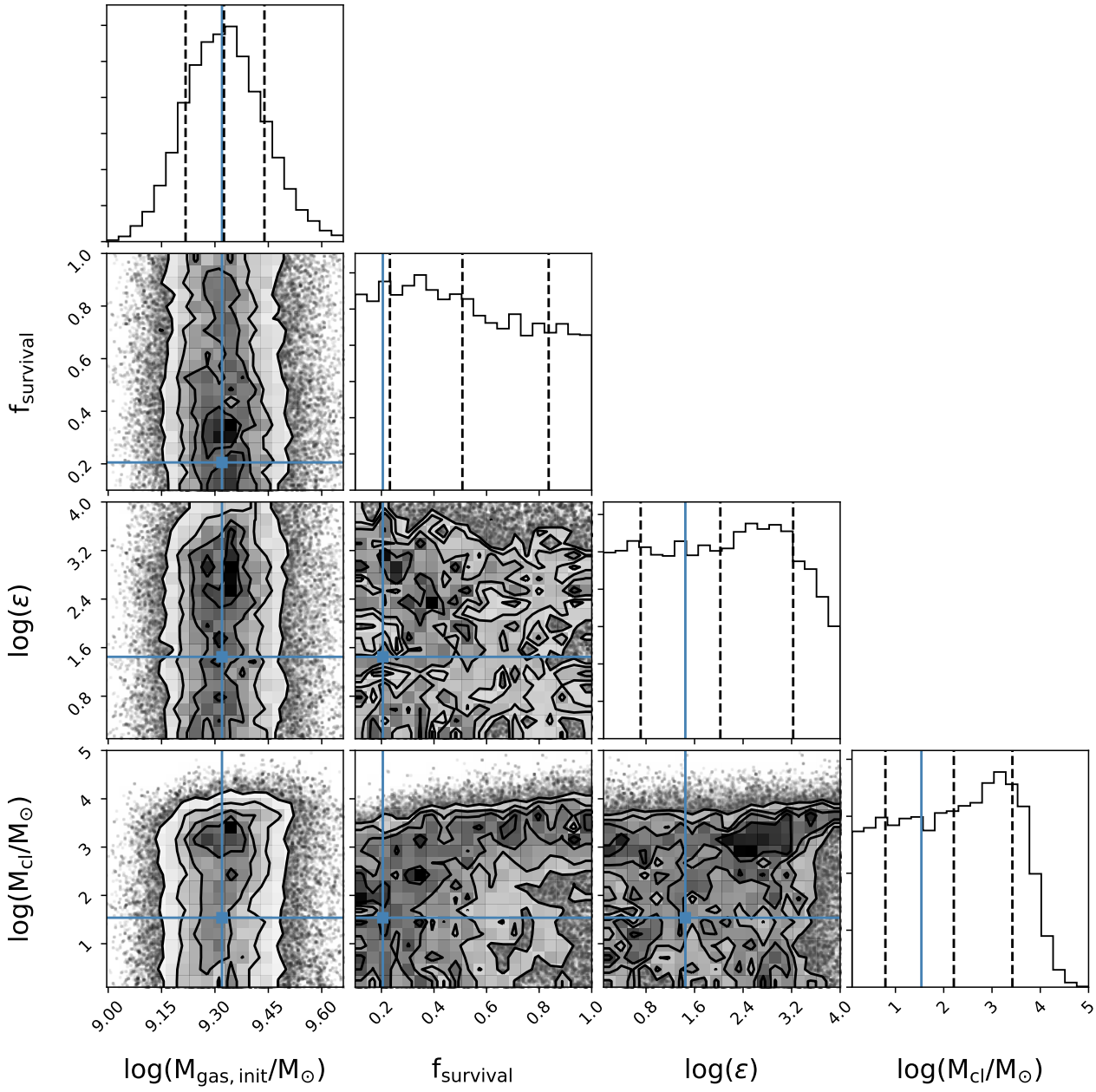

Figure G1. Corner plot for Model I (i.e., closed-box models with a customised SFH) for galaxy bin 1. The contour plots correspond to 2D posterior PDFs indicating the probability of two parameters in a 2D plane, where contours represent the 0.5σ, 1.0σ, 1.5σ and 2.0σ likelihoods. The histograms correspond to 1D marginalised posterior PDFs showing the likelihood that a certain value will be assigned to a given parameter (by marginalising over the other parameters). The maximum likelihood (blue solid curve) corresponds to the best-fit solution. The black dashed lines correspond to the 16th, 50th and 84th percentiles of the 1D posterior PDFs to reflect the uncertainties on these median model parameter values.

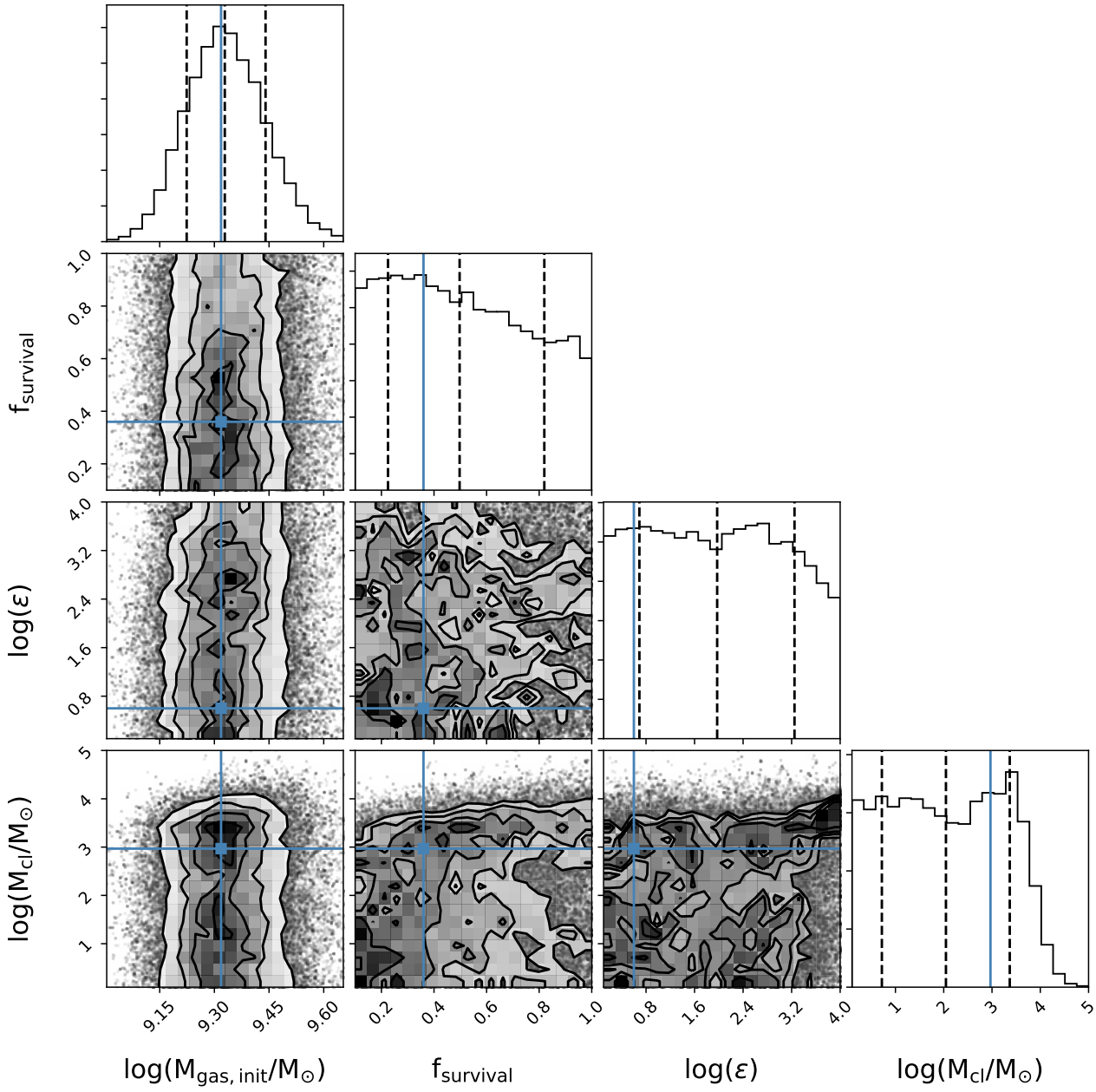

Figure G2. Corner plot for Model II (i.e., closed-box models with a delayed SFH) for galaxy bin 1. See caption of Fig. G1 for more information.

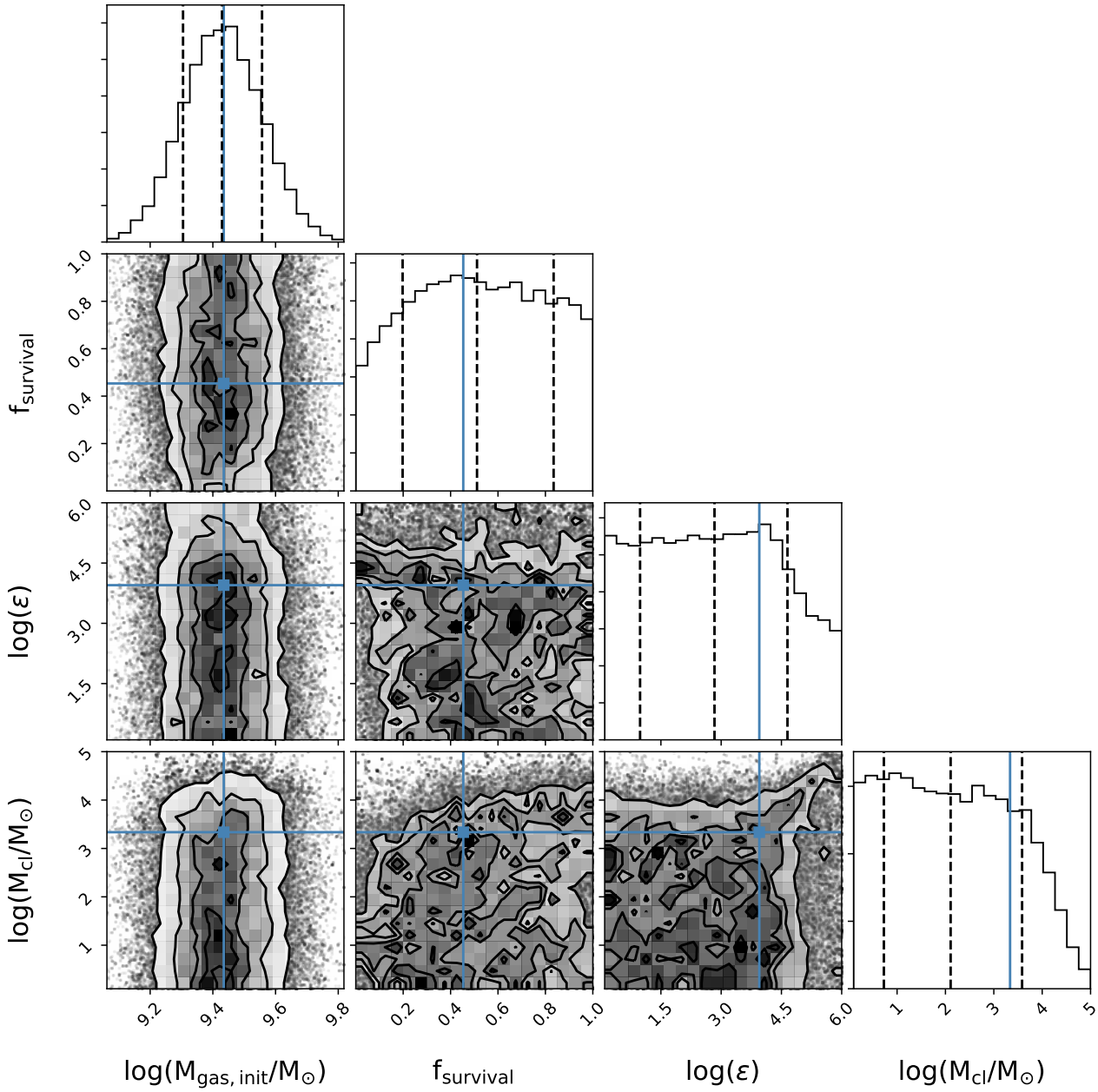

Figure G3. Corner plot for Model III (i.e., models with gaseous flows and a customised SFH) for galaxy bin 1. See caption of Fig. G1 for more information.

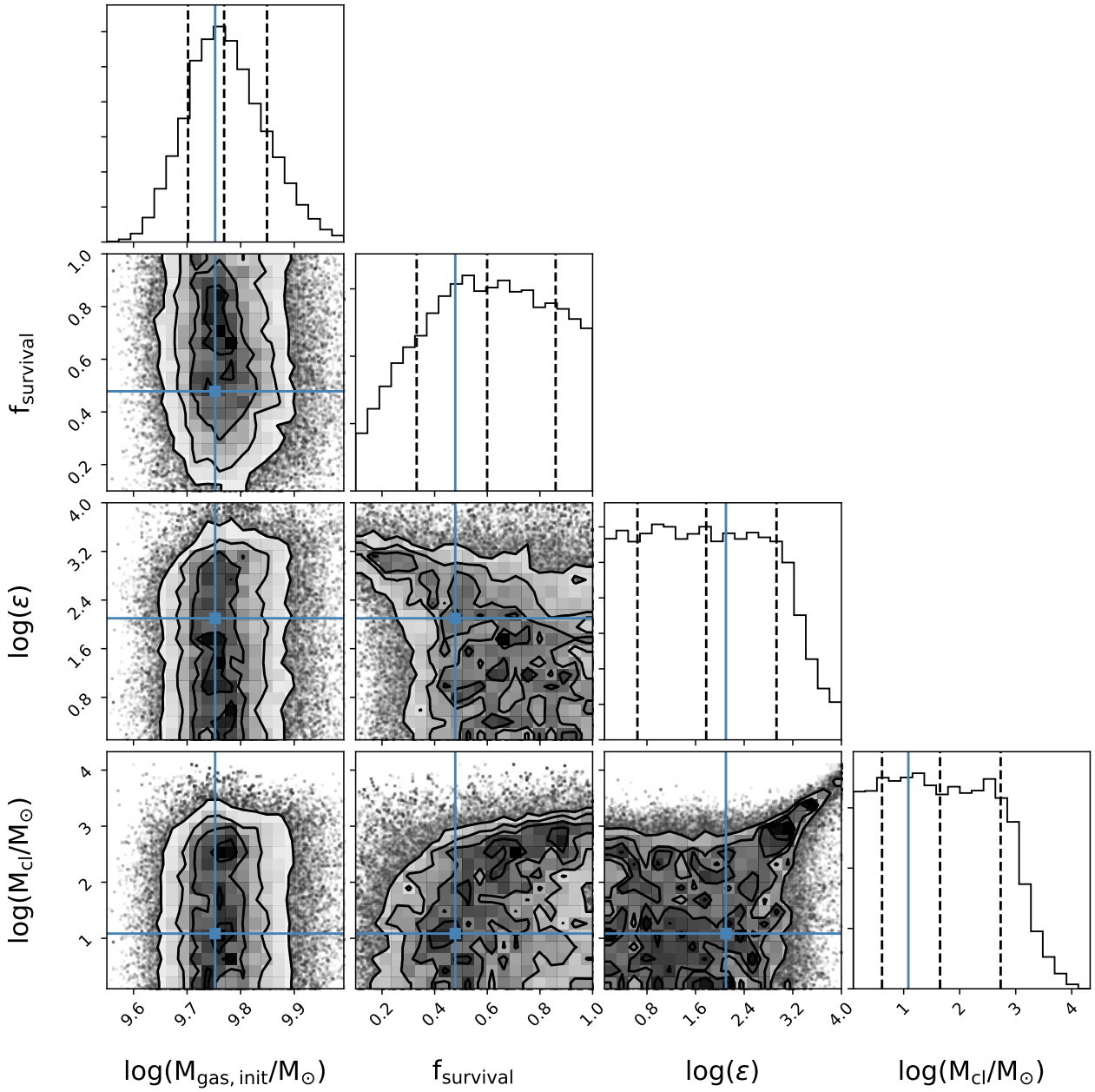

Figure G4. Corner plot for Model I (i.e., closed-box models with a customised SFH) for galaxy bin 2. See caption of Fig. G1 for more information.

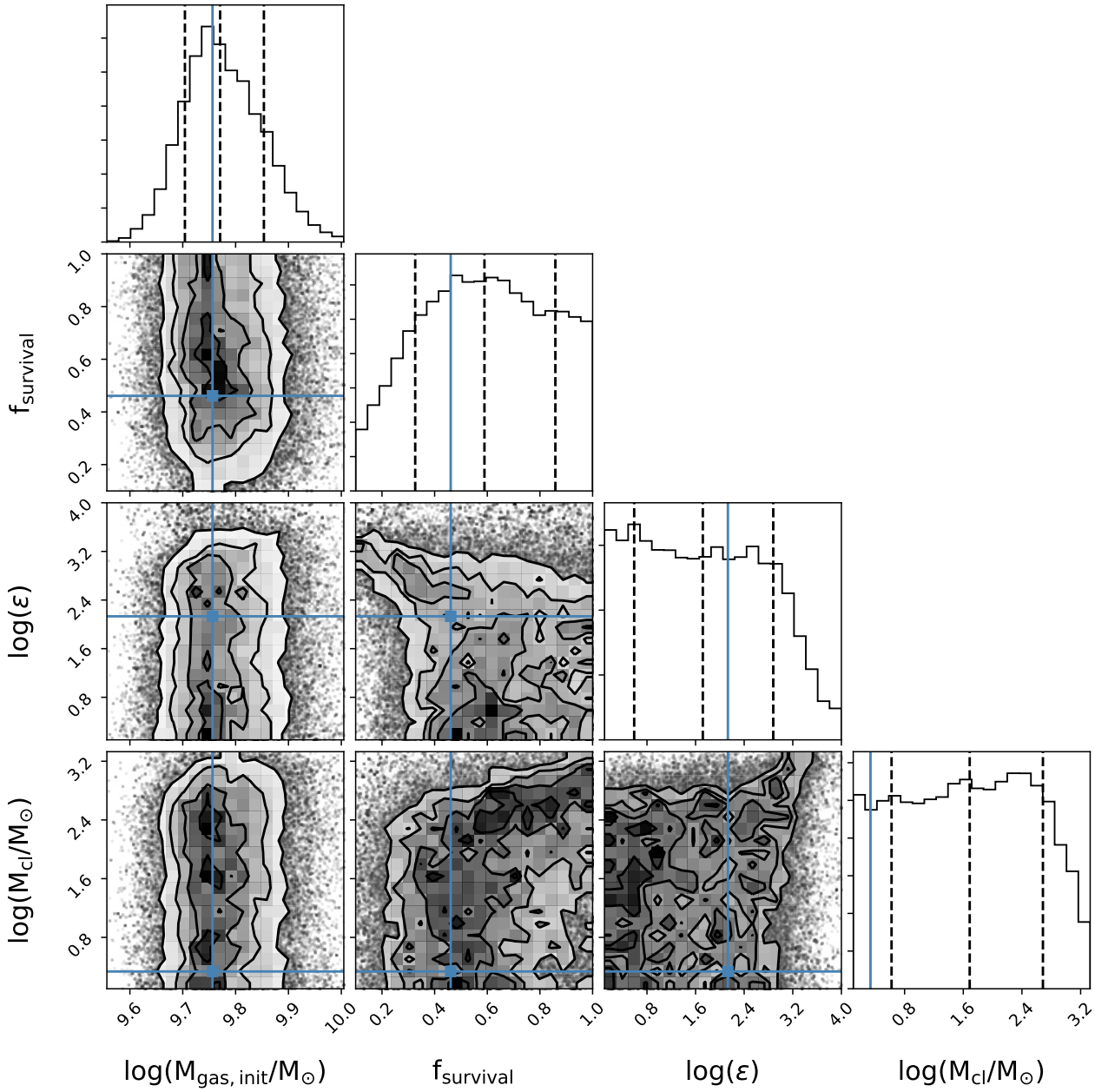

Figure G5. Corner plot for Model II (i.e., closed-box models with a delayed SFH) for galaxy bin 2. See caption of Fig. G1 for more information.

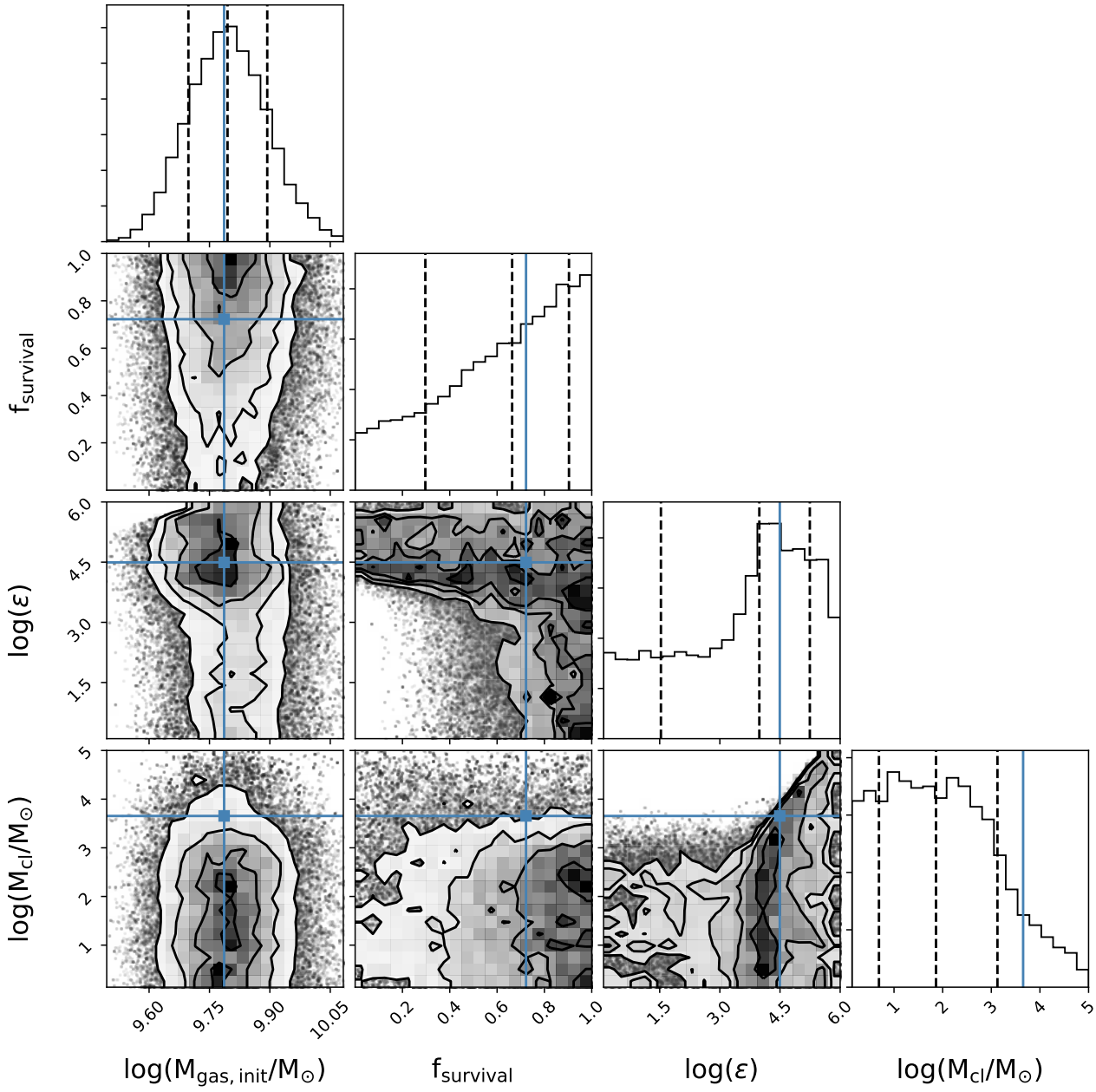

Figure G6. Corner plot for Model III (i.e., models with gaseous flows and a customised SFH) for galaxy bin 2. See caption of Fig. G1 for more information.

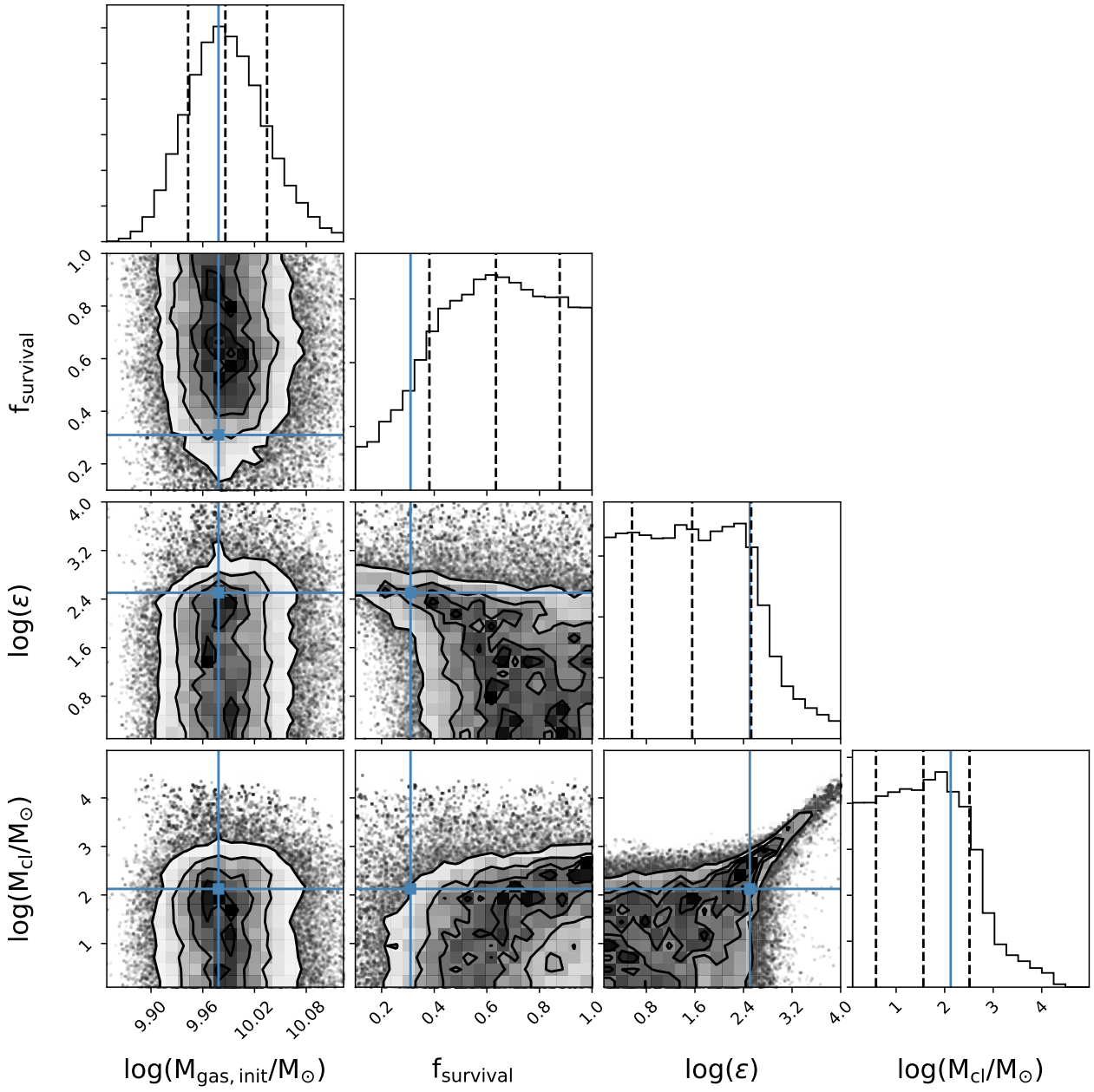

Figure G7. Corner plot for Model I (i.e., closed-box models with a customised SFH) for galaxy bin 3. See caption of Fig. G1 for more information.

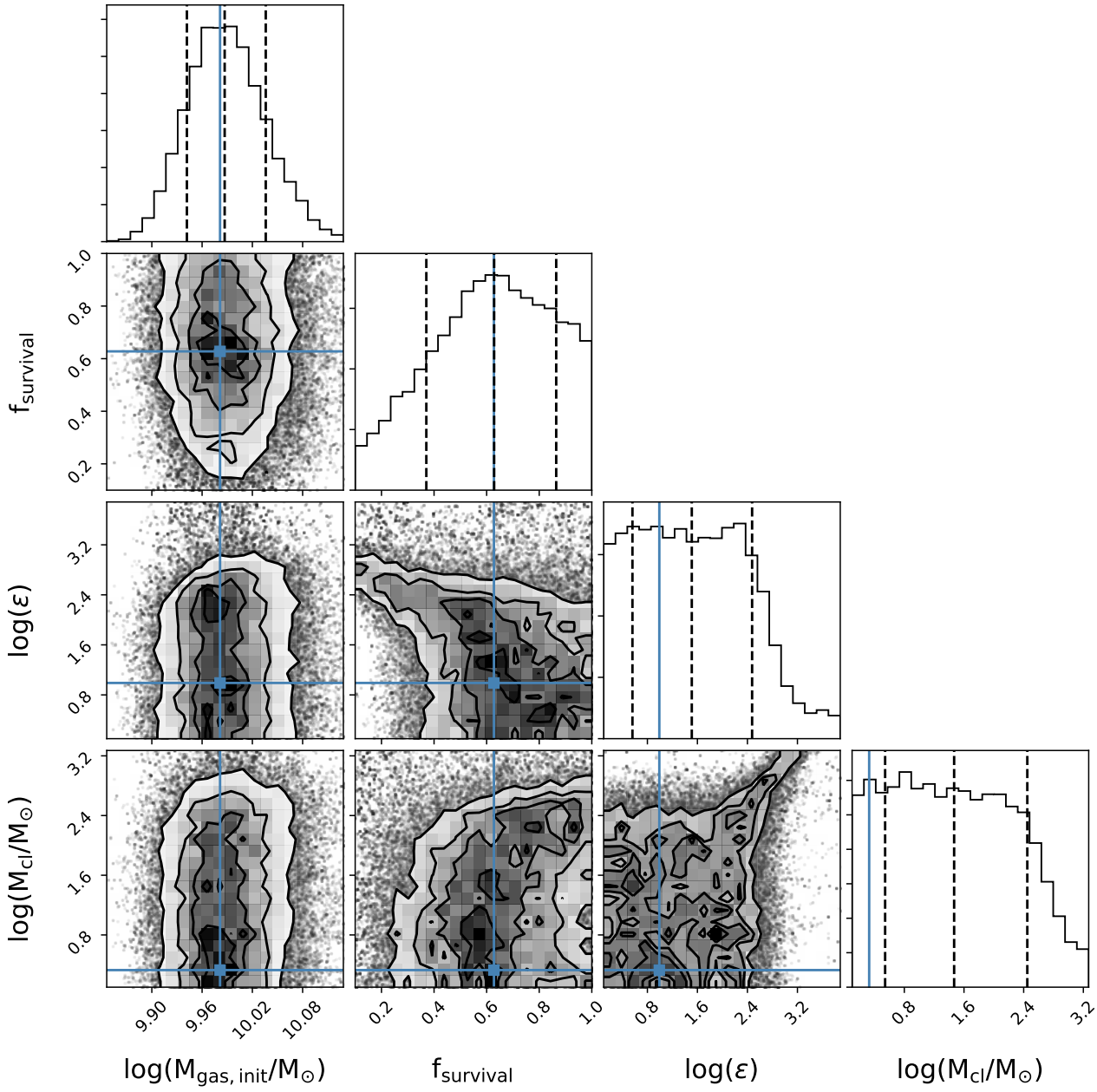

Figure G8. Corner plot for Model II (i.e., closed-box models with a delayed SFH) for galaxy bin 3. See caption of Fig. G1 for more information.

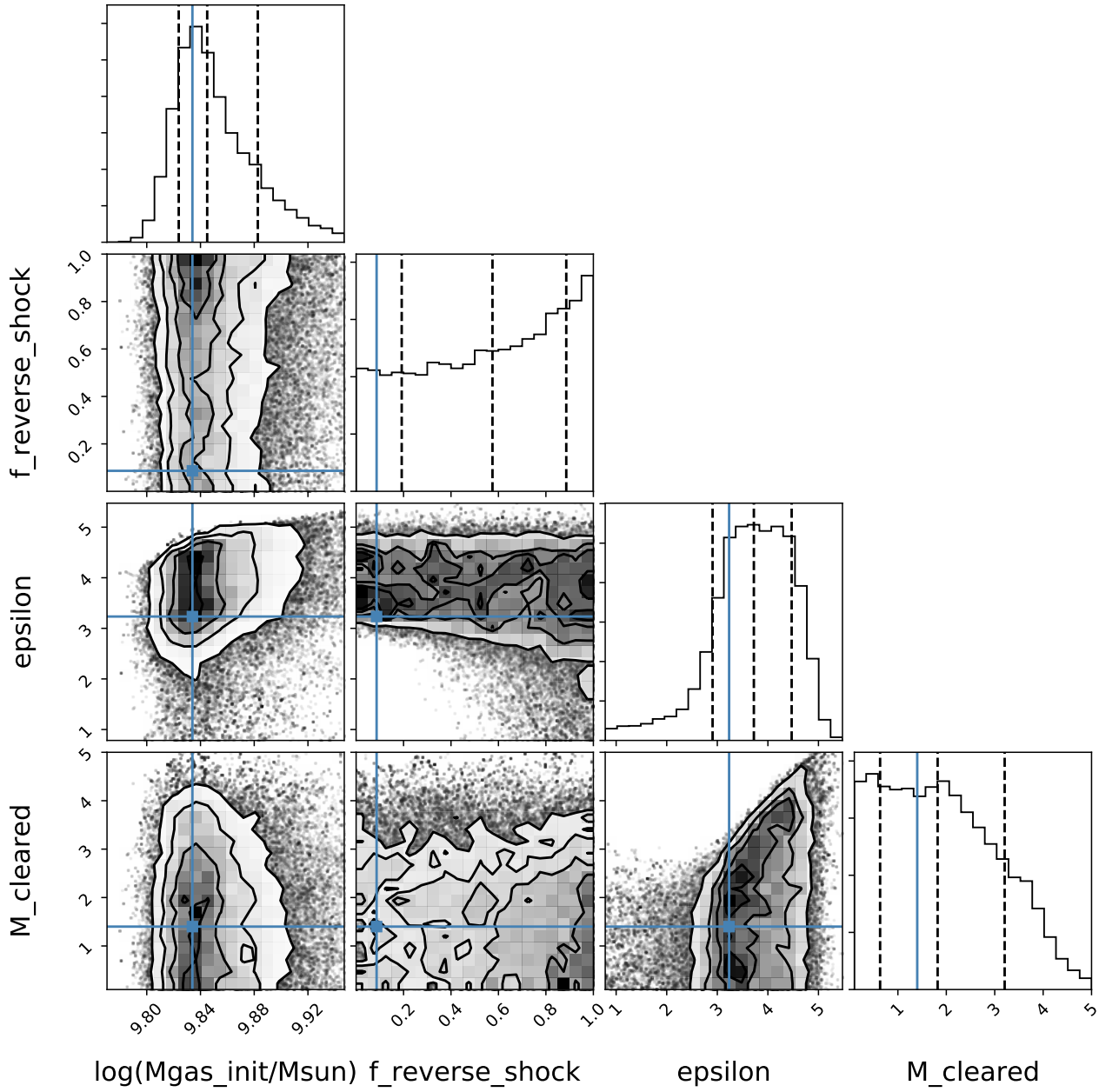

Figure G9. Corner plot for Model III (i.e., models with gaseous flows and a customised SFH) for galaxy bin 3. See caption of Fig. G1 for more information.

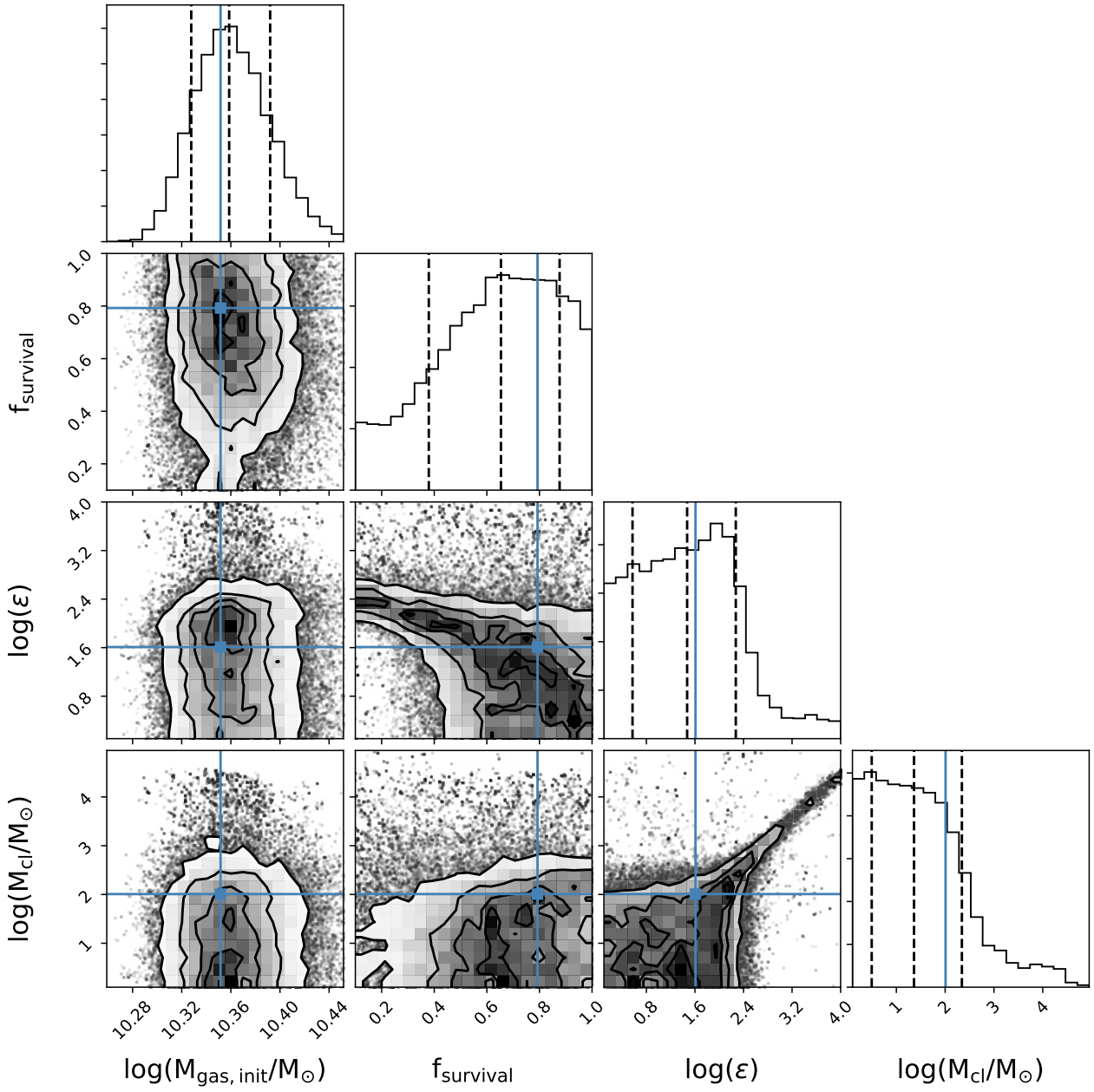

Figure G10. Corner plot for Model I (i.e., closed-box models with a customised SFH) for galaxy bin 4. See caption of Fig. G1 for more information.

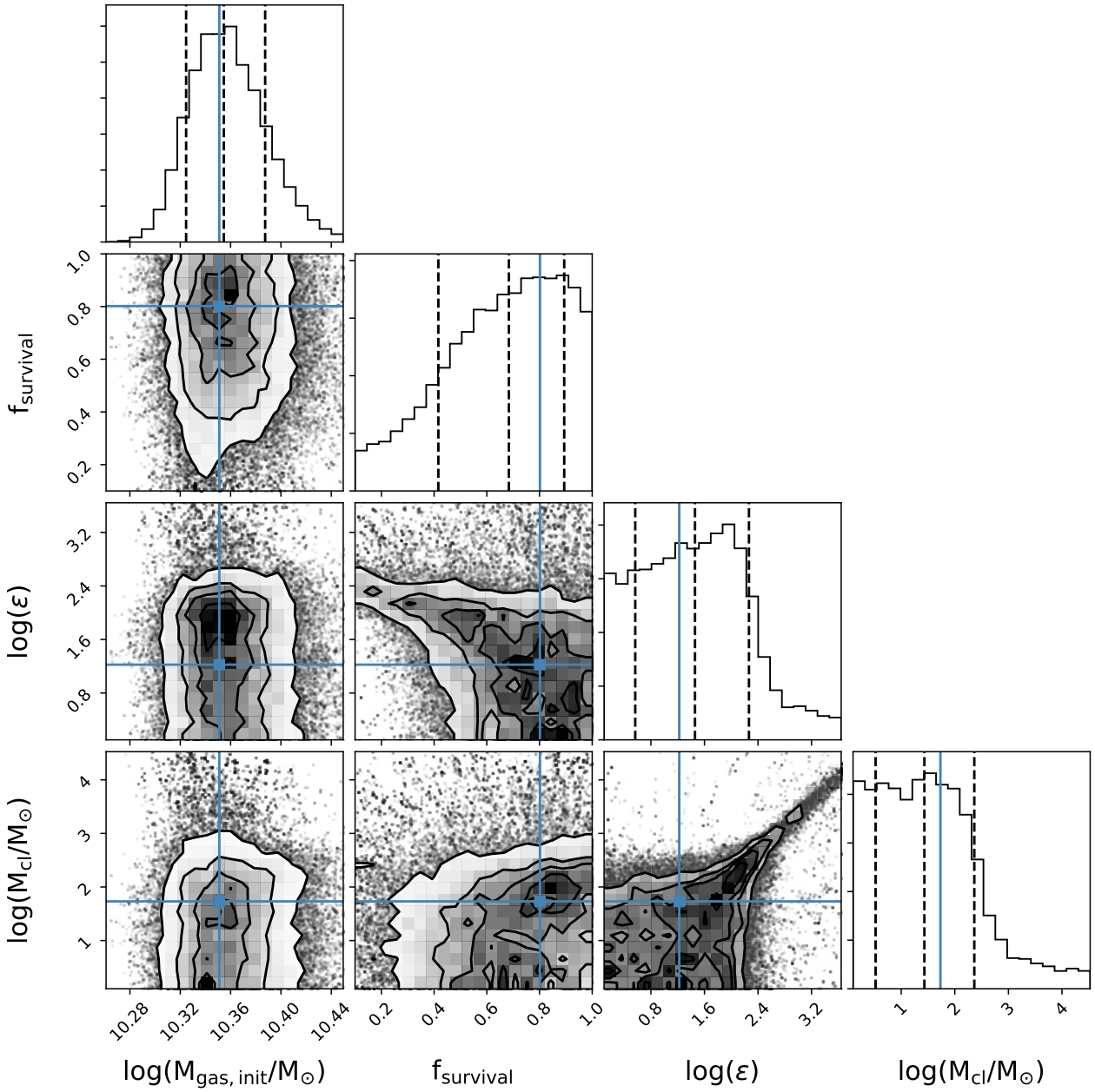

Figure G11. Corner plot for Model II (i.e., closed-box models with a delayed SFH) for galaxy bin 4. See caption of Fig. G1 for more information.

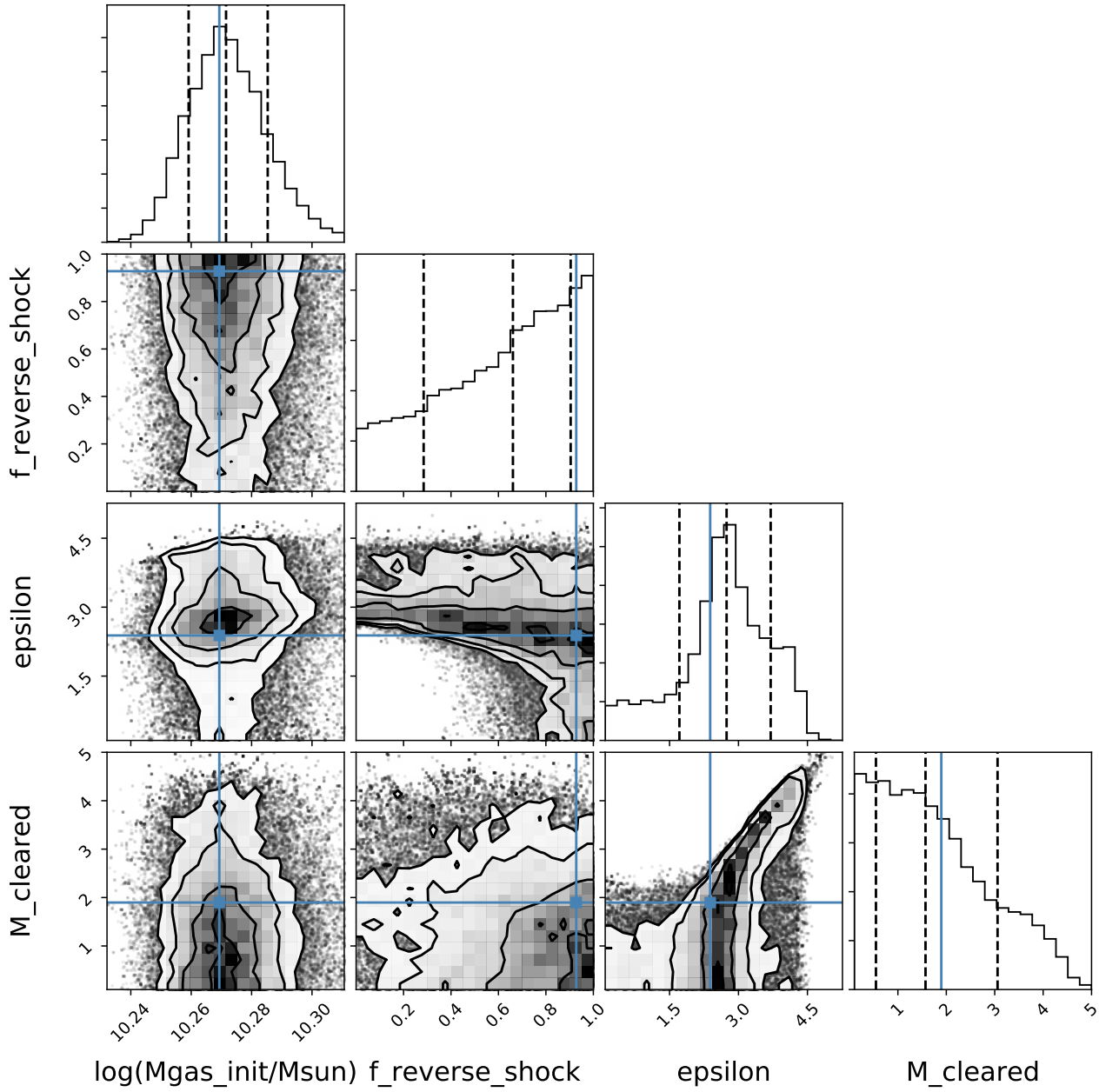

Figure G12. Corner plot for Model III (i.e., models with gaseous flows and a customised SFH) for galaxy bin 4. See caption of Fig. G1 for more information.

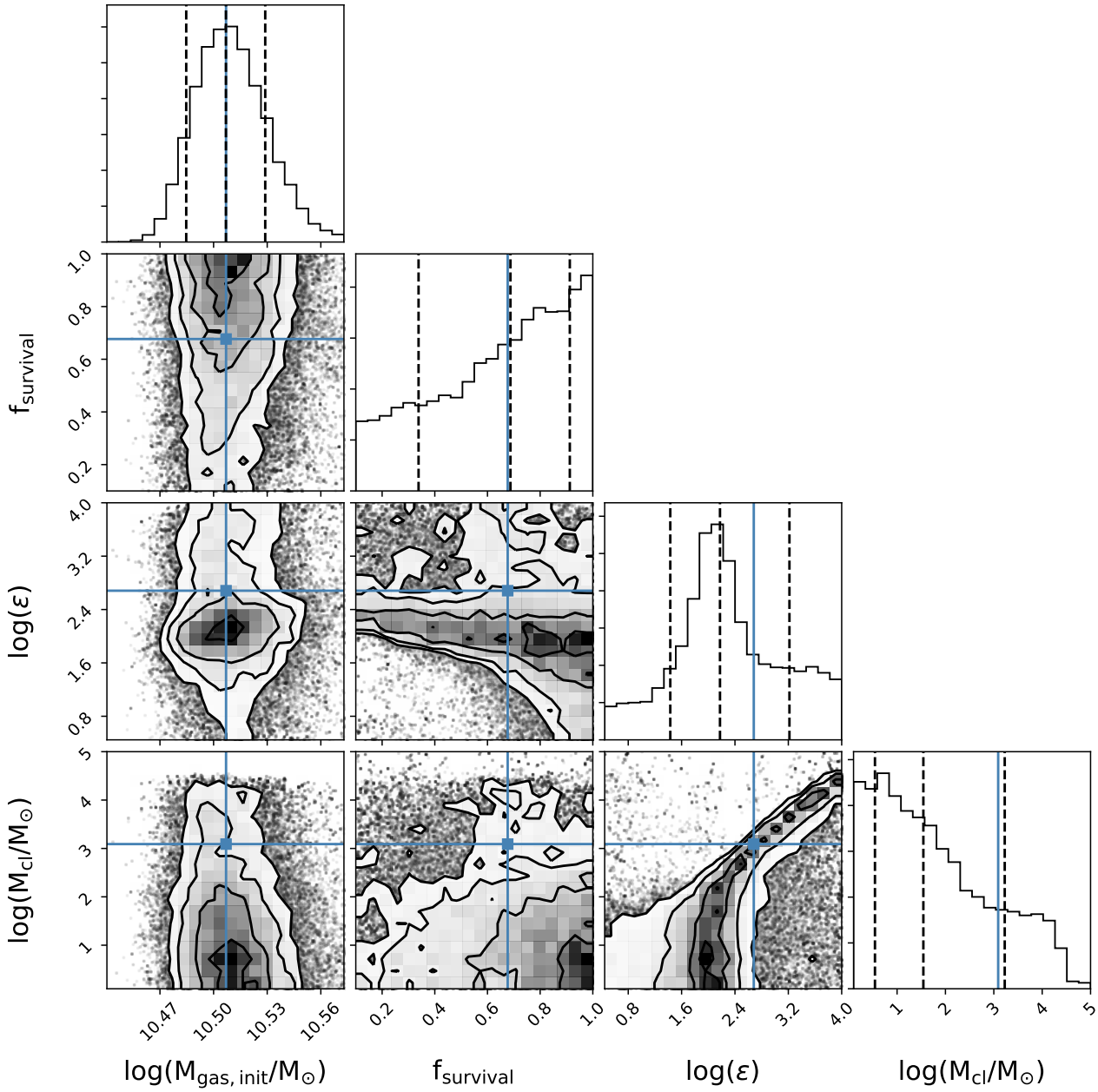

Figure G13. Corner plot for Model I (i.e., closed-box models with a customised SFH) for galaxy bin 5. See caption of Fig. G1 for more information.

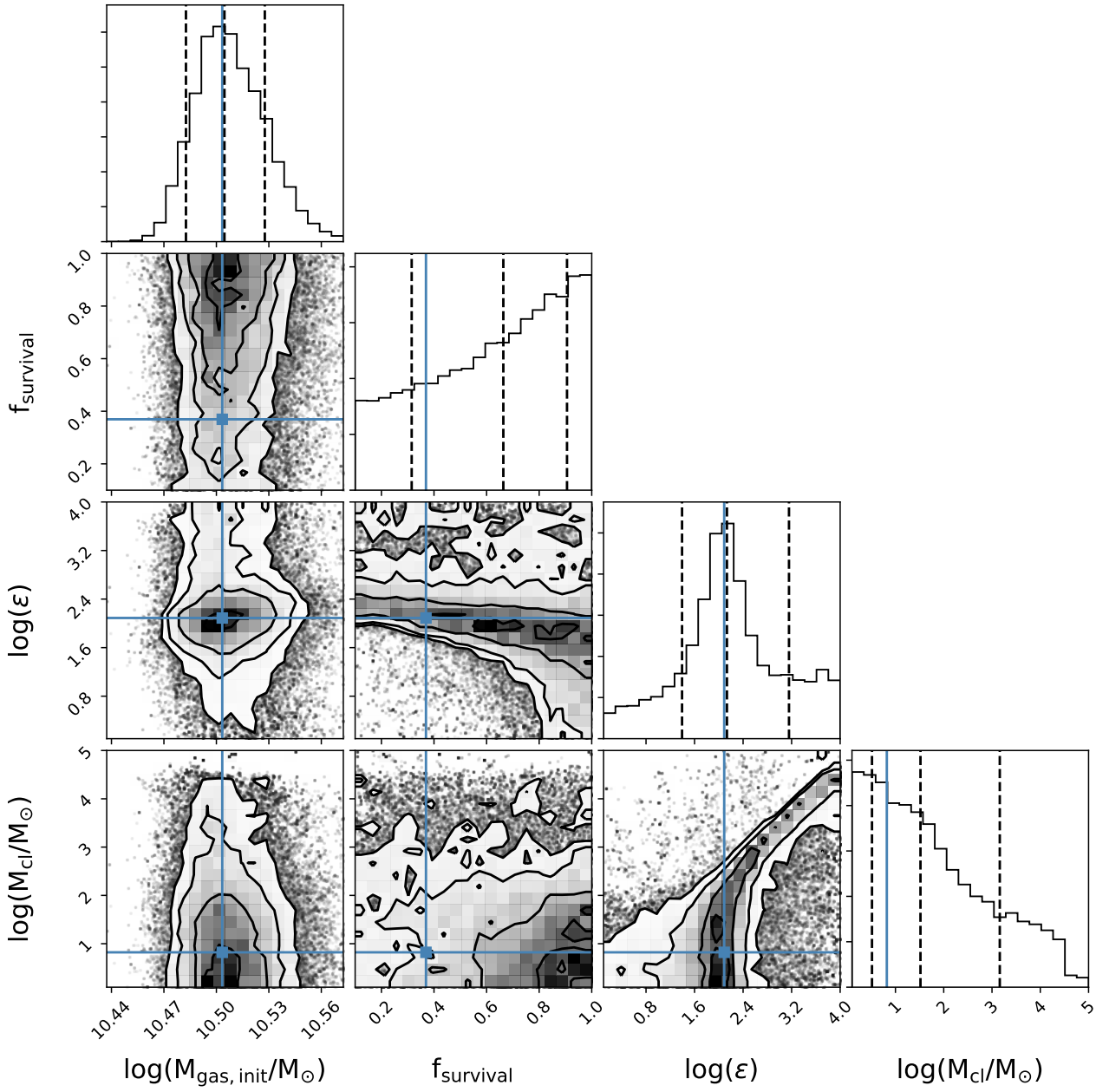

Figure G14. Corner plot for Model II (i.e., closed-box models with a delayed SFH) for galaxy bin 5. See caption of Fig. G1 for more information.

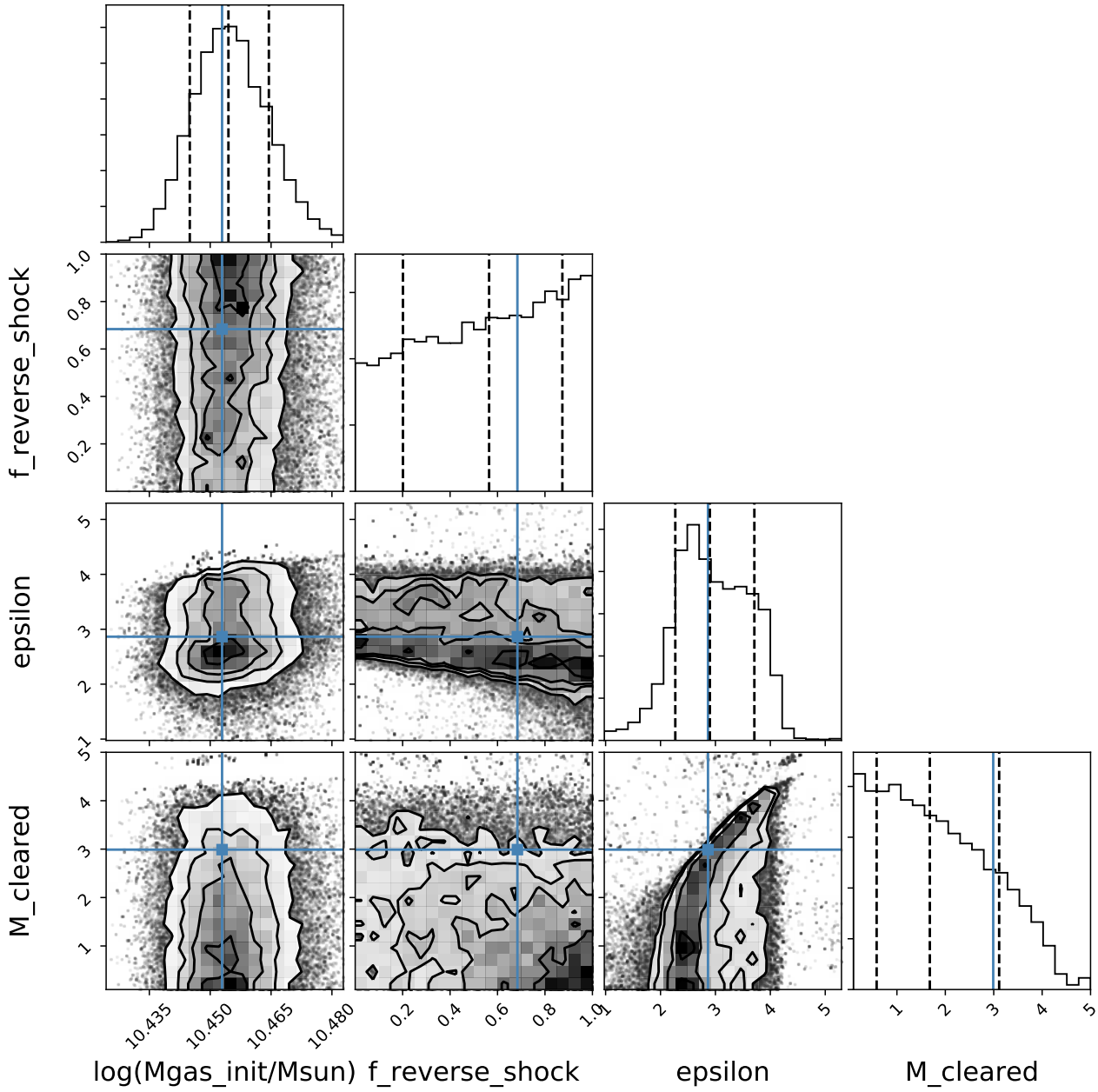

Figure G15. Corner plot for Model III (i.e., models with gaseous flows and a customised SFH) for galaxy bin 5. See caption of Fig. G1 for more information.

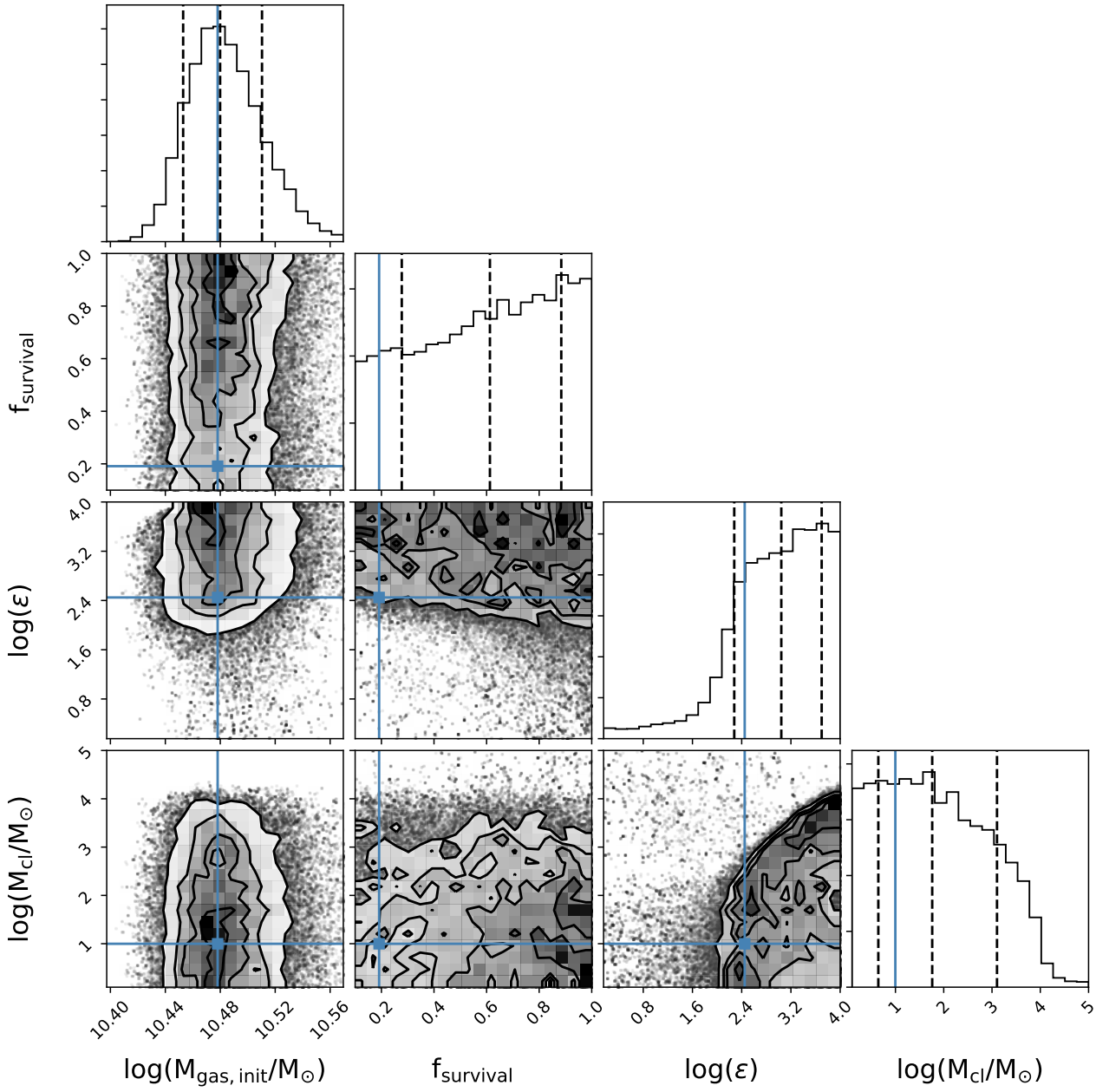

Figure G16. Corner plot for Model I (i.e., closed-box models with a customised SFH) for galaxy bin 6. See caption of Fig. G1 for more information.

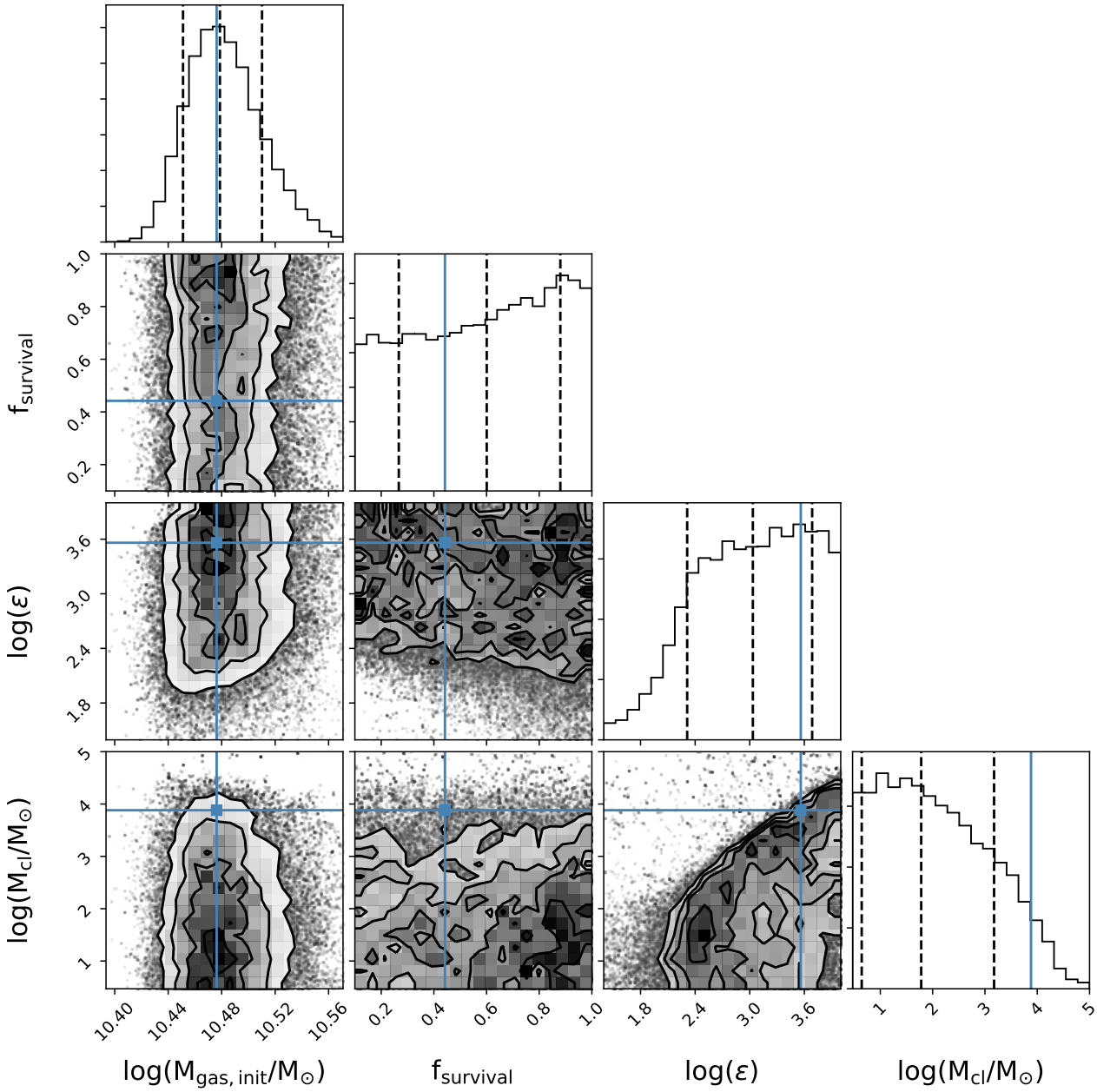

Figure G17. Corner plot for Model II (i.e., closed-box models with a delayed SFH) for galaxy bin 6. See caption of Fig. G1 for more information.

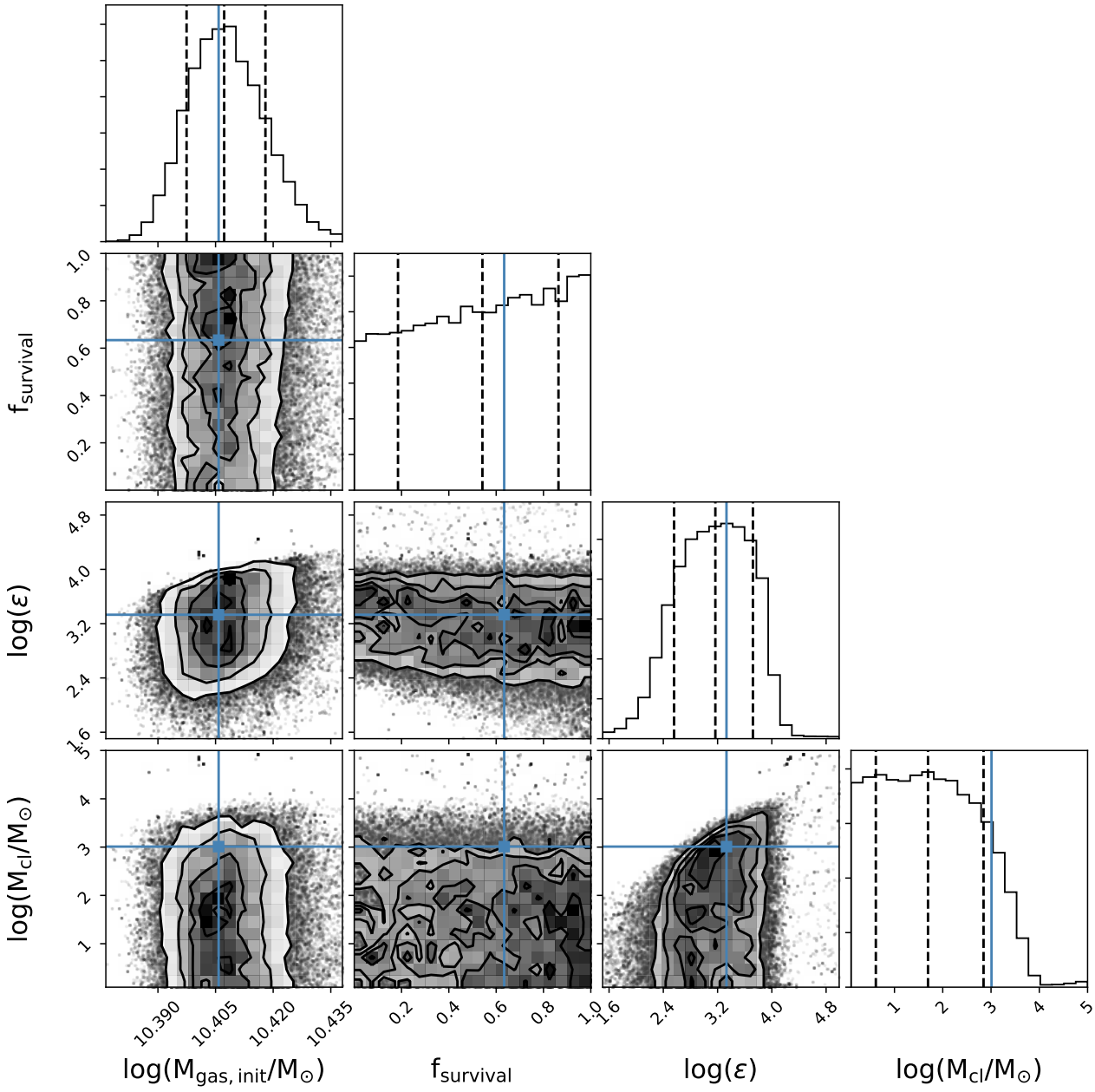

Figure G18. Corner plot for Model III (i.e., models with gaseous flows and a customised SFH) for galaxy bin 6. See caption of Fig. G1 for more information.